

INAUGURAL-DISSERTATION
zur
Erlangung der Doktorwürde
der
Naturwissenschaftlich-Mathematischen
Gesamtfakultät
der
Ruprecht-Karls-Universität
Heidelberg

vorgelegt von
M.Eng. Le Cao
aus Anhui, China

Tag der mündlichen Prüfung: 25.04.2014

Numerical Investigation of Tropospheric Halogen Release and Ozone Depletion in the Polar Spring

Gutachter: Prof. Dr. Eva Gutheil
Prof. Dr. Ulrich Platt

Contents

Abstract	I
Zusammenfassung	III
1. Introduction	1
1.1 The Atmosphere of the Earth	1
1.2 The Role of Ozone in the Lower Atmosphere	2
1.2.1 Ozone in the Stratosphere	3
1.2.2 Ozone in the Troposphere	5
1.3 Research Objectives	8
2. Background	11
2.1 The Ozone Chemistry in the Lower Atmosphere	11
2.1.1 The Reactions of Ozone in the Stratosphere	11
2.1.2 The Reactions of Ozone in the Troposphere	14
2.2 Ozone Depletion Event in the Polar Spring	15
2.3 Types of Boundary Layers	23
2.4 State of the Art	25
3. Model Description	27
3.1 Box Model	27
3.1.1 Parameterization of the Heterogeneous Reactions	28
3.1.2 Photolysis Reactions	31
3.1.3 Sensitivity Analysis	32
3.2 Three-Dimensional Model	33
3.2.1 Configuration	33
3.2.2 Governing Equations	34
4. Numerical Scheme	39
4.1 Discretization of the Equations	39
4.2 Pressure-Implicit with Splitting Operations (PISO) Method	42
4.3 Implementation of the PISO Method in OpenFOAM	46

5. Results and Discussion	51
5.1 Box Model	51
5.1.1 Bromine Only Chemical Reaction Mechanism	52
5.1.2 NO _x Related Chemical Reaction Mechanism	63
5.1.3 Chlorine Related Chemical Reaction Mechanism	70
5.1.4 Skeletal Chemical Reaction Mechanism	72
5.2 Three-Dimensional Model	75
5.2.1 Model with a Flat Surface	76
5.2.2 Model with a Mountain	85
6. Conclusions and Future Work	93
6.1 Conclusions	93
6.2 Future Work	95
Appendix	99
A. Nomenclature	A-1
B. Chemical Reaction Mechanism for Ozone Depletion and Halogen Release	B-1
C. Acknowledgements	C-1

Abstract

Ozone is one of the most important natural atmospheric constituents in both the stratosphere and the troposphere of the earth. Compared with the ozone in the stratosphere, which is mainly formed via the natural photolytic decomposition of oxygen molecules, the ozone in the troposphere originates from reactions involving volatile organic compounds (VOC) and nitrogen oxides (NO_x). The near-surface mixing ratio of ozone varies with the regions. In pristine regions, such as the Arctic and the Antarctic, the natural mixing ratios of ozone in the troposphere range from 30 to 40 nmol/mol on average. About thirty years ago, a rapid destruction of the tropospheric ozone on a time scale of hours to days was observed in polar regions during spring time. Meanwhile, a negative correlation between halogen (e.g. Br and Cl) concentrations and ozone mixing ratios was found, which reveals the involvement of halogen species in the ozone depletion process. It has been presumed that halogen species participate in a variety of chemical reaction cycles, leading to ozone depletion. Moreover, the oxidation of inert halogen ions from aerosol particles, fresh sea ice or snow packs can also speed up the depletion of ozone in the troposphere by releasing Br_2 and BrCl from the surfaces of these substrates.

The tropospheric ozone depletion event has broad impacts on the atmospheric chemistry of the polar regions, such as changing the lifetimes of the hydrocarbons and the formation of the aerosol particles. Therefore, in this study, the modeling of tropospheric ozone depletion in polar spring is addressed. The first step is to identify an appropriate chemical reaction mechanism for capturing the temporal evolution of the chemical mixing ratios. Thus, a box model study is conducted, in which the transport of the air is not included and only chemical reactions are considered. Three chemical reaction schemes are investigated in the box model study: a bromine-only reaction scheme, which then is subsequently extended to include nitrogen and chlorine related species. The heterogeneous reaction rates are parameterized by considering the aerodynamic resistance, the reactive surface ratio, β , i.e. the ratio of reactive surface area to total flat ground surface area, and the boundary layer height, L_{mix} . In the chemical reaction mechanism in which nitrogen and chlorine are not considered, it is found that for $\beta = 1$, a substantial ozone decrease occurs after five days and lasts for 40 h for $L_{\text{mix}} = 200$ m. For about $\beta \geq 20$, the time required for major ozone depletion ($[\text{O}_3] < 4$ ppb) to occur becomes independent of the height of the boundary layer and approaches the minimum time of two days, 28 h of which are attributable to the induction and 20 h to the depletion time. In the chemical reaction mechanism including the nitrogen containing compounds, it is found that a small amount of NO_x may have a strong impact on the ozone depletion rate in the polar regions. During the ozone

depletion, a reaction cycle involving BrONO_2 hydrolysis is dominant. A critical value of 0.0004 of the uptake coefficient of the BrONO_2 hydrolysis reaction at the aerosol and saline surfaces is identified, beyond which the existence of NO_x accelerates the ozone depletion event, whereas for lower values, deceleration occurs. In the chlorine related chemical reaction mechanism, the calculation of the time-integrated bromine and chlorine atom concentrations suggests a value on the order of 10^3 for the $[\text{Br}] / [\text{Cl}]$ ratio, which shows that chlorine atoms have minor direct influence on ozone depletion.

A sensitivity analysis is conducted in the box model to show the relative importance of each reaction in the mechanism. It is found that during the ozone depletion time, the heterogeneous activation processes related to HOBr become more important due to the high bromine concentration in the air at this time period. Moreover, the critical role of the BrONO_2 related reactions in the ozone depletion mechanism is confirmed by the relative NO_x concentration sensitivities. On the basis of the sensitivity analysis of the bromine-only chemical reaction mechanism, 27 less important reactions with the lowest sensitivities and four related species are removed from the original bromine only chemical reaction mechanism. As a result, a skeletal mechanism applicable in 3-D simulations is obtained, which consists of 28 reactions among 26 species. The major features, including the evolution and peak values of the mixing ratios of the chemical species, are maintained.

The skeletal chemical reaction mechanism is implemented in a meteorological 3-D model. Large eddy simulation accounts for the turbulence, and the Smagorinsky model is employed as the sub-grid model. Different physical boundaries on the ground are used in the 3-D model: a flat surface on the ground, and a mountain located on the surface. It is found that the vertical turbulent mixing of air parcels occurs below the height of the polar boundary layer, leading to a non-uniform vertical distribution of the chemical species mixing ratios. The ozone is totally consumed near the bottom surface where a strong elevation of the reactive bromine species occurs. Weather conditions such as wind speed, surface topography and the boundary layer stability may affect the boundary layer height, thus influencing the ozone depletion rate.

Keywords: Ozone depletion, Halogen release, Detailed chemical reaction mechanism, Sensitivity analysis, Skeletal chemical reaction mechanism, Large eddy simulation

Zusammenfassung

Ozon ist ein wichtiges Spurenelement in der Stratosphäre und Troposphäre der Erde. Verglichen mit dem Ozon in der Stratosphäre, welches hauptsächlich durch die natürliche photolytische Dekomposition von Sauerstoffmolekülen gebildet wird, entsteht das Ozon in der Troposphäre durch Reaktionen, die flüchtige organische Verbindungen (volatile organic compounds, VOC), und Stickstoffoxide (nitrogen oxides, NO_x), beinhalten. Das Mischungsverhältnis von Ozon nahe der Erdoberfläche ist abhängig von der betrachteten Region. In abgelegenen Gebieten, wie der Arktis und der Antarktis, schwankt das natürliche Ozonmischungsverhältnis im Durchschnitt zwischen 30 und 40 nmol/mol. Vor etwa 30 Jahren, in einem Frühjahr Mitte der 80er Jahre, wurde eine rasche Zerstörung von Ozon innerhalb von Stunden oder wenigen Tagen in den Polarregionen beobachtet. Gleich-zeitig wurde ein negativer Zusammenhang zwischen den Halogenkonzentrationen (z.B. Br und Cl) und den Ozonmischungsverhältnissen gefunden, was auf eine Beteiligung der Halogene bei dem Ozonabbauprozess hinweist. Es wird angenommen, dass Halogene an zahlreichen chemischen Reaktionen beteiligt sind und dadurch den Ozonabbau verursachen. Außerdem könnte die Oxidation von inerten Halogenionen aus Aerosolen, Meereis oder Schnee ebenfalls den Ozonabbau in der Troposphäre beschleunigen, indem Br_2 und BrCl von der Oberfläche dieser Substrate freigesetzt wird.

Der Ozonabbau in der Troposphäre hat einen tiefgreifenden Einfluss auf die chemischen Prozesse in der Atmosphäre der Polarregionen, z.B. ändert sich die Lebensdauer der Kohlenwasserstoffe und die Bildung von Aerosolpartikeln. Deshalb befasst sich die vorliegende Arbeit mit der Modellierung des Ozonabbaus in der Troposphäre im polaren Frühjahr. Der erste Schritt ist die Identifikation eines geeigneten Mechanismus, der die zeitlichen Verläufe der chemischen Mischungsverhältnisse akkurat erfasst. Es werden drei chemische Reaktionsschemata mit Hilfe eines sogenannten Boxmodells, das nur chemische Reaktionen und keine Luftströmung berücksichtigt, untersucht: ein zunächst auf den Bromverbindungen aufbauender Mechanismus, welcher anschließend um Stickstoff- und Chlorverbindungen ergänzt wird. Die heterogenen Reaktionsgeschwindigkeiten wurden parametrisiert, um den aerodynamischen Widerstand, das reaktive Oberflächenverhältnis, β , d.h. das Verhältnis der reaktiven Oberfläche zur gesamten, eben angenommenen, Oberfläche, und die aerodynamische Grenzschichtdicke, L_{mix} , zu berücksichtigen. Für die chemischen Reaktionsmechanismen, für die Stickstoff und Chlor enthaltenden Spezies nicht berücksichtigt werden, wird im Fall von $\beta = 1$ und $L_{\text{mix}} = 200 \text{ m}$ eine deutliche Reduzierung des Ozons nach 5 Tagen und für eine Dauer von 40 Stunden beobachtet. Für $\beta > 20$ ist die Zeit, die für einen wesentlichen Ozonabbau ($[\text{O}_3] < 4 \text{ ppb}$) benötigt wird, unabhängig von der

Dicke der aerodynamischen Grenzschicht und nähert sich 2 Tagen, davon 28 Stunden für die Induktion und 20 Stunden für die Abbauphase. Wenn stickstoffhaltige Verbindungen zu dem Reaktionsmechanismus hinzugefügt werden, wird festgestellt, dass bereits eine geringe Menge NO_x einen großen Einfluss auf den Ozonabbau in Polarregionen haben kann. Während des Ozonabbaus ist ein Reaktionszyklus, der die Hydrolyse von BrONO_2 beinhaltet, dominant. Es wird ein kritischer Wert von 0.0004 für den Aufnahmekoeffizienten der BrONO_2 Hydrolysereaktion an den Aerosol- und Salinoberflächen festgestellt, über welchen hinaus die Anwesenheit von NO_x den Ozonabbau beschleunigt, während bei niedrigeren Werten der Abbau verlangsamt wird. Im Reaktionsmechanismus mit Chlor enthaltenden Spezies legt die Berechnung der zeitintegrierten Brom- und Chlorkonzentrationen einen Wert in der Größenordnung 10^3 für das $[\text{Br}]/[\text{Cl}]$ Verhältnis nahe, was zeigt, dass Chlor nur einen geringen direkten Einfluss auf den Ozonabbau hat.

Eine Empfindlichkeitsanalyse wird im Boxmodell durchgeführt, um den relativen Einfluss jeder einzelnen Reaktion im Mechanismus zu untersuchen. Es wird beobachtet, dass die auf HOBr bezogenen heterogenen Aktivierungsprozesse während des Ozonabbaus, durch die gleichzeitig hohen Bromkonzentration in der Luft an Gewicht gewinnen. Weiterhin wird die kritische Rolle der BrONO_2 -bezogenen Reaktionen im Ozonabbauprozess durch die relative Empfindlichkeit bezüglich der NO_x Konzentration bestätigt. Auf Basis der Empfindlichkeitsanalyse des ausschließlich auf Bromverbindungen beschränkten Reaktionsmechanismus wurden 27 weniger wichtige Reaktionen und 4 weniger wichtige Stoffe identifiziert und aus dem Mechanismus entfernt. Das Ergebnis ist ein Skelettmechanismus für 3-D Simulationen, der 28 Reaktionen und 26 Verbindungen beinhaltet. Die wichtigsten Eigenschaften wie die Entwicklung und Maximalwerte der Mischungsverhältnisse der Stoffe, werden erhalten.

Der Skelettmechanismus ist in ein meteorologisches 3-D Modell implementiert. Die Turbulenz wird durch die Methode der Grobstruktursimulation modelliert und als Kleinskalenmodell wird das von Smagorinsky angewandt. Zwei unterschiedliche Randbedingungen werden für die Erdoberfläche verwendet: eine flache Oberfläche und eine Bergstruktur. Es wird beobachtet, dass die vertikale turbulente Mischung der Umgebungsluft innerhalb der polaren Grenzschicht stattfindet und zu einer ungleichmäßigen vertikalen Verteilung der Mischungsverhältnisse der verschiedenen Stoffe führt. Wenn das Ozon aufgebraucht ist, wird ein starker Anstieg des reaktiven Broms nahe der Erdoberfläche verzeichnet. Die Wetterbedingungen wie z.B. Windgeschwindigkeit und die Stabilität innerhalb der Grenzschicht können die Grenzschichtdicke beeinflussen und haben dadurch ebenfalls Einfluss auf die Ozonabbaugeschwindigkeit.

Schlagnworte: Ozonabbau, Halogenfreisetzung, detaillierter chemischer Reaktionsmechanismus, Skelettmechanismus, Grobstruktursimulation

List of Figures

1.1	Sketch of the lower atmosphere.	2
1.2	Antarctic ozone holes in four different years.	4
1.3	Potato leaves with brown spots in a high ozone concentration environment.	6
1.4	First observation of the correlation between ozone depletion in the troposphere and rapid bromine enhancement, conducted at Alert, Canada in April 1986.	7
2.1	Snow cover in Arctic in February 2009.	16
2.2	A sketch for halogen chemistry.	17
2.3	A sketch of the pathway for the speeding up of the ozone depletion by NO _x species.	21
2.4	A sketch of the pathway for the ozone production by NO _x species.	22
2.5	Vertical distributions of wind speed and potential temperature in the convective and stable boundary layer.	24
3.1	Schematic depiction of the model.	34
4.1	Categories of the numerical methods to solve the flow field.	43
4.2	Flow chart for PISO algorithm.	45
5.1	Time variation of ozone and bromine species for bromine only mechanism with the boundary layer height of 200 m.	53
5.2	Time variation of ozone and bromine species for bromine only mechanism with the boundary layer height of (a) 500 m; (b) 1000 m.	54
5.3	Time variation of ozone and bromine species for bromine only mechanism, when the initial Br ₂ mixing ratio is (a) 0.1 ppt; (b) 0.5 ppt.	55
5.4	Effect of heterogeneous reaction rate on the ozone depletion time.	56
5.5	Temporal behavior of ozone relevant reaction rates in a 200 meters boundary layer: (a) formation (b) depletion.	57
5.6	Contribution to ozone depletion at: (a) day 2 (induction stage) (b) day 6 (depletion stage).	58
5.7	Contribution to Br formation at day 6 (depletion stage).	59

5.8	Relative sensitivities of ozone and BrO concentrations for bromine containing reactions at day 6 for a 200 m boundary layer height.	60
5.9	Temporal evolution of ozone concentration sensitivities for mixing length L_{mix} , uptake coefficient γ and surface coverage ratio β	61
5.10	Impact of the reactive surface ratio on the (a) total ozone depletion time for three different boundary layer heights (b) induction and depletion time for a 200 m boundary layer height.	62
5.11	Time variation of ozone, nitrogen containing species and bromine concentrations for a boundary layer height of 200 m.	63
5.12	Temporal change of NO _x relevant reaction rates in 200 m boundary layer height: (a) formation (b) depletion.	65
5.13	Relative sensitivities of NO _x concentrations at day 4 for a boundary layer height of 200 m.	66
5.14	Relative sensitivities of O ₃ concentrations at day 4 for a boundary layer height of 200 m.	67
5.15	Relative sensitivities of O ₃ and BrO concentrations at day 4 for a boundary layer height of 200 m.	68
5.16	Ozone depletion rates with different values of BrONO ₂ hydrolysis uptake coefficient.	69
5.17	Time evolution of ozone, chlorine containing species and total chlorine concentrations, when the boundary layer height is 200 m.	70
5.18	Impact of the reaction rate ratio of (R14) and (R129), $K_{Br_2/BrCl}$, on the ozone depletion time.	71
5.19	Time integrated halogen atom concentrations and the [Br]/[Cl] ratio versus the ozone mixing ratio.	72
5.20	Temporal behavior of relative sensitivities of ozone for a 200 meters boundary layer height.	73
5.21	Time variation of mixing ratio of ozone and bromine species for the boundary layer height of 200 m for the detailed and skeletal bromine only mechanism in the box model study.	75
5.22	Schematic depiction of the simulation with a flat ground surface.	76
5.23	Instantaneous velocity in x direction at cut plane $x = 200$ m.	79
5.24	Instantaneous velocity in y direction at cut plane $x = 200$ m.	80
5.25	Vertical distribution of averaged wind profiles over the 9 th hour.	80
5.26	Distribution of the instantaneous vertical velocity at hour 9 in (a) 3D view and (b) 2D view cut plane at $x = 0$ m.	81
5.27	Probability density function for the instantaneous vertical velocity at the 9 th hour.	82

5.28	Averaged effective turbulent diffusivity over the 9 th hour.	83
5.29	Vertical distribution of ozone, BrO and HOBr at day 6.	83
5.30	Vertical distributions of averaged wind profiles and effective turbulent diffusivity over the 9 th hour when wind speed is 15 m/s.	84
5.31	Melville Island in Canada.	86
5.32	Three-dimensional view of the computational domain with the mountain topography surface.	86
5.33	Instantaneous wind speed in x direction at the 9 th hour at $y = -60$ km cut plane.	88
5.34	Instantaneous wind speed in y direction at the 9 th hour at $x = -40$ km cut plane.	89
5.35	Instantaneous wind speed in z direction at the 9 th hour at $y = -60$ km cut plane.	89
5.36	Distribution of the ozone concentration at the 9 th hour at $y = -60$ km cut plane.	90
5.37	Distribution of the BrO concentration at the 9 th hour at $y = -60$ km cut plane.	90
6.1	Gas transfer processes in the boundary layer.	96

List of Tables

3.1	Coefficients for the photolysis reaction rates.	32
3.2	Relative sensitivities for the Chapman mechanism.	33
5.1	Emission fluxes from the snow.	51
5.2	Initial gas composition.	52
5.3	List of ozone relevant reactions.	56
5.4	List of NO _x relevant reactions.	64
5.5	Overview of NO _x relevant reactions.	64
5.6	Bromine only mechanism for ozone depletion and bromine explosion. .	74
5.7	Inlet values of the principal chemical species.	87

1. Introduction

1.1 The Atmosphere of the Earth

The earth's atmosphere is a layer of gases, which contains 78% nitrogen (N_2), 21% oxygen (O_2) and 1% argon (Ar). The nitrogen in the atmosphere is accumulated since the ancient time because N_2 is chemically inert and water insoluble, whereas the majority of the oxygen in the atmosphere originates from the photosynthesis of the plants on the earth. Water vapor usually has the fourth highest concentration in the atmosphere, which can reach to at most 3% of the atmosphere. The concentration of the water vapor varies with the locations, dominated by the precipitation and the deposition processes [1]. The remaining gaseous constituents such as ozone, sulfur dioxide (SO_2) and nitrogen oxides (NO_x) occupy less than 1% of the earth's atmosphere. In the 18th century, the focus of the study of the earth's atmosphere is on the major components of the atmosphere, N_2 , O_2 , water vapor and carbon dioxide CO_2 . Since the late 19th century, the chemical production and depletion of the gaseous constituents, which have mole fractions less than 1 $\mu\text{mol/mol}$, have been investigated as these gases are involved in a variety of the chemical and anthropogenic processes, such as the global warming effect, fuel combustion and biomass burning [1].

Based on the altitude, the earth's atmosphere can be divided into upper and lower regions. Since most of the earth's weather phenomena occurs below the altitude of 50 km, the lower atmosphere attracts the most attention from the meteorologists. The lower atmosphere can be divided into different parts according to the properties of the atmospheric layers such as pressure and temperature. Figure 1.1 shows the structure of the lower atmosphere. It is seen that the lower atmosphere contains two atmospheric layers. The one residing in the top part is the stratosphere. It extends from approximately 11 km to 50 km above the earth's surface. In the stratosphere, the temperature increases with height, which suppresses the vertical motions of the air parcels in this layer. Thus, little vertical mixing can be observed in the stratosphere. The other layer is the troposphere, which is the lowest part of the earth's atmosphere. The height of the troposphere amounts to roughly 11 km extending from the surface of the earth. Most of the activities of the living things on the earth take place in this layer. The troposphere is characterized with a rapid vertical mixing of air and large

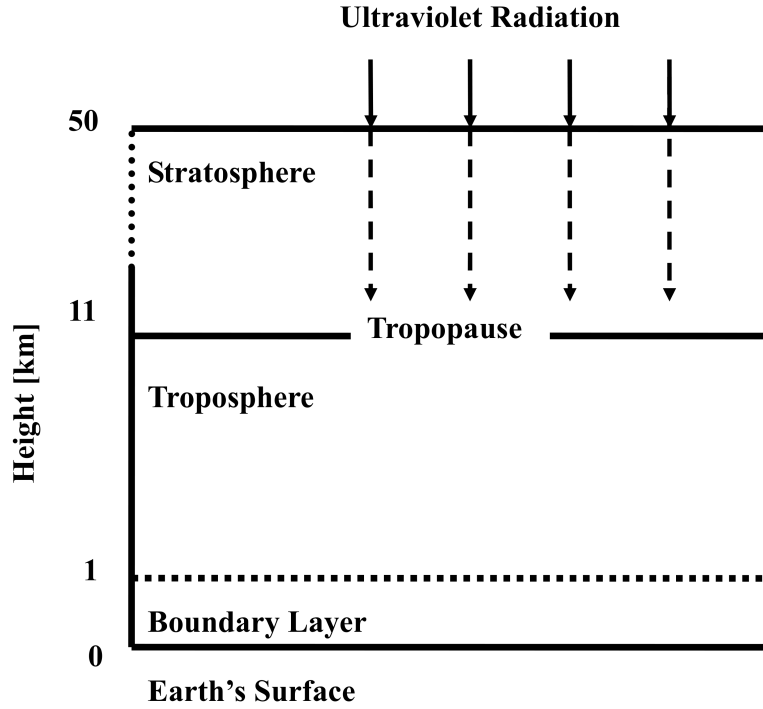


Figure 1.1: Sketch of the lower atmosphere.

scale vertical mixing structures. The temperature in the troposphere usually decreases with the height. Between stratosphere and troposphere, there exists a boundary called tropopause. When an air parcel moves across the tropopause, the cooling with the height stops and the air parcel is surrounded by the ambient air with almost constant temperature.

1.2 The Role of Ozone in the Lower Atmosphere

Ozone (O_3) in the lower atmosphere receives special attention as it is a precursor of many atmospheric oxidizers, and it determines the oxidation power of the atmosphere. It was first detected by Schoenbein [2], who also estimated the gaseous ozone concentrations in many cities of Europe. Later on, the special role of ozone in absorbing the ultraviolet (UV) radiation with the wavelength between 200 nm and 300 nm was recognized from the laboratory study of Cornu [3] and Hartley [4]. In order to figure out the global ozone distribution and the relation between ozone variations and other geophysical conditions, the Dobson spectrometer was developed by Dobson et al. [5] for measuring the total amount of ozone regularly. A network was also constructed for connecting the ozone measuring stations all over the world. The vertical distribution

of ozone was first obtained by Götz et al. [6] by observing the spectra of scattered radiation during the time of sunrise and sunset. Then the vertical distribution of ozone up to 70 km was captured by Johnson et al. [7] by using a rocket flight. During the year of 1957-1958, a large number of the ground ozone measuring stations were established including several stations in the Antarctic. A global map of the variation of ozone concentration with season and latitude for the whole Northern Hemisphere was obtained based on the observations of this ozone measuring network. The satellite ozone measurements started in the 1970's. It started from the application of the back-scatter UV technique [8] on the satellite named Nimbus-4, then a comprehensive picture of the ozone data for the year 1970 was obtained from this satellite measurements. In 1978, an improved version of the ozone measuring instruments was utilized in the Nimbus-7 satellite, providing the data for the total column ozone and also its vertical distribution in a low resolution. The tropospheric ozone concentration has also been detected since the 1970's by using the ozonesondes which are the balloons with the installation of the electrochemical sensor [9, 10]. In these ozonesondes observations, an annual increase of tropospheric ozone in both Europe and North America is shown.

1.2.1 Ozone in the Stratosphere

About 90% of the earth's ozone exists in the stratosphere and it plays two major roles in the stratosphere. First, by absorbing the UV radiation, the stratospheric ozone may convert the solar energy into heat, which increases the temperature in the upper stratosphere and suppresses the temperature inversion in the stratosphere [1]. This is also the major reason for the existence of the stratosphere. Secondly, as it could absorb most of the UV radiation with the wavelength between 280-320 nm, which is often called UV-B [11]. The UV-B can penetrate human skin and be absorbed by the deoxyribonucleic acid (DNA), which subsequently cause the initiation of the skin cancer [12]. Thus, by absorbing UV-B, the stratospheric ozone is a protection of the life on the earth.

It has been reported [13] that the amount of the stratospheric ozone has decreased significantly since the 1950's. This decrease of the ozone in the stratosphere has several health impacts. The incidence of skin cancer increases as excessive UV rays reach human bodies with less ozone in the stratosphere. This effect is confirmed by the recent assessment [14] showing the dependence of the skin cancer incidence on the stratospheric ozone depletion. Moreover, a long-time exposure to a high intensity of UV radiation also leads to the eye irritation, weakening of the human immune system and some respiratory illnesses [15].

Several potential causes for the depletion of the stratospheric ozone are suggested. It is first postulated by Harrison [17] in the year 1970 that the supersonic aircraft, which

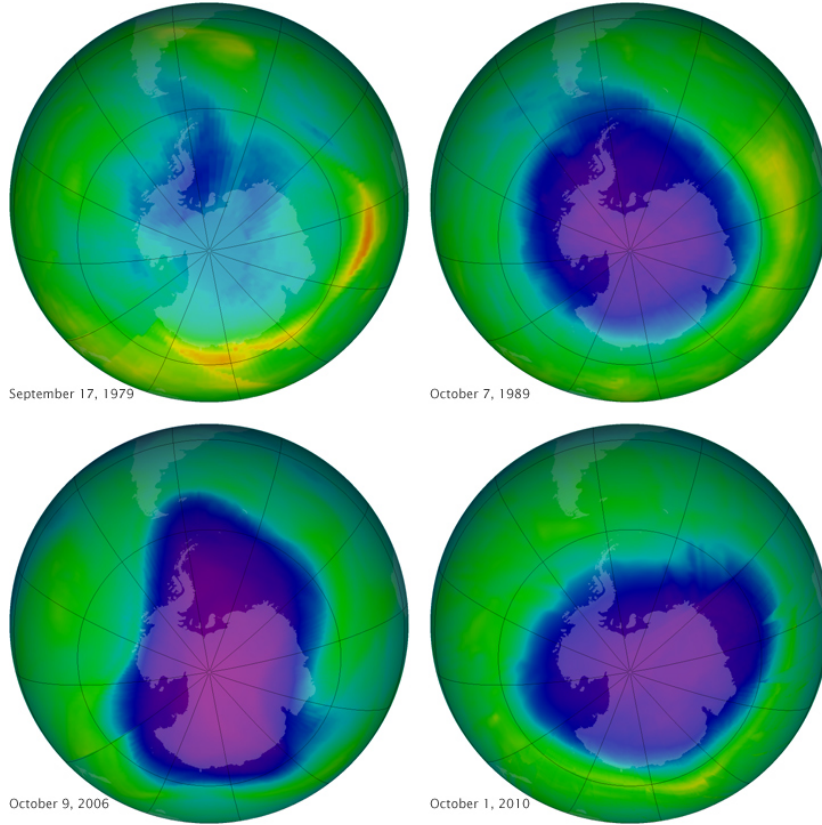


Figure 1.2: Antarctic ozone holes in four different years, the purple and dark blue areas denote the ozone hole [16].

can release the exhaust containing water vapor might have an effect on the stratospheric ozone depletion. However, due to the design problem and a very high cost, currently, there are no remaining supersonic flights working for the commercial service, which eliminates the possibility that the supersonic aircraft causes the stratospheric ozone depletion. The tests of the nuclear weapons by the United States and the Soviet Union during the 1960's can also result in a depletion of the stratospheric ozone. But the observed depleted ozone caused by the nuclear tests is within the normal temporal variation of ozone in the stratosphere. The direct emission from the firing of the rocket has also the potential to cause the stratospheric ozone depletion, but the influence is shown to be negligible in the recent study [18]. Molina and Rowland [19, 20] first suggested that the bulk of the stratospheric ozone depletion is attributable to the chlorine related chemistry, especially the chlorofluorocarbons (CFCs). The CFCs are widely used in the refrigeration, packaging and some other industrial applications. They are inert and not water soluble. The eventual chemical fate of the CFCs is to be transported to the stratosphere and photolyzed in the presence of the solar UV, forming active chlorine atoms, which can destroy ozone in the stratosphere. Thus, in

order to protect the ozone layer in the stratosphere, it is needed to control the global emission of the CFCs to the atmosphere. The first controls of the CFCs were announced in the United States in 1976 and their application range is limited to the propellant gases in the aerosol sprays. The usage of the refrigerants and plastic forming processes are not taken into account in these controls. Then other countries such as Canada and Norway joined this project. In the autumn of 1987, an international protocol was signed in Montreal [21], aiming at reducing the production of CFCs and recovering the ozone layer in the stratosphere.

In 1985, the "ozone hole" was first revealed by Farman et al. [22] in the Dobson ozone measuring station over the Halley Bay, Antarctic. Figure 1.2 shows the occurrence of the Antarctic ozone hole in the years of 1979, 1989, 2006 and 2010. The measurements were conducted by using NASA's Total Ozone Mapping Spectrometer (TOMS [23]) in the years of 1979-2003 and Royal Netherlands Meteorological Institute (KNMI) Ozone Monitoring Instrument (OMI [24]) from the year 2004 to present. A steady decline of ozone in the stratosphere occurs over Antarctic in the polar spring. It is also found that the occurrence of the ozone hole requires the conditions of a low temperature in which the polar stratospheric clouds can form and the presence of the sunlight [25]. The detailed related reactions are given in Chapter 2 of this thesis.

1.2.2 Ozone in the Troposphere

Compared with the role as a protection layer in the stratosphere, ozone in the troposphere behaves as a type of pollutant and it is harmful to human health and vegetation. Excessive amount of ozone in the troposphere may cause respiratory problems of human. It is found by Lippmann [26] that the exposure of healthy adults to 100 ppb (ppb = parts per billion) ozone for several hours leads to the reduction of the lung function. Moreover, this harmful effect caused by ozone accumulates with longer exposure time. Large amount of ozone in the troposphere can also destroy living tissue, cause eye irritation and chest pain to individuals [27]. The ozone damage is also found to the plants on the earth [28]. The gaseous ozone molecules can enter the plants through the gas exchange pores on the leaves and destroy the cell tissues within the plants. It is observed [29] that the photosynthesis processes of the plants are suppressed if the plants are exposed to a high concentration of ozone, which leads to a slower plant growth. A photograph of the leaves exposed to high concentrations of ozone is shown in Fig. 1.3, which illustrates the ozone damage to the plants.

The ozone in the troposphere is formed through the reactions associated with the ozone precursors, nitrogen oxides and hydrocarbons. Since most of the nitrogen oxides and the hydrocarbons originate from the human activities such as the gasoline vapors, fossil fuel power plants, automobile emissions and some other industries, high tropo-



Figure 1.3: Potato leaves with brown spots in a high ozone concentration environment [16].

spheric ozone mixing ratios are usually found in the rural areas and the regions with heavy industry. Since 1900, it is announced [30] that the ozone concentration detected near the earth's surface has more than doubled with growing population and industrial activities.

The mixing ratios of ozone near the surface of the earth are 20–60 ppb on average, and the regions with ozone mixing ratio exceeding 200 ppb are considered as areas with severe air pollution. In order to protect the human health, the safe levels for the tropospheric ozone have been established in different countries [31]. The standard in the United States is an average mixing ratio of 80 ppb over 8 hours and the standard in European Union is 60 ppb. The most strict standard is set in Japan, which has the average value of 60 ppb over 1 hour. In addition to these national standards, the World Health Organization has also proposed a standard of 60 ppb averaged over 8 hours as a guidance. To achieve these standards, government regulations have been released such as limiting the motor vehicles on the road, controlling the emission from the industry and reducing the number of the coal-fire generating stations in the city.

Similar as the ozone hole in the stratosphere, a rapid ozone depletion event in the troposphere is also observed in the polar spring. In the year 1981, it was first reported by Oltmans [33] that a large daily change of the ozone concentration in the air occurs at Alert, Canada. Later on, Bottenheim et al. [34] found that the ozone is significantly depleted at Alert in the measurements conducted in March 1985. Since then, the tropospheric ozone depletion event has been reported in different locations of the polar regions [32, 35, 36, 37, 38, 39, 40]. It is found in polar regions, the amount of ozone in the

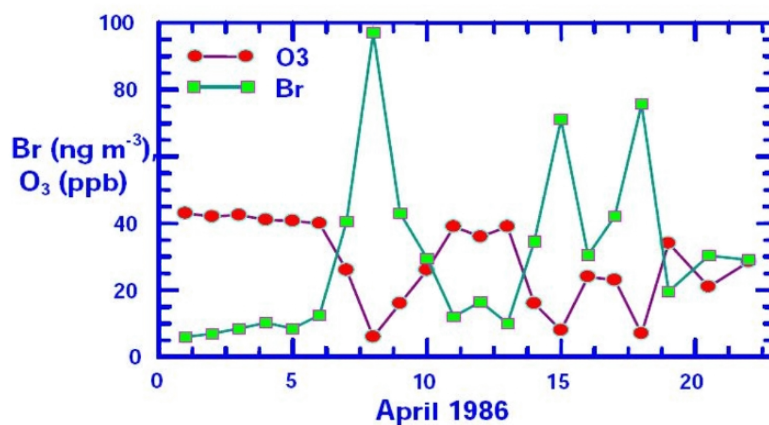


Figure 1.4: First observation of the correlation between ozone depletion in the troposphere and rapid bromine enhancement, conducted at Alert, Canada in April 1986. Figure taken from Barrie et al. [32]. Horizontal axis denotes the time in April 1986, unit: days. Vertical axis represents the mixing ratio of ozone and bromine, unit: ppb and ng m^{-3} .

atmospheric boundary layer may reduce from the background value of tens of ppb to less than 1 ppb within several hours or days in spring seasons. The negative correlation between the ozone and bromine concentrations was first revealed in the measurements conducted by Barrie et al. [32] at Alert in April 1986 (Fig. 1.4). It is seen in Fig. 1.4 that when the mixing ratio of ozone drops down, the concentration of the bromine species in the air significantly increases. It is suggested by Barrie et al. [32] that the photolysis of bromoform may be the source of the bromine atoms. However, it was later estimated by Simpson et al. [41] that the lifetime of the bromoform is too long to produce such a large amount of bromine within a time scale of a few days. The role of bromine monoxide (BrO) in the ozone depletion event was first revealed by Hausmann and Platt [42] in the spectroscopic measurement of bromine oxide and ozone in the Arctic during the Polar Sunrise Experiment 1992 (PSE92) [43]. The sudden increase of halogen species concentrations (X , X_2 , XY , XO , HOX , where X and Y denote halogen atoms such as Br and Cl) during the ozone depletion event has also been reported in both the Arctic and the Antarctic [44, 45, 46, 47, 48, 49, 50, 51, 52]. In order to explain the large amount of the reactive halogen species and the observed ozone loss, a BrO -catalyzed chemical ozone destruction is suggested [42]. A special halogen activation process named the “bromine explosion” is also proposed [53, 54, 55]. In the “bromine explosion” process, active bromine is liberated through the auto-catalytic heterogeneous reactions occurring in the sea-salt aerosols or at the surface of sea ice.

Similar halogen activation and the halogen-induced ozone loss are also found in volcanic plumes [56] and in coastal regions [47]. This tropospheric ozone depletion phenomenon is the major focus of the present study and is explained in detail in Chapter 2.

1.3 Research Objectives

The simulation of the air quality and the ozone concentration is complicated as both the transport properties (wind speed, temperature profile, ...) and the related chemical reactions should be considered in the model. Since the calculation of a coupled system including transport and chemistry is very time-consuming, in previous studies (e.g. Community Model for Air Quality (CMAQ) [57]), the usual treatment in the air quality forecast models is to update the meteorological model every half hour or one hour, then the output of the meteorological model is used as the conditions of the chemical-transport model within this time step. This treatment is computationally efficient and able to simulate some physical phenomena with typical large time scales. However, this treatment neglects the rapid transport processes occurring within the output time step of the meteorological model. Thus, in the recent coupled models developed, the chemical calculations are carried out with the same time step as the one used in the meteorological model, so that the chemical processes and the transport of the air can be simultaneously simulated in these coupled models.

One of these coupled models is GEOS-Chem (Goddard Earth Observing System Chemistry) [58, 59]. It is a 3-D global model for investigating the variation of the background surface ozone mixing ratios in North America. The causes for the observed elevated ozone mixing concentrations in North America are also examined from the simulation results by using GEOS-Chem. GEOS-Chem has also been applied to the European regions by Auvray and Bey [60] to study the effect on the ozone budget caused by the long-range transport processes. It is found that the local emission of ozone precursors is the major cause of the ozone distributed over Europe instead of the long-range transport. A coupled model MC2-AQ (Mesoscale Compressible Community model with Air Quality) is first implemented by Kaminski et al. [61] for European conditions. Kaminski et al. conclude that the weak wind and high temperature conditions over western Europe in summer lead to the enhanced ozone mixing ratios of more than 90 ppb. By using a model named Meso-NH-C (Mesoscale Non-hydrostatic Chemistry), Tulet et al. [62] observe a rapid ozone increase over the French polluted areas. The spatial distribution of the ozone concentrations between northern France and southern England is also derived by using this model. A 3-D mesoscale model RAMS-Chemistry (Regional Atmosphere Modeling System Chemistry) [63, 64] is used to study the effect of the vertical convection between the upper troposphere and the lower stratosphere on

the vertical distributions of the ozone precursors such as nitrogen oxides and the ozone budget in the stratosphere. Since the year 2000, several research groups have been working on the development of the meteorological model WRF (Weather Research and Forecasting [65]). Grell et al. [66] first fully coupled a chemical module related to ozone pollution with WRF, which is called WRF/Chem model. In the WRF/Chem model, the predictions of the ozone concentrations and the ozone precursors are improved due to the refined parameterization of the physics within the boundary layer. A global multi-scale model GEM-AQ (Global Environmental Multi-scale Air Quality) [67] is developed with the focus on the middle and lower troposphere. The modeled global distributions of the tropospheric ozone are compared with the satellite images for the spring, summer and autumn seasons of the year 2001.

However, the models mentioned above are not applicable to predict the tropospheric ozone depletion in the polar spring. The reason is that the halogen chemistry causing the tropospheric ozone depletion has not been implemented in these models. Moreover, in the polar regions, the heterogeneous gas exchange between the bottom ice/snow surface and the ambient air is a major source of the halogen species in the polar troposphere. This heterogeneous process is also not included in these models. Thus, for simulating the tropospheric ozone depletion in the polar spring, a variety of specific numerical models have been developed to investigate this ozone depletion event and the halogen explosion, which are described in Chapter 2 of this thesis. Despite these efforts, some fundamental issues are still unresolved. These issues can be summarized as:

- **What are the sources of the halogens causing the ozone depletion?**

The sources of the reactive halogens are not clear until now. The possible sources include: aerosol particles derived from the frost flowers, fresh sea ice, snow pack on the sea ice, blowing snow lifted by the strong wind, thin brine layer on the ice/snow pack surface, etc.

- **What is the effect caused by the change of the weather conditions?**

Different weather conditions can influence the ozone depletion rate and the related chemical species concentrations. The weather condition depends on the boundary layer height, wind speed, temperature inversion intensity and surface properties such as the uptake of the reactants at the ice/snow surface.

- **What is the role for each reaction in the ozone depletion and halogen release mechanism?**

The importance of each reaction in the chemical reaction mechanism is not clear. Moreover, it is helpful to know, which reactions contribute more to the ozone consumption and the increase of the halogens.

- **How to include the effect of the vertical turbulent mixing for the ozone depletion more accurately?**

Both the local chemistry and the transport of the air parcels may change the ozone concentration. In order to simulate the vertical turbulent mixing in the atmospheric boundary layer more accurately, a multi-dimensional model with the appropriate turbulence model is required.

The purpose of this thesis is to address these issues. The organization is as follows. In Chapter 2, some basic concepts about the ozone depletion event and the related chemical reactions are given. Besides, the recent development of the numerical models is discussed. In this study, a box model and a three-dimensional model are constructed. These two models and the relevant equations are described in Chapter 3. Chapter 4 shows the discretized form of the equations given in Chapter 3 and the algorithm used to solve these equations. The computational results are presented in Chapter 5. These results are categorized by the type of the model used. In Chapter 6, a summary of the major conclusions is given. The potential extension of the model is also discussed. The appendix contains a list of symbols and the chemical reaction mechanisms implemented in the model.

2. Background

In this chapter, a brief description is presented for

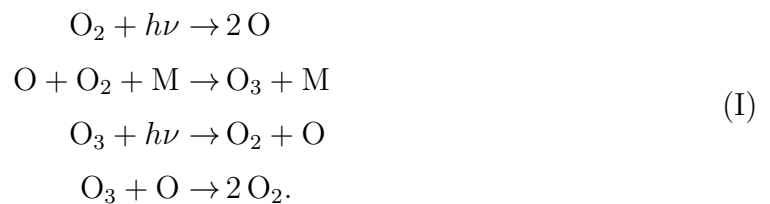
- the chemical production or depletion pathways of ozone in the lower atmosphere,
- ozone depletion event in the polar spring,
- types of the atmospheric boundary layers,
- development of numerical modeling for the ozone depletion event in polar regions.

2.1 The Ozone Chemistry in the Lower Atmosphere

Ozone is a natural gas which affects the mixing ratios of many atmospheric constituents such as CO₂. It is produced or destructed by a variety of chemical reaction cycles in the presence of UV radiation from the sun, nitrogen oxides, hydroxyl radicals (OH) and halogen species in the stratosphere and troposphere. These chemical reaction cycles are discussed in the following sections.

2.1.1 The Reactions of Ozone in the Stratosphere

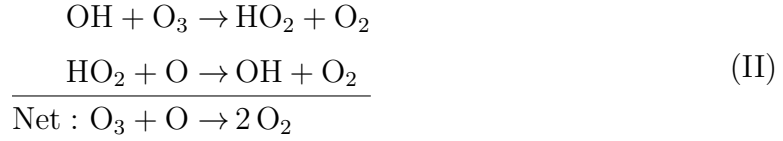
Ozone in the stratosphere is naturally formed by the photolysis of the oxygen molecules by absorbing the UV radiation. The formation and destruction reaction pathways of the stratospheric ozone are first proposed by Chapman [68], which is then named as “Chapman mechanism”:



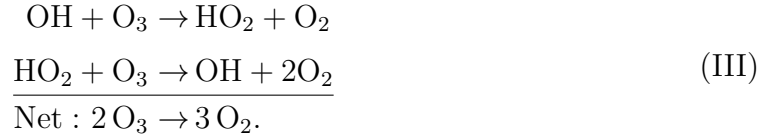
The UV light dissociates the oxygen molecules, forming two oxygen atoms. Ozone is then produced through the reaction between the oxygen atoms and O₂ in the presence

of the third body, M. The reaction between O_3 and oxygen atoms removes the ozone from the system, which is considered as the principle ozone depletion chemical pathway in the stratosphere. However, it is found by Johnston and Whitten [69] that the amount of ozone observed in the stratosphere is only half of the value predicted by the Chapman mechanism. Thus, some additional ozone destruction reaction pathways should exist.

The ozone destruction cycles associated with hydroxyl radicals (OH) in the stratosphere are first identified by Bates and Nicolet [70]:

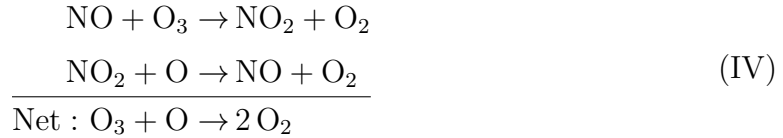


and

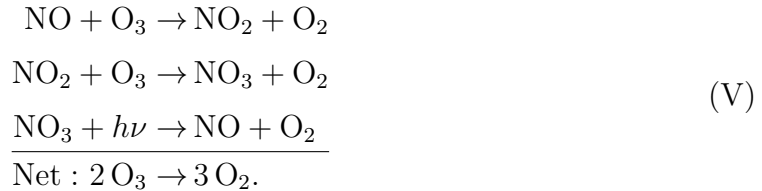


In these two cycles, OH plays as a catalyst, leading to the removal of the ozone in the stratosphere.

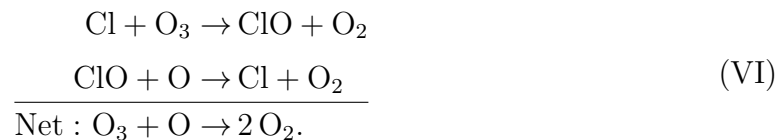
Apart from these two ozone destruction cycles by OH, the role of the nitrogen oxides for consuming ozone in the stratosphere is also discovered in the 1970's by Crutzen [71] and Johnston [72]. Two different chemical reaction cycles are suggested. In the upper stratosphere, the chemical reaction cycle



is important as a large amount of the oxygen atoms is found in the upper stratosphere due to the radiation. In the lower stratosphere, without the presence of the oxygen atoms, the chemical reaction cycle (V) involving NO_3 is more effective:

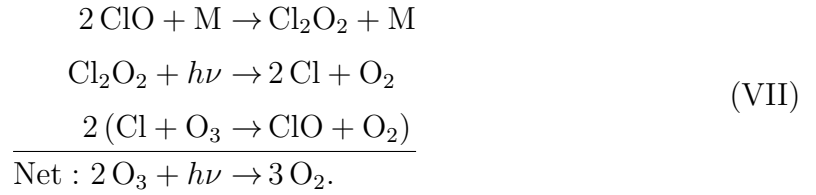


The halogen species, especially chlorine, are also involved in an ozone destruction cycle in the stratosphere:

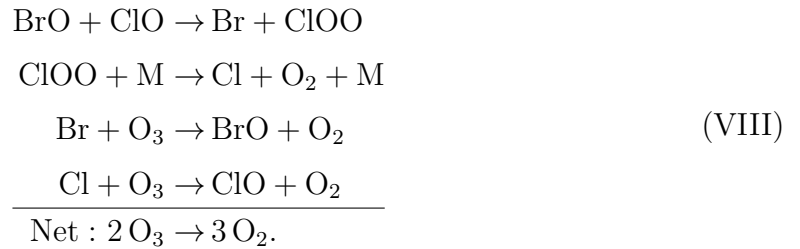


This reaction cycle is very rapid that the chlorine atom has a lifetime of only about 0.2 s [73]. Each chlorine atom can destroy about 10^5 ozone molecules until it reacts with other chemical species, which is the termination of the reaction cycle (VI). The coupling of the hydroxyl radicals, nitrogen oxides, bromine oxides with the chlorine oxides also leads to the ozone depletion by different reaction pathways in the regions with less amount of the oxygen atoms [1].

For the observed ozone hole in the Antarctic, a chemical reaction mechanism associated with the halogen oxides was first proposed by Molina and Molina [74]:



Moreover, BrO can participate in similar reaction cycles, leading to the ozone destruction. A bromine-chlorine coupling chemical reaction cycle (VIII) has also been proposed by McElroy et al. [75] and Tung et al. [76]:



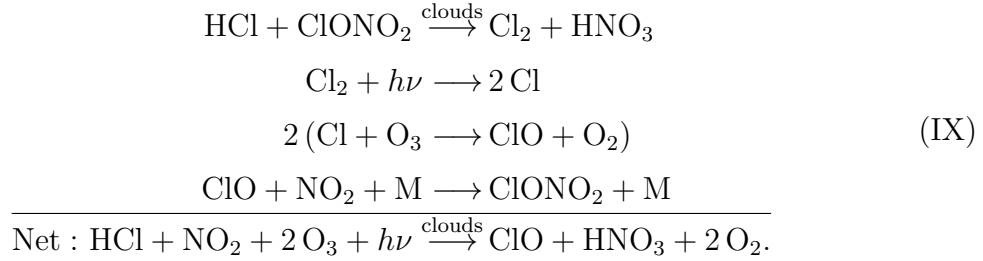
The reaction $\text{BrO} + \text{ClO}$ in the chemical reaction cycle (VIII) has many branches, such as producing OClO or BrCl . These products rapidly decompose in the presence of the third body, M, or the sunlight, forming halogen atoms and leading to a substantial ozone depletion.

However, due to the low intensity of the solar radiation in the polar regions, the photodissociation of the oxygen molecules is suppressed. Thus, the gas-phase reactions in the stratosphere involving oxygen atoms could not produce sufficient BrO and ClO for the chemical reaction chain of (VII) and (VIII) to proceed. A heterogeneous reaction occurring at the surface of the polar stratospheric clouds between HCl and ClONO_2 is explored by Solomon et al. [25] (“S” in the reaction number denotes “stratosphere”):



In this heterogeneous reaction, the gas-phase HCl in the stratosphere is easily absorbed by the polar stratospheric clouds. On the surfaces of the cloud particles, the gaseous ClONO_2 react with HCl, leading to the liberation of the chlorine from these chlorine

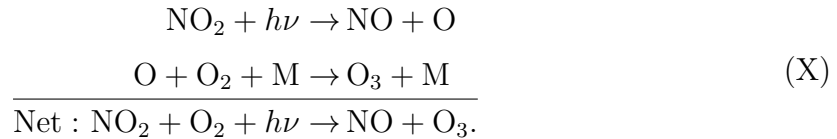
reservoir species HCl and ClONO₂. The Cl₂ molecules generated in this heterogeneous reaction can photolyze, which results in the following heterogeneous ozone destruction cycle (IX) responsible for the Antarctic ozone hole:



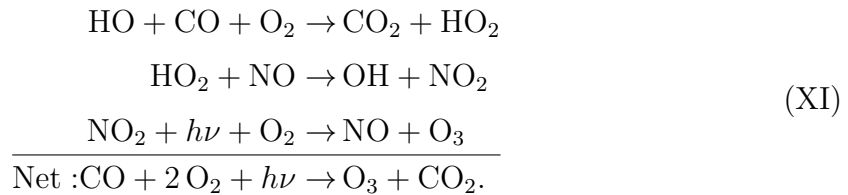
In cycle (IX), ozone is consumed in the presence of the sunlight and the polar stratospheric clouds, which are usually formed in a very low temperature. This explains the reason why the ozone holes are found in polar regions [25].

2.1.2 The Reactions of Ozone in the Troposphere

On average, about 10% of the ozone in the troposphere originates from the vertical downward entrainment from the stratosphere [77]. The annual average ozone flux from the stratosphere to the troposphere is of the order of 10^{13} mol. Moreover, ozone in the troposphere can also be generated through the chemical reaction cycle (X) involving the nitrogen oxides (NO and NO₂):



In reaction cycle (X), NO and O₃ are formed in the presence of the sunlight and NO₂. However, most of the nitrogen oxides in the air emission pollutants is in the form of NO instead of NO₂. Thus, cycle (X) is not able to fully explain the observed concentration of ozone in the troposphere. The reaction cycle (XI) associated with the carbon monoxide (CO) is suggested:



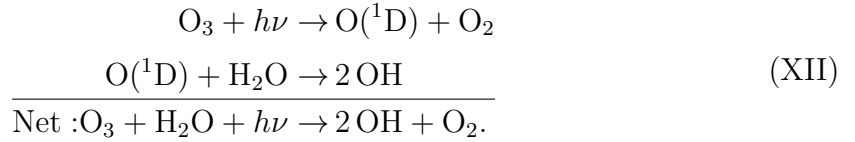
Many VOCs such as the methane (CH₄) can react with the hydroxyl radical HO in a similar way. The generated peroxy radicals may replace HO₂ to oxidize NO to NO₂ but through a more complex chemical system. It is estimated that 70% of the local

chemical production of the ozone in the troposphere is formed through the reaction $\text{HO}_2 + \text{NO}$, and about 20% via the reaction $\text{CH}_3\text{O}_2 + \text{NO}$ [77]. In the regions with less amount of NO_x , the rate determining step of cycle (XI) is the conversion step from NO to NO_2 . When NO_x concentrations are sufficiently high, the production of ozone depends on the CO or VOCs concentration in the air. The CO , NO_x and VOCs in the troposphere are mostly produced from the emission of the motor vehicles and the industrial processes, thus, the ozone mixing ratios in the troposphere are relatively high in the regions with a large population or in the heavy industrial areas.

The deposition on the earth's surface causes about 20% of the ozone reduction in the troposphere [77]. The deposition rate depends on the intensity of the turbulent mixing, types of the surface and the climate conditions such as the temperature and wind speed. Apart from the deposition, chemical reaction pathways also exist for the ozone loss in the troposphere. These chemical reaction pathways include (note that the reaction numbers refer to the mechanism in the appendix B of the thesis):



and



Similar as in the stratosphere, it is also found that the halogen species are involved in an ozone depletion process in the lowest part of the troposphere. In contrast to the stratosphere, where chlorine plays an important role, in the troposphere, bromine is more dominant. A strong correlation between a rapid ozone depletion and high levels of bromine in the regions with high latitude has also been confirmed since the measurements conducted at Alert, Canada in the year 1986 [32]. The chemical reaction cycles involving halogen containing compounds are also suggested by Barrie et al. [32] and summarized by Platt and Hönniger [78], Simpson et al. [79] and Abbatt et al. [80]. This ozone depletion event and the following enhancement of the halogen mixing ratios are the major focus of this study. Thus, it is discussed in more details in the next section.

2.2 Ozone Depletion Event in the Polar Spring

Polar regions, which consist of Arctic and Antarctic, are the parts of the globe near the poles. The Arctic region is located in the north polar ocean and it includes several islands. Antarctic, or the south pole region, is a widely ice-covered continent. Because of

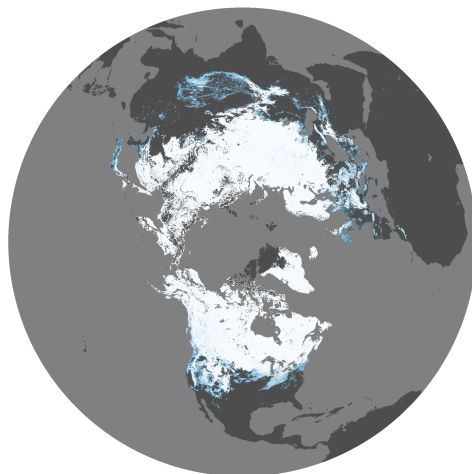


Figure 2.1: Snow cover in the Arctic in February 2009. White regions denote where the ground was totally covered by snow, blue shows places where snow was observed [16].

the unique weather conditions in the polar regions, it is possible to study the chemical processes and the air motions in the polar regions under highly simplified conditions without being affected by the human activities. Therefore, the polar regions are often called the “natural laboratory”. The special weather conditions of polar regions include:

- cold: the average temperature in polar regions is less than 283 K and the lowest temperature, which has been detected is 184 K in the Antarctic. Due to the low temperature, snow and ice in polar regions can stay for several months or even the whole year. Thus, polar regions are mostly covered with ice and accumulating snow. According to the observations, 60% of the Arctic and more than 98% of the Antarctic is snow- or ice-covered (see Fig. 2.1).
- dry: the humidity in polar regions is low because the cold air is unable to hold as much moisture as the warm air. In summer time, it is possible that the humidity in some polar regions especially the parts near oceans increases. However, after summer has passed, the temperature becomes lower so that the ocean surface is frozen and covered by the sea ice, the water evaporation from the ocean is retarded, leading to a decline of the air humidity.
- unpolluted environment: there is low pollution in polar regions. NO_x species ($\text{NO} + \text{NO}_2$) for example, instead of being produced from the reaction of nitrogen and oxygen gases in large cities with the high motor vehicle traffic, originate in polar regions mostly from the photolysis of nitrate in the snow pack. The typical

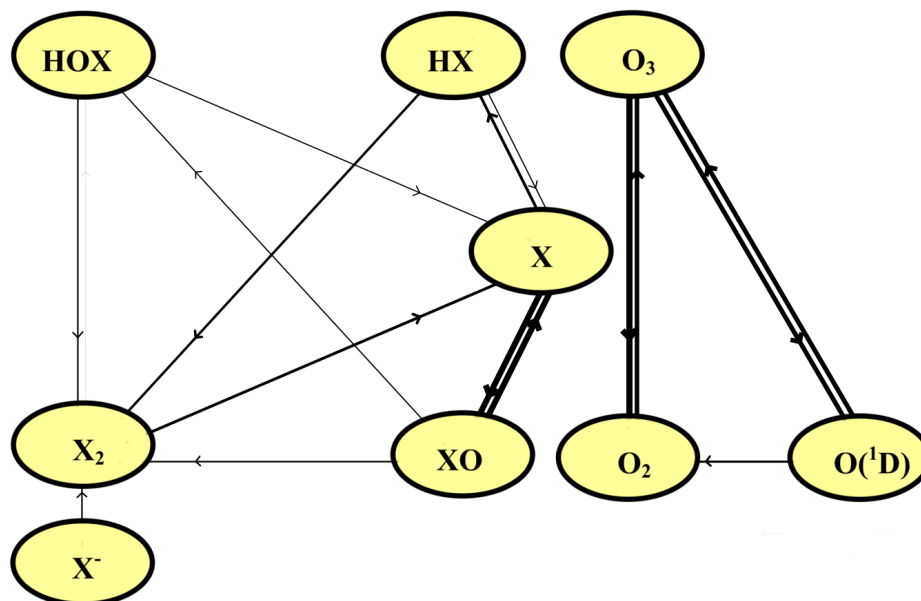


Figure 2.2: A sketch for halogen chemistry (plotted using Fluxviewer, available at [81], the thickness of the arrows connecting the species boxes denotes the typical reaction rate).

mixing ratio of NO_x is less than 100 ppt (ppt = parts per trillion) in both the Arctic and Antarctic.

The typical mixing ratio of ozone in the polar regions is 30-40 ppb on average. Excluding the vertical downward entrainment from the stratosphere and the natural chemical ozone production cycles as discussed above, the long-term transport from the low-latitude regions also enhances the ozone concentration in the polar troposphere. However, it is found that the ozone mole fraction in the polar boundary layer may reduce from the background mixing ratio to a near zero value within several hours or days in the spring season. During this ozone depletion event, the chemical pathways including halogen species (Br, Cl, I) become important, which changes the lifetime of the chemical species and the final products of the chemical reactions in the atmosphere.

It is suggested by Wayne et al. [82] and Le Bras and Platt [83] that the halogen species are involved in an auto-catalytic chemical cycle, leading to the ozone depletion. A schematic diagram for halogen chemistry is shown in Fig. 2.2. It is seen in Fig. 2.2 that the primary reaction for connecting the halogen cycle and the ozone cycle is related to the active atomic halogen radicals, reacting with ozone and forming halogen oxide as following (the reaction numbers correspond to the mechanism in the appendix B):



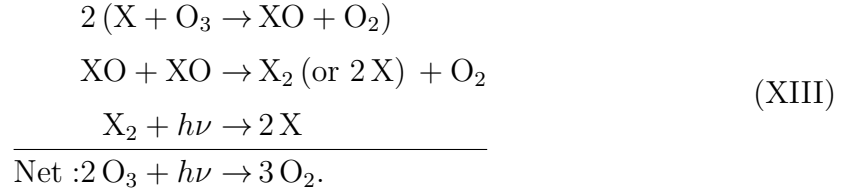
The produced halogen oxide molecules photolyze in the presence of the sunlight:



Ozone is destructed through reactions (R4) and (R92). However, the total ozone stock in the air is not consumed because ozone is regenerated from reactions (R6) and (R132). To destruct ozone, the active halogen radicals must be produced from halogen oxide without any ozone production. Thus, the self reactions of halogen oxide are suggested by Wayne et al. [82]:



By including the photolysis reactions of X_2 , an auto-catalytic photochemical cycle (XIII) is concluded as:



In cycle (XIII), the tropospheric ozone is converted to oxygen without any loss of halogen, and the halogen species act as a catalyst.

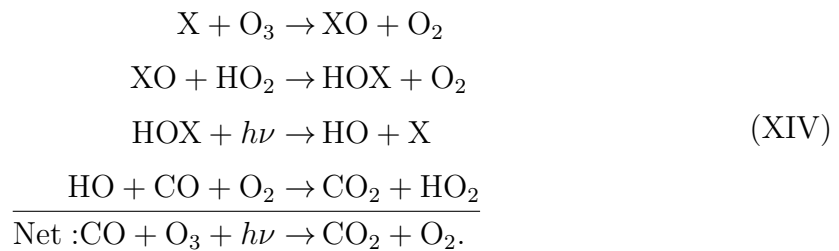
Another branch of the chemical reaction mechanism is that HO_2 in the natural atmosphere may oxidize XO , forming HOX :



HOX is an important reservoir of inorganic halogen species and short-lived (photolysis lifetime ~ 10 min for the case of $\text{X}=\text{Br}$). Active halogen atoms are formed by the photolysis of HOX :

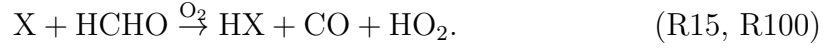


Ozone depletion cycle (XIV) involving HOX is then obtained:



The efficiency of cycle (XIV) is limited by the conversion of XO to HOX due to the small amount of HO₂. Thus, cycle (XIV) is more effective in the regions with less amount of the reactive halogen species [78].

Hydrogen halides can be produced from the reaction of formaldehyde or other aldehyde with reactive halogen atoms:



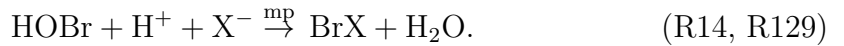
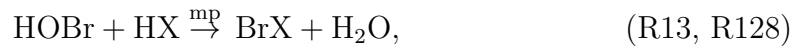
An analogous reaction involving HO₂ also occurs:



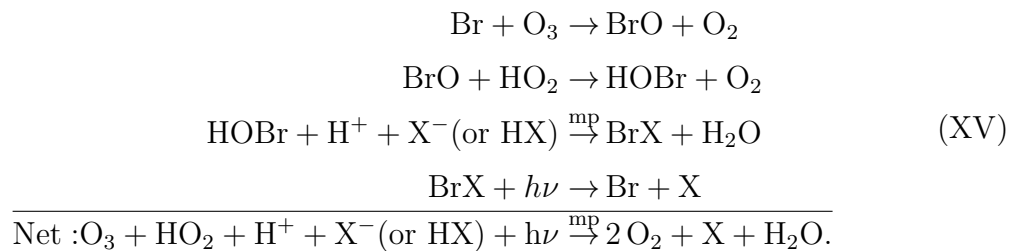
Because of the relative short lifetime of XO (e.g. ~ 100 s for bromine monoxide), most of the reactive halogen species are finally converted to hydrogen halides. Since hydrogen halides are difficult to photolyze and easily absorbed by the sea salt aerosols in the troposphere, the halogen atoms in the hydrogen halides are irreversible. The only gas phase reactions for reforming active halogen species from HX are



However, the natural concentration of the tropospheric HO (about 10^6 molecules cm⁻³) is too small to maintain the large reactive halogen concentration during the ozone depletion event. Besides, all these chemical cycles mentioned before can not enhance the total halogen stock in the air, which contradicts the detections of a large increase of halogen concentration in polar regions during the ozone depletion event [42, 44, 45, 46, 47, 48, 51, 52]. Therefore, a recycling process is needed for activating the inert halogen species. It is concluded that the heterogeneous reactions involving HOBr are responsible for this activation process (“mp” stands for “multiphase reaction”, i.e. reactions at the aerosol and at the ice/snow surface) [84, 85, 86]:

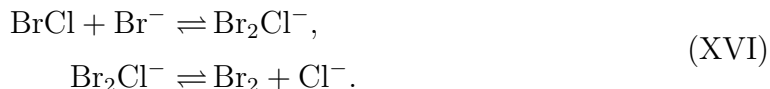


Hence, the chemical cycle (XV) including heterogeneous reactions is gained:



By absorbing gaseous HOBr and HX, the aerosols containing high concentrations of sea salt can offer a possible location for reactions (R13) and (R128) [87]. Active halogen species BrX are reformed at the aerosol surface and then enter the surrounding environment. However, Impey et al. [88] stated that the typical polar sea salt concentration is not enough to support very high frequent activation processes. Thus, it is not possible for the aerosols alone to maintain the large amount of the reactive halogen species in the atmosphere. The new-formed sea ice is likely another major source of halogen species through reactions (R14) and (R129) [89]. The fresh ice contains a great deal of deposited sea salt by freezing processes. The frost flowers on the ice also enhance the surface area because of their sharp angular features [90]. According to Staebler et al. [91], the surface area offered by fresh sea ice for the heterogeneous reaction is more than 1000 times the sea salt aerosol surface area. The activation of inert halogen ions through these heterogeneous reactions also explains the reason for the excessive halogen detection in ozone depletion event. In the case of X=Br, each effective collision of one HOBr molecule at the surface leads to one Br₂ molecule liberation, causing an exponential increase of bromine mixing ratio in the atmosphere and significant speed up of the ozone depletion. This phenomenon is known as the “bromine explosion” [53, 54, 55].

The production rates of BrCl and Br₂ through heterogeneous reactions, (R13, R128) and (R14, R129) are limited by the ion concentrations. As Koop et al. [92] estimated, the ratio of the Cl⁻ and Br⁻ concentrations in the deposited aerosols under typical polar conditions is 188:1. However, the detected gaseous BrCl mixing ratio in the atmosphere approximately equals the value of Br₂. The reason is that after the effective collision between HOBr molecules and aerosol surface, most of BrCl molecules generated at the surface will undergo the following secondary heterogeneous reactions [86]:



The overall production ratio of BrCl and Br₂ is within the range of 0.7 to 1.4 [93, 94].

In the Arctic, a small amount of NO_x may exist, which originates from the nitrate contained in the snow, and this NO_x may have a strong impact on the ozone depletion. The NO_x species can modify the ozone concentration by a variety of paths.

1. The active halogen atoms may be formed from the reaction between halogen oxide and NO:



The active halogen atoms formed in reactions (R80) and (R114) consume ozone via reactions (R4) and (R92). However, when NO₂ photolyzes (lifetime ~100 s),

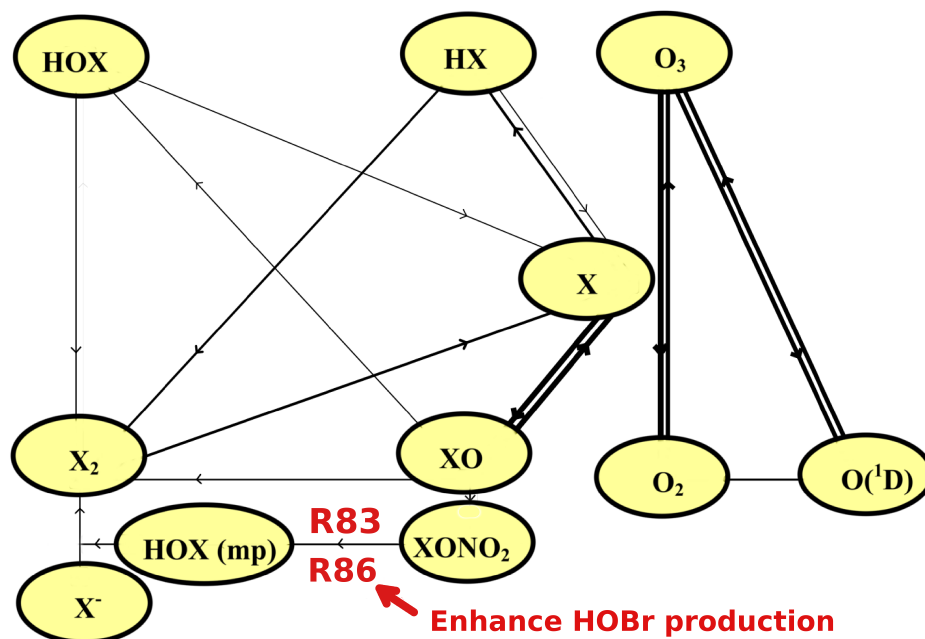


Figure 2.3: A sketch of the pathway for the speeding up of the ozone depletion by NO_x species, the hydrolysis of XONO_2 (reaction R83 and R86) leads to the enhancement of the HOX production, thus accelerating the release of inert X^- ions.

ozone is reformed:



As a result, the net loss of ozone is not contributed by the combination of reactions (R80), (R114) and (R68).

2. NO_x species may help to accelerate the ozone depletion by the processes related to halogen nitrates (XONO_2). The speeding-up ozone depletion pathway is shown in Fig. 2.3. The formation of halogen nitrates and the following hydrolysis decomposition is suggested by Sander et al. [95]:



Halogen nitrates formed through reactions (R79) and (R115) are usually thermally stable, but rather easily decomposed by hydrolysis at the sea salt aerosol surface or the sea ice surface through reactions (R83) and (R86), producing HOX and HNO_3 . The HNO_3 photolysis reaction rate at the aerosol surface is suggested

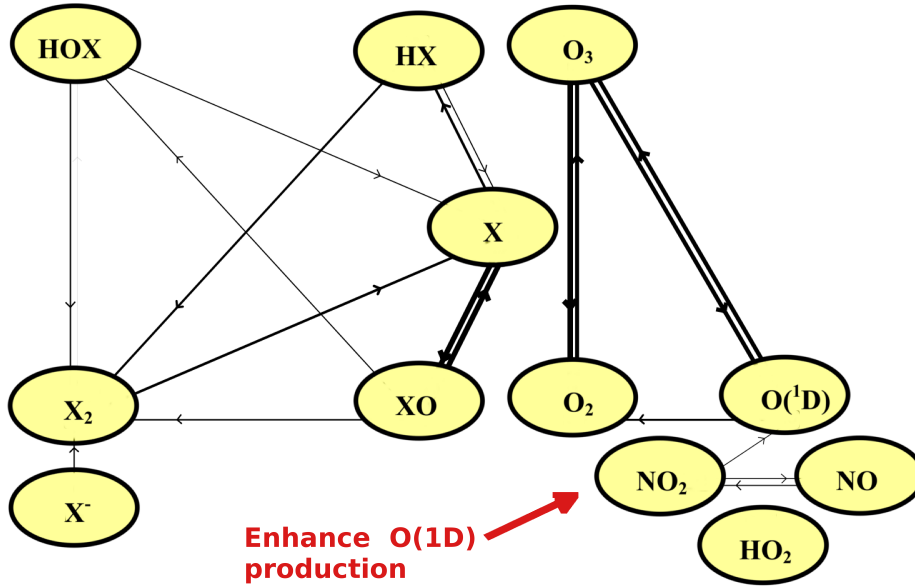
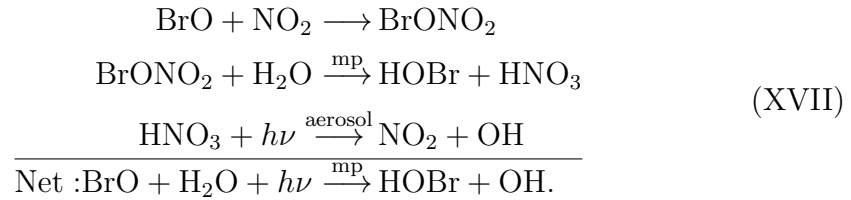


Figure 2.4: A sketch of the pathway for the ozone production by NO_x species, the photolysis of NO_2 enhances the production of $\text{O}(^1\text{D})$, thus speeding up the ozone formation.

by Finlayson-Pitts [96] to be faster than that in the gas phase. As a consequence, in the case of $\text{X}=\text{Br}$, the reaction cycle (XVII) is obtained as follows:



In cycle (XVII), the production of HOBr is enhanced, which is seen in Fig. 2.3. Hence, more effective collisions will occur between the HOBr molecules and the ice surface. Because of the “bromine explosion” mechanism, an additional gaseous bromine flux is released into the air, speeding up the ozone depletion process.

3. NO_x species can also take part in an ozone production cycle (XI), which was discussed before. This ozone production pathway is shown in Fig. 2.4.

Overall, the net effect on ozone depletion caused by NO_x species results from the balance between the cycle (XI) and (XVII). If the additional bromine flux induced by cycle (XVII) is strong enough, the additional amount of ozone depleted through cycle (XVII) is more than the part of ozone formed through cycle (XI). In that situation, NO_x species tends to accelerate the whole ozone depletion event, and vice versa.

2.3 Types of Boundary Layers

The tropospheric ozone depletion events reported in polar regions are mostly accompanied with a stable boundary layer. The boundary layer is the lowest part of the troposphere, see Fig. 1.1. It is directly affected by the change of the overlying surface. The definition of the boundary layer is “that part of the troposphere that is directly influenced by the presence of the earth’s surface, and responds to surface forcing with a time scale of about an hour or less” [97]. Depending on the effects brought by buoyancy, the boundary layer can be divided into three major categories:

- convective (mixed) boundary layer,
- neutral (residual) boundary layer,
- stable boundary layer.

The typical vertical velocity and temperature profiles for convective and stable boundary layers are illustrated in Fig. 2.5. The potential temperature $\Theta = T(\frac{p_0}{p})^{(R/c_p)}$ is used here. T is the absolute temperature, p denotes the local pressure and p_0 is a standard reference pressure. R is the gas constant of air, and c_p is the specific heat capacity at a constant pressure. The potential temperature represents the temperature needed for an air parcel adiabatically carried to the standard reference pressure p_0 . The potential temperature is not affected by the lifting or sinking of the air parcels. Therefore, it is a measure of the stability of the atmospheric layers.

It can be seen in Fig. 2.5(a) that in the convective boundary layer, the ground surface is warmer than the atmosphere above. Therefore, the air near the ground is heated and repelled upwards. The overall effect of the buoyancy is to force the air parcel to displace from its original location, leading to an enhancement of the vertical mixing. Thus, large scale structures are observed in the convective boundary layer, such as plumes and updraft curtains [97]. Because of the strong turbulent mixing, a well-mixed layer is formed in the middle portion of the convective boundary layer. In this well-mixed layer, the potential temperature, wind speed, humidity and pollutant from the ground are almost uniformly distributed, which can be seen from Fig. 2.5(a).

When the potential temperature of the ground surface equals the one in the surrounding gas, the neutral boundary layer forms. In the neutral boundary layer, buoyancy plays no effect. The mixing is only dominated by the wind shear and the intensity is nearly isotropic.

When the warm air is transported over the cold surface, a stable boundary layer is formed. This is often observed at nights or in the polar regions with low wind speed and clear sky. In the stable boundary layer, as shown in Fig. 2.5(b), the surface has a lower potential temperature than the air above the surface. This temperature inversion

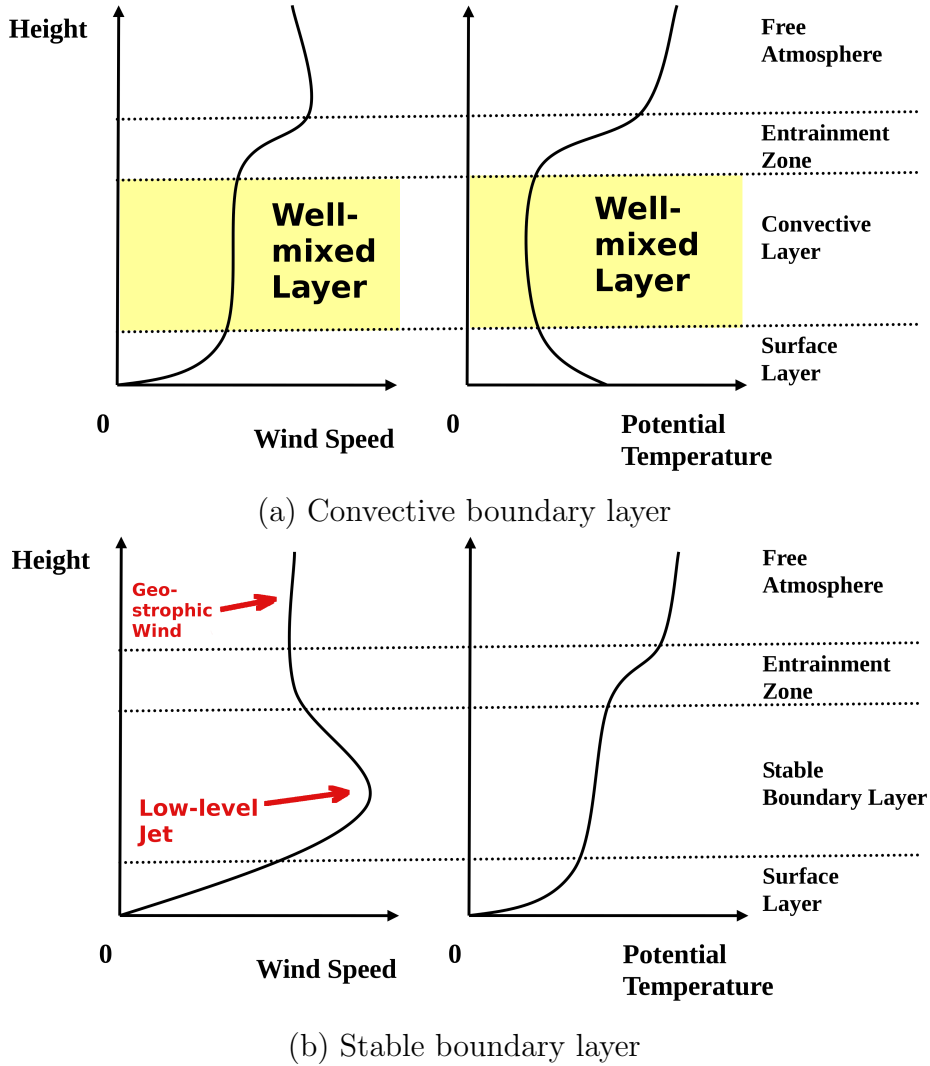


Figure 2.5: Vertical distributions of wind speed and potential temperature in the convective and stable boundary layer (after Stull [97]).

tends to suppress the turbulent mixing. Thus, the effect of the buoyancy in the stable boundary layer is to play against the turbulent mixing generated by the wind shear. Fig. 2.5(b) also shows that below the top of the stable boundary layer, the peak of the wind speed is larger than the geostrophic wind speed, which is formed with the balance between the vertical pressure gradient and the Coriolis force. This super-geostrophic wind speed is called “low-level jet”. Due to the suppression of the vertical mixing by the temperature inversion, instead of the large scale structures in the convective boundary layer, small eddies are detected in the stable boundary layer. This typical characteristic of the small structures in the stable boundary layer adds the difficulty for the numerical simulation, since it requires a finer mesh resolution.

2.4 State of the Art

In order to improve the understanding of the ozone depletion event in polar spring, many model studies have been conducted since the 1990's. Box models are first used. In the box model, or called 0-D model, the chemical species are assumed to be distributed uniformly within the computational domain. The horizontal and vertical mixing is also assumed to be very rapid. In the box model studies [85, 98, 93], the temporal evolutions of the chemical species during the ozone depletion event and the recycling of the halogen species are investigated. The triggering of the ozone depletion event is also studied [99, 100, 101], and the precipitation of calcium carbonate (CaCO_3) is proposed as the key triggering factor. Liao et al. [102] pay attention to the impact of BrO on the concentration of hydroxyl radicals during the ozone depletion event. The principal sources of NO_x and HO_x radicals are studied by Bloss et al. [103] using the data from the observations [104] performed in the coastal Antarctic boundary layer.

Moreover, models with higher dimension are developed. The one-dimensional model proposed by Lehrer et al. [105] aims to determine the primary source of reactive halogens, and they suggest the sea ice surface to be the major source of reactive bromine. The one-dimensional model called MISTRA-SNOW [106, 107] is the first model to couple a snow module with a one-dimensional boundary layer model MISTRA [108, 109, 110], highlighting the importance of the boundary layer height and the NO_x emission fluxes from the snow pack. The chemical processes related to BrO and ozone are first incorporated in a three-dimensional model by Zeng et al. [111, 112], estimating the ozone depletion based on the BrO concentrations derived from satellite VCD (vertical column density) observations.

Different sources of reactive halogens are studied by using different models. Zhao et al. [113] developed a global three-dimensional model, stating that the aerosols derived from frost-flowers might be the major source of reactive halogens. The possibility for the snow particles lifted by wind in a stormy blowing-snow condition to be a major source of bromine during the ozone depletion event is discussed [114, 115]. Later, the measurements conducted by Jones et al. [116, 117] in the Antarctic confirm the important role of the blowing snow in ozone depletion event, and Jones et al. conclude that the ozone depletion event occurs more likely in low wind speed, shallow stable boundary layer conditions or high wind speed, blowing snow conditions. Different 1-D models are used by Toyota et al. [118, 119] to analyze the air-snow pack interaction, and Toyota et al. suggest the snow pack as the potential source.

However, all the models mentioned above have their drawbacks. The models with lower dimension always include a prescribed value of the turbulent diffusivity in the boundary layer. On the contrary, the higher dimension models mostly include a very simple treatment of the chemical reactions.

Thus, in order to study the underlying physical and chemical processes of the ozone depletion events, an integral three-dimensional model is developed by considering a skeletal chemical reaction mechanism and environmental physical properties such as the wind and turbulent mixing. It is assumed that the saline snow/ice surface is the major source of the halogen species. HOBr molecules from the overlying atmosphere collide with the saline surface, leading to the liberation of Br_2 and BrCl from the surface back to the surroundings. Moreover, the heterogeneous reactions occurring at the aerosol surfaces are included for re-activating the inert halogen from the hydrogen halides. The strategy of this study is as follows:

1. Investigate the detailed chemical reaction mechanism in a box model, capturing the time behavior of the major chemical species such as O_3 , BrO and HOBr .
2. Identify the significance of each chemical reaction and transport features by a sensitivity analysis.
3. Based on the results of the sensitivity analysis, the detailed chemical reaction mechanism is reduced, and a skeletal mechanism is derived for the three-dimensional simulations – assure that the main features are maintained.
4. Perform a three-dimensional large eddy simulation with the skeletal mechanism under realistic weather conditions. Different shapes of the bottom surface are used to study the impact on the ozone depletion caused by the topographic change.

3. Model Description

As mentioned above, at first, a box model is used to capture the temporal evolutions of the major chemical species for different chemical reaction schemes. In the present model, three chemical reaction schemes are investigated. The parameterized heterogeneous reactions are included in the chemical reaction mechanism and the effect caused by the change of the weather conditions is studied. The relative importance of specific reactions and their rate constants is identified by a sensitivity analysis. Some reactions can be removed from the mechanism according to the sensitivity analysis. The derived skeletal mechanism is then implemented into a three-dimensional unsteady model to describe the tropospheric ozone depletion in polar regions. The transport of the air parcels and vertical turbulent mixing are modeled using large eddy simulation (LES).

3.1 Box Model

The box model is constructed by using the open-source chemical kinetic software KINAL (KInetic aNALysis of reaction mechanics) [120]. KINAL is able to calculate stiff ordinary differential equations in the form of

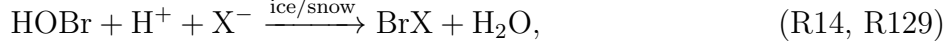
$$\frac{d\vec{c}}{dt} = \vec{f}(\vec{c}, \vec{k}). \quad (3.1)$$

Equation (3.1) represents complex chemical reaction system. \vec{c} denotes the column vector of species concentrations. \vec{k} and t are the vector of the reaction rate constants and the physical time, respectively. A fourth-order semi-implicit Runge-Kutta method is used for the solution of Eq. (3.1).

Different chemical reaction schemes are implemented in the box model. The reaction rates are calculated at $T = 258$ K at atmospheric pressure, and the reactions are listed in Appendix B. Three different detailed chemical reaction schemes are studied. The first one concerns bromine as the only halogen species in the mechanism. The second reaction scheme is an extension of the first one, where nitrogen containing species are added, and the third chemical reaction scheme also includes chlorine reactions.

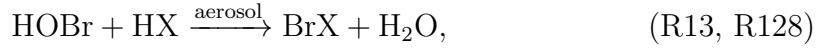
3.1.1 Parameterization of the Heterogeneous Reactions

In the present chemical reaction mechanism, the total halogen loading in the atmosphere is determined by the heterogeneous reactions



where (R14) refers to $\text{X}=\text{Br}$ and (R129) to Cl . These heterogeneous reactions occur at the sea ice surface covered by snow. The inert halogen ions are activated from the fresh sea ice, leading to the increase of the halogen concentrations in the air.

Moreover, the liquid aerosols offer a possible location for (R13) and (R128) by absorbing gaseous HOBr and HX [87]:



where (R13) refers to $\text{X}=\text{Br}$ and (R128) to Cl . In these two reactions, active halogen species BrX are reformed from HX at the aerosol surface and emitted into the surrounding environment. Since these heterogeneous reactions heavily affect the halogen concentrations in the atmosphere, it is essential to precisely parameterize the multi-phase reaction rates.

3.1.1.1 Heterogeneous Reactions for Aerosols

According to Schwartz [121], the production rate of Br_2 molecules for (R13) is given as

$$\frac{d[\text{Br}_2]}{dt} = -\frac{d[\text{HOBr}]}{dt} = k_{\text{R13}}[\text{HOBr}] \quad (3.2)$$

with the first-order heterogeneous reaction rate constant

$$k_{\text{R13}} = \left(\frac{a}{D_g} + \frac{4}{v_{\text{therm}}\gamma} \right)^{-1} d_{\text{eff}}. \quad (3.3)$$

The term a/D_g in Eq. (3.3) represents the molecular diffusion limit, where D_g is the molecular diffusivity in the gas phase. In the present model, $D_g = 0.2 \text{ cm}^2 \text{ s}^{-1}$, and $a = 0.45 \text{ }\mu\text{m}$ is the typical aerosol radius [105]. The remaining contribution on the RHS of Eq. (3.3) accounts for the collision frequency at the surface. The molecular mean speed v_{therm} of HOBr is given by $v_{\text{therm}} = \sqrt{\frac{8RT}{\pi M_{\text{HOBr}}}}$, where M_{HOBr} is the molar mass of HOBr. R is the universal gas constant and T is the absolute temperature (258 K in the model). γ in Eq. (3.3) denotes the uptake coefficient of HOBr on sea salt aerosols. Considering Eq. (3.3), it is seen that for aerosols with low γ , thermal collision induced reactions are favored, whereas in case of a high value of γ , there will be limitations due to diffusion.

The surface-volume coefficient, d_{eff} , is the ratio of the total aerosol surface area, A_{aerosol} , and the total volume of the model, V_m [122]:

$$d_{\text{eff}} = \frac{A_{\text{aerosol}}}{V_m}. \quad (3.4)$$

The value of the uptake coefficient, γ , and the surface-volume coefficient, d_{eff} , for heterogeneous reaction rate of (R13) and (R128) must be evaluated.

The evaluation of γ and d_{eff} is similar to the one used in Lehrer et al. [105] and Cao et al. [122]. For reaction (R13), the production of Br_2 is limited by the absorption of both gaseous HOBr and HBr in the suspended aerosol particles. The HOBr uptake coefficient γ to the bulk of liquid phase can be expressed in the form of Eq. (3.5) according to Hanson et al. [123]:

$$\frac{1}{\gamma} = \frac{1}{\alpha} + \frac{v_{\text{therm}}}{4H^*RT\sqrt{k_{\text{liq}}^{\text{I}}D_{\text{liq}}}f(q)}. \quad (3.5)$$

Here, α is the accommodation coefficient taken to be unity [105] in the present study. The effective Henry constant, H^* , is applied for the species, which can dissociate in the liquid solutions, and it has the value of $1.7 \cdot 10^4 \text{ mol}/(\text{L atm})$ for HOBr. $k_{\text{liq}}^{\text{I}}$ is the first-order liquid reaction rate constant of reaction (R13), and it can be calculated as $k_{\text{liq}}^{\text{I}} = k_{\text{liq}}^{\text{II}} [\text{HBr}]_{\text{liq}} = k_{\text{liq}}^{\text{II}} H_{\text{HBr}}^* P_{\text{HBr}}$ [1]. $k_{\text{liq}}^{\text{II}}$ is the second-order liquid reaction rate constant, and its value is $5 \cdot 10^4 \text{ L}/(\text{mol s})$. The effective Henry constant of HBr for reaction (R13) has the value of $3 \cdot 10^8 \text{ mol}/(\text{L atm})$ in the model. P_{HBr} is the partial pressure of gaseous HBr. For 10 ppt HBr, $P_{\text{HBr}} = 10^{-11} \text{ atm}$. D_{liq} in Eq. (3.5) denotes the liquid phase diffusion coefficient for HOBr, which is taken to be $5 \cdot 10^{-6} \text{ cm}^2/\text{s}$. The function $f(q)$ equals $\coth(q) - (1/q)$, where $q = a\sqrt{k_{\text{liq}}^{\text{I}}/D_{\text{liq}}}$, and a is the typical aerosol radius. Thus, $\gamma = 0.12$ is obtained for a gas mixing ratio of 10 ppt HBr. If the aerosol particles are assumed to be uniformly distributed, using the data provided by Staebler et al. [91], the aerosol volume concentration is calculated to be $10^{-11} \text{ cm}^3/\text{cm}^3$, and 10^{-6} cm^2 effective aerosol surface area is offered in each cm^3 volume of air, which corresponds to $d_{\text{eff}} = 10^{-6} \text{ cm}^{-1}$. The first-order reaction rate constant for reaction (R13) can then be calculated as $k_{\text{R13}} = 6.14 \cdot 10^{-4} \text{ s}^{-1}$ for 10 ppt HBr mixing ratio.

Considering the chlorine containing mechanism in (R128), BrCl is produced via the corresponding heterogeneous reaction. Similarly, if the HCl mixing ratio is 10 ppt, the first-order reaction rate $1.61 \cdot 10^{-5} \text{ s}^{-1}$ is obtained with $k_{\text{liq}}^{\text{II}} = 10^5 \text{ L}/(\text{mol s})$ and $H^* = 3 \cdot 10^6 \text{ mol}/(\text{L atm})$ for reaction (R128).

3.1.1.2 Heterogeneous Reactions for Ice and Snow Packs

For reaction (R14), in which the ice/snow packs offer the possible reaction site, the change in concentration of HOBr is calculated as

$$\frac{d[\text{HOBr}]}{dt} = -k_{\text{R14}}[\text{HOBr}], \quad (3.6)$$

with the reaction rate constant

$$k_{\text{R14}} = \frac{v_d}{L_{\text{mix}}} \beta. \quad (3.7)$$

The reaction rate constant k_{R14} depends on the deposition velocity, v_d , at the ice/snow surfaces, the typical height of the mixing layer, L_{mix} , and the total reactive surface area offered by ice/snow, which is denoted by a reactive surface ratio coefficient, β [122]. The deposition velocity v_d is governed by the sum of three resistances: the aerodynamic resistance r_a , the quasi-laminar layer resistance r_b and the surface resistance r_c [1]:

$$v_d = (r_a + r_b + r_c)^{-1}. \quad (3.8)$$

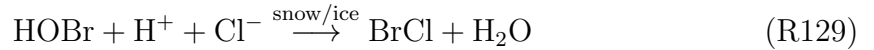
The estimation of the values of the deposition velocity is taken following the work of Huff and Abbatt [124, 125]. The first term on the RHS of Eq. (3.8), r_a , shows the resistance of turbulent transport of bringing the gas from the atmosphere down to the surface, and it is given as $1/(\kappa^2 W)(\ln(z_s/z_0))^2$, where $\kappa = 0.4$ is the von Karman's constant, W is the wind speed for which the value 8 m/s is used [126]. z_s is the height of the surface layer, which is 10% of the boundary layer height. z_0 is the surface roughness length, and 10^{-5} m is used for the ice surface [97, 124, 125]. Thus, the value of r_a depends on the local transport properties (wind speed, boundary layer, ...). The quasi-laminar layer resistance, r_b , represents the ability of molecular diffusion to transfer gas across a liquid-laminar layer above the surface, and it is given as $r_b = z_0/D_g$. r_c is the surface resistance and can be expressed as $4/(v_{\text{therm}}\gamma)$. A constant uptake coefficient of $\gamma = 0.06$ is taken after Sander and Crutzen [87]; this includes the assumption that H^+ and halogen ions are inexhaustible at the ice/snow surface.

L_{mix} in Eq. (3.7) stands for the typical height of the stable boundary layer. Typical magnitudes of the stable boundary layer height observed in polar regions range from a near zero value to over 1000 m [97], depending, for instance, on the wind speed and the temperature inversion intensity. In the present model, different boundary layer heights of 200 m (suggested in Beare et al. [126] and used in Evans et al. [127]), 500 m (used in Oltmans et al. [36]) and 1000 m (used in Lehrer et al. [105]) are considered. The deposition velocity for these three boundary layer heights is 0.605 cm/s, 0.536 cm/s and 0.491 cm/s, respectively. These values are in a reasonable range of the HOBr deposition velocity [87, 128, 129].

A reactive surface ratio coefficient, β , is introduced in Eq. (3.7), representing the ratio of total reactive surface area offered by the ice/snow surface and the flat surface area. For a flat surface of pure ice, β equals unity. However, considering the porous properties of the contaminated snow above the ice surface, larger surface area may be offered by the ice/snow surface. Besides, the surface physical structure and the roughness may also increase the reactive surface area, for instance, through frost flowers because of their sharp angular features [90]. The lifted snow pumped by the wind near the surface may also increase the total reactive surface area. Because of the uncertainty of the reactive surface area offered by the saline surface, a parameter study is conducted with the consideration of a proper range of β .

For $\beta = 1.0$, the reaction rate constant k_{R14} for reaction (R14) is calculated to be $3.03 \cdot 10^{-5} \text{ s}^{-1}$, $1.072 \cdot 10^{-5} \text{ s}^{-1}$ and $4.91 \cdot 10^{-6} \text{ s}^{-1}$ for the boundary layer heights $L_{\text{mix}} = 200 \text{ m}$, 500 m and 1000 m , respectively, if the chlorine mechanism is discarded. All HOBr molecules at the ice/snow surface are converted into Br_2 through reaction (R14), and the Br_2 is emitted into the ambient air.

However, if the chlorine mechanism is added, reaction



competes with (R14) for the HOBr molecules, and the reaction rate ratio, $K_{\text{Br}_2/\text{BrCl}} = k_{\text{R14}}/k_{\text{R129}}$ of reactions (R14) and (R129) determines the formation ratio of Br_2 and BrCl molecules through the heterogeneous activation from the ice/snow pack. The value of $K_{\text{Br}_2/\text{BrCl}}$ varies between 0.8 to 1.4 [94]. Michalowski et al. [93] found that the ozone depletion rate is very sensitive to the production rate ratio of Br_2 and BrCl . Therefore, the relation between the production rate ratio and ozone depletion time is investigated in the present study, whereas the default value is taken to be unity.

3.1.2 Photolysis Reactions

The photolysis reaction rates, J , are evaluated by using a three-coefficient formula, where the surface albedo equals unity [130, 131]:

$$J = J_0 \exp(b[1 - \sec(c\chi)]). \quad (3.9)$$

χ is the Solar Zenith Angle (SZA). The values for the coefficients J_0 , b , c for different chemical species are listed in Tab. 3.1.

In this model, the average photolysis reaction rates are used under the condition of SZA equals 80 degrees. It is found that the variation of SZA has little effect on the temporal evolutions of the ozone and halogen species mixing ratios [105, 122].

Table 3.1: Coefficients for the photolysis reaction rates, see Eq. (3.9). Note that two chemical pathways for the photolysis of NO_3 are possible: (R69) $\text{NO}_3 + h\nu \xrightarrow{\text{O}_2} \text{NO}_2 + \text{O}_3$ and (R70) $\text{NO}_3 + h\nu \rightarrow \text{NO} + \text{O}_2$.

Species	J_0 [s^{-1}]	b	c	Species	J_0 [s^{-1}]	b	c
O_3	$6.85 \cdot 10^{-5}$	3.510	0.820	BrONO_2	$3.11 \cdot 10^{-3}$	1.270	0.859
Br_2	$1.07 \cdot 10^{-1}$	0.734	0.900	BrNO_2	$1.11 \cdot 10^{-3}$	1.479	0.851
BrO	$1.27 \cdot 10^{-1}$	1.290	0.857	BrCl	$3.41 \cdot 10^{-2}$	0.871	0.887
HOBr	$2.62 \cdot 10^{-3}$	1.216	0.861	Cl_2	$7.37 \cdot 10^{-3}$	1.204	0.863
H_2O_2	$2.75 \cdot 10^{-5}$	1.595	0.848	ClO	$1.08 \cdot 10^{-4}$	3.876	0.816
HNO_3	$1.39 \cdot 10^{-6}$	2.094	0.848	HOCl	$7.47 \cdot 10^{-4}$	1.396	0.855
NO_2	$2.62 \cdot 10^{-2}$	1.068	0.871	ClONO_2	$1.29 \cdot 10^{-4}$	1.286	0.861
$\text{NO}_3 \rightarrow \text{NO}_2$	$6.20 \cdot 10^{-1}$	0.608	0.915	OClO	$2.61 \cdot 10^{-1}$	1.058	0.872
$\text{NO}_3 \rightarrow \text{NO}$	$7.03 \cdot 10^{-2}$	0.583	0.917				

3.1.3 Sensitivity Analysis

Even though the detailed chemical reaction schemes perform well in predicting the ozone depletion in the box model, it is not affordable for a three-dimensional simulation since the calculation of the chemical source term is the most time-consuming step in the simulation. Thus, some less important reactions and species should be removed from the detailed chemical reaction mechanism to obtain a skeletal reaction scheme, which can be done by the sensitivity analysis of the detailed chemical reaction mechanism.

In a complex chemical system, it is difficult to see the relative importance of its parts and the features of the kinetic behavior. However, if this information is available, it would help to gain insight and better understanding of the kinetic behavior. In this situation, a sensitivity analysis is helpful to gain deeper knowledge about the chemical reactions system. One element of the local relative sensitivity matrix can be written as

$$S_{ij} = \frac{\partial \ln c_i}{\partial \ln k_j}, \quad (3.10)$$

where c_i is the concentration of i^{th} species and k_j is the rate constant of j^{th} reaction. The concentration sensitivity S_{ij} is a function of time and it represents the effects on the i^{th} concentration change caused by the j^{th} reaction rate change at different time points. Matrix decomposed method [132] is embedded in the subroutine SENS of KINAL for the sensitivity calculation. Before applying the sensitivity analysis for the ozone depletion and halogen explosion mechanism, a validation has been conducted for the Chapman mechanism [68] of atmospheric ozone kinetics in the stratosphere (4

Table 3.2: Relative sensitivities for the Chapman mechanism.

Species	k_1	k_2	k_3	k_4
	$t = 2.5 \text{ s}$			
O	-0.99988E+00	-0.77339E-04	0.14593E-01	0.98537E+00
O ₃	0.42143E-04	-0.88398E-07	0.86352E-05	-0.41538E-04
	$t = 2.5 \times 10^6 \text{ s}$			
O	-0.76157E+00	-0.23841E+00	0.71023E+00	0.76069E+00
O ₃	0.23837E+00	-0.23835E+00	0.70986E+00	-0.23790E+00
	$t = 2.5 \times 10^7 \text{ s}$			
O	-0.50019E+00	-0.49981E+00	0.50019E+00	0.49981E+00
O ₃	0.49999E+00	-0.49999E+00	0.49961E+00	-0.49961E+00

reactions and 3 oxygen related species, see chemical reaction cycle (I) in Chapter 2). The values of the relative sensitivities are shown in Tab. 3.2. The difference between the results in the present analysis shown in Tab. 3.2 and previous studies [132] is smaller than 0.1% of the absolute values, which validates the sensitivity analysis used in the present study.

With the focus on the principal chemical species concentrations (O₃, Br, BrO, HOBr, ...) in the ozone depletion event, the relative sensitivity for each reaction in the mechanism can be studied. Then the reactions with large values of the sensitivity are maintained, and reactions with the lowest sensitivities are removed – this process may also lead to removal of species from the original chemical reaction mechanism. Thus, a skeletal mechanism is obtained, which is implemented in the 3-D computations.

3.2 Three-Dimensional Model

A three-dimensional unsteady model to describe the tropospheric ozone depletion in polar regions is developed using large eddy simulation (LES) with the simplified Smagorinsky subgrid model and the skeletal chemical reaction mechanism. The governing equations are solved using the open source platform OpenFOAM (Open Field Operations And Manipulations [133]).

3.2.1 Configuration

Figure 3.1 shows the schematic of the model configuration. The initial wind blows along the horizontal direction. Due to the friction from the ground and the vertical gradient of

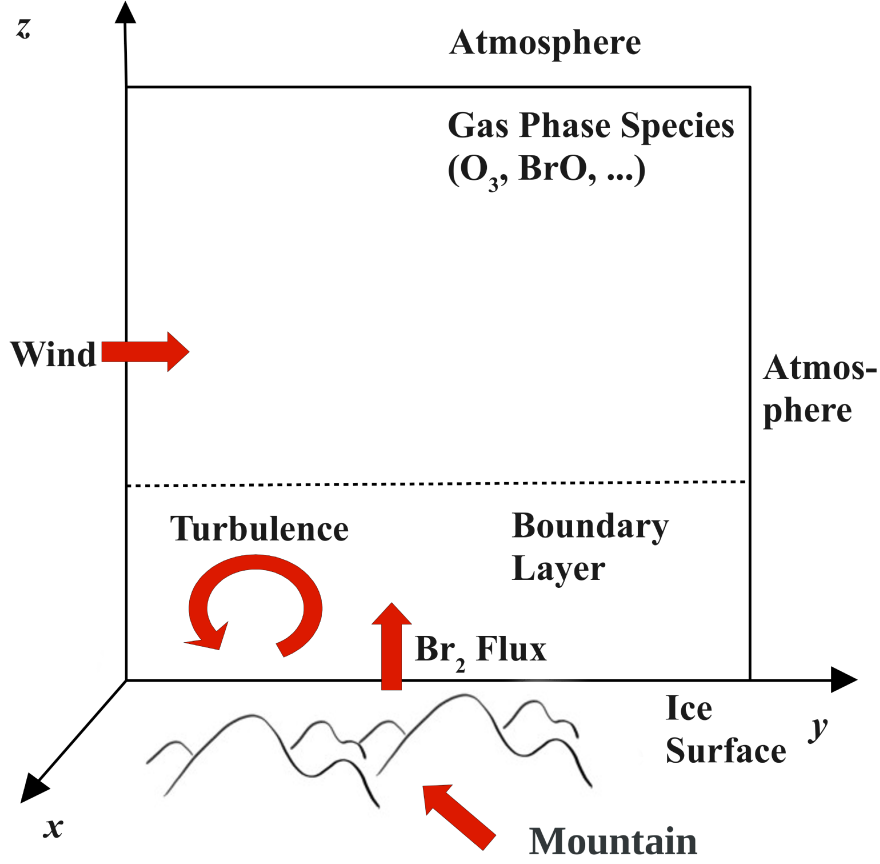


Figure 3.1: Schematic depiction of the model.

the potential temperature, a boundary layer is formed. The halogen fluxes generated through the heterogeneous reactions on the ground are mixed within the boundary layer by the combination of the molecular diffusion and turbulent diffusion, leading to the enhancement of the halogen concentration and the relevant ozone depletion in the lowest part of the troposphere. Two different geometries are used as the bottom boundary of the computational domain, one includes a flat surface on the ground, and another simulation incorporates a mountain located at the surface in order to acquire a better understanding of the ozone depletion event occurring above a non-flat surface.

3.2.2 Governing Equations

The following three-dimensional unsteady compressible Navier-Stokes equations are solved [97, 133, 134]:

- Mass:

$$\frac{\partial \rho}{\partial t} + \nabla \cdot (\rho \vec{U}) = 0 \quad (3.11)$$

- Momentum:

$$\frac{\partial(\rho\vec{U})}{\partial t} + \nabla \cdot (\rho\vec{U}\vec{U}) = -\nabla p - \nabla \cdot \bar{\bar{\tau}} - \nabla \cdot \bar{\bar{\tau}}_t + \rho\vec{g} - 2\rho(\vec{\Omega} \times \vec{U}) \quad (3.12)$$

- Energy:

$$\frac{\partial(\rho h_s)}{\partial t} + \nabla \cdot (\rho\vec{U}h_s) - \nabla \cdot (\rho\alpha_{\text{eff}}\nabla h_s) = \frac{Dp}{Dt} - \sum_{i=1}^N \dot{\omega}_i \Delta h_{f,i}^\circ \quad (3.13)$$

- Mass Fractions:

$$\frac{\partial(\rho Y_i)}{\partial t} + \nabla \cdot (\rho\vec{U}Y_i) - \nabla \cdot (\rho D_{i,\text{eff}}\nabla Y_i) = \dot{\omega}_i, \quad (3.14)$$

where ρ is the air density and \vec{U} is the gas velocity. $\vec{\Omega} = (0, \omega \cos(\phi), \omega \sin(\phi))^T$ is the angular velocity vector of the earth's rotation, where $\omega = 7.27 \cdot 10^{-5} \text{ s}^{-1}$ is the magnitude of the angular velocity of the earth, and $\phi = 73^\circ \text{N}$ [126] corresponds to the latitude. \vec{g} is the gravitational acceleration. h_s denotes the sensible enthalpy and α_{eff} is the effective thermal diffusivity. p denotes the pressure and Dp/Dt is the material derivative of the pressure. $\Delta h_{f,i}^\circ$ is the specific enthalpy of formation and Y_i the mass fraction of species i , respectively. $D_{i,\text{eff}}$ are the effective species diffusivities and $\dot{\omega}_i$ is the reaction rate of species i , where N chemical species are considered. $\bar{\bar{\tau}}$ denotes the viscous stress tensor due to molecular viscosity,

$$\bar{\bar{\tau}} = -2 \mu_1 \bar{\bar{e}}^D, \quad (3.15)$$

where μ_1 is the molecular dynamic viscosity. $\bar{\bar{e}}^D = \bar{\bar{e}} - \frac{1}{3}(\text{tr}(\bar{\bar{e}})) \bar{\bar{I}}$ is the deviatoric part of the rate of strain tensor. The symbol tr denotes the trace of a matrix which is the sum of the elements on the main diagonal of the matrix. $\bar{\bar{I}}$ is the unit dyadic, $\bar{\bar{e}}$ is given as

$$\bar{\bar{e}} = \frac{1}{2}(\nabla\vec{U} + (\nabla\vec{U})^T). \quad (3.16)$$

The subgrid-scale stress tensor $\bar{\bar{\tau}}_t$ consists of two parts: a deviatoric part and an isotropic part:

$$\bar{\bar{\tau}}_t = \bar{\bar{\tau}}_t^D + \frac{2}{3}k_t \bar{\bar{I}}, \quad (3.17)$$

where $k_t = 0.5 \text{ tr}(\bar{\bar{\tau}}_t)$ is the subgrid turbulent kinetic energy. Thus, Eq. (3.12) for momentum can be written as

$$\frac{\partial(\rho\vec{U})}{\partial t} + \nabla \cdot (\rho\vec{U}\vec{U}) = -\nabla \bar{p} - \nabla \cdot \bar{\bar{\tau}} - \nabla \cdot \bar{\bar{\tau}}_t^D + \rho\vec{g} - 2\rho(\vec{\Omega} \times \vec{U}), \quad (3.18)$$

where \bar{p} is the modified pressure $\bar{p} = p + \frac{2}{3}k_t$. With an assumption of a linear subgrid-scale viscosity hypothesis, the deviatoric part of the subgrid stress tensor follows

$$\bar{\bar{\tau}}_t^D = -2 \mu_t \bar{\bar{e}}^D, \quad (3.19)$$

where μ_t is the turbulent dynamic viscosity in the subgrid scale. As a result, the final form of the momentum equation used in this study is

$$\frac{\partial(\rho \vec{U})}{\partial t} + \nabla \cdot (\rho \vec{U} \vec{U}) = -\nabla \bar{p} + \nabla \cdot (2\mu_{\text{eff}} \bar{\bar{e}}^D) + \rho \vec{g} - 2\rho(\vec{\Omega} \times \vec{U}). \quad (3.20)$$

The effective dynamic viscosity μ_{eff} is

$$\mu_{\text{eff}} = \mu_l + \mu_t. \quad (3.21)$$

3.2.2.1 Subgrid Model

The subgrid dynamic turbulent viscosity is computed as [135, 136]:

$$\mu_t = \rho c_k \Delta \sqrt{k_t}. \quad (3.22)$$

In the model, the filter width, Δ , equals (grid size)^{1/3}. According to Yoshizawa [137] and Fureby [136], a balance equation for k_t is derived:

$$\frac{\partial(\rho k_t)}{\partial t} + \nabla \cdot (\rho \vec{U} k_t) = -\nabla \cdot (2\mu_{\text{eff}} \nabla k_t) - \rho \bar{\bar{e}} : \bar{\bar{\tau}}_t - \rho c_e k_t^{\frac{3}{2}} \Delta. \quad (3.23)$$

The first term on the right-hand side of Eq. (3.23) denotes the diffusion of the subgrid kinetic energy. The second and third terms represent the production and dissipation of the subgrid kinetic energy.

The Smagorinsky model [138] is used as the subgrid model in this study. The Smagorinsky model is based on the local equilibrium assumption, it is assumed that the rate of energy transfer from the filtered scale to the residual scale equals the dissipation rate of k_t . In this situation, in Eq. (3.23),

$$-\rho \bar{\bar{e}} : \bar{\bar{\tau}}_t = \rho c_e k_t^{\frac{3}{2}} \Delta. \quad (3.24)$$

Using the condition of Eq. (3.22), the relation

$$k_t = \frac{c_k}{c_e} \Delta^2 E^2 \quad (3.25)$$

is obtained, where $E = \sqrt{2 \bar{\bar{e}} : \bar{\bar{e}}}$ is the characteristic filtered rate of strain.

Combining Eq. (3.25) and Eq. (3.22), the subgrid dynamic turbulent viscosity is denoted as

$$\mu_t = \rho c_k \sqrt{\frac{c_k}{c_e}} \Delta^2 E. \quad (3.26)$$

In previous studies [139], the subgrid turbulent viscosity is usually defined as $\mu_t = \rho c_s^2 \Delta^2 E$. Thus, it can be concluded that

$$c_s^2 = c_k \sqrt{\frac{c_k}{c_e}}. \quad (3.27)$$

The choice of the value of c_s is dependent on the simulation conditions such as the mesh size and stability of the boundary layer. The value of c_s cannot be too small, otherwise the simulation is affected by the oscillations in the small scale. On the contrary, if the value of c_s is too large, subgrid stress dominates the total stress. The flow field tends to be laminarized and the simulation is no longer a true LES. In the present study, for the simulation with the flat ground surface, the constant c_k is set to 0.05 and c_e to 1.048, these values correspond to the value of c_s as 0.1. In the simulation including a mountain located at the bottom surface, since the mesh size is much larger than the one used in the flat surface simulation (see section 5.2.2.1), the value of the constant c_k is reduced to 0.0005, which corresponds to the value of c_s as 0.0033.

The effective thermal diffusivity α_{eff} is calculated following $\rho\alpha_{\text{eff}} = \mu_l/\text{Pr}_l + \mu_t/\text{Pr}_t$, where the laminar and turbulent Prandtl numbers equal 0.7, i.e. $\rho\alpha_{\text{eff}} = \mu_{\text{eff}}/0.7$. The species diffusion coefficients, $D_{i,\text{eff}}$, are taken to be equal for each species, $D_{i,\text{eff}} = D_{\text{eff}}$, and a Lewis number, $\text{Le} = \alpha_{\text{eff}}/D_{\text{eff}}$, of unity is assumed.

3.2.2.2 Thermodynamic Properties

Temperature dependent physical properties of the chemical species including heat capacity, enthalpy, and entropy are given by using polynomials from the JANAF (Joint Army-Navy-Air Force) tables [140] as follows [141]:

$$\frac{C_p}{R} = a_1 + a_2T + a_3T^2 + a_4T^3 + a_5T^4, \quad (3.28)$$

$$\frac{H}{RT} = a_1 + \frac{a_2}{2}T + \frac{a_3}{3}T^2 + \frac{a_4}{4}T^3 + \frac{a_5}{5}T^4 + \frac{a_6}{T}, \quad (3.29)$$

$$\frac{S}{R} = a_1 \ln T + a_2T + \frac{a_3}{2}T^2 + \frac{a_4}{3}T^3 + \frac{a_5}{4}T^4 + a_7. \quad (3.30)$$

C_p is the specific heat capacity. R is the universal gas constant. T is the temperature. H is the enthalpy and S is the entropy. a_1, a_2, \dots, a_7 are the polynomial constants for the species studied.

For the species, which cannot be found in the JANAF table such as HOBr, an estimation method used by Lundström [142] is implemented. The specific heat capacity, C_p , is regarded to be independent of the temperature, which leads to

$$a_1 = \frac{C_p}{R}, \quad (3.31)$$

with

$$a_2 = a_3 = a_4 = a_5 = 0.0. \quad (3.32)$$

Then a_6 and a_7 can be computed as:

$$a_6 = \frac{H}{R} - a_1 T \quad (3.33)$$

and

$$a_7 = \frac{S}{R} - a_1 \ln T. \quad (3.34)$$

Taking the standard state thermodynamic properties C_p° , H° and S° from McBride and Gordon [143] and McGrath and Rowland [144], it is possible to calculate a_1 , a_6 and a_7 for Br, BrO, Br₂ and HOBr in the present study.

4. Numerical Scheme

In this chapter, the numerical scheme of the model and its implementation are described. The numerical solver for dealing with the governing equations ((Eq. (3.11) to Eq. (3.14) in Chapter 3) is developed by using the open source software OpenFOAM 1.7.1. OpenFOAM is a finite-volume toolbox which contains a cluster of C++ libraries. The value stored in OpenFOAM is categorized into two types, volume-centered and face-centered. Different interpolation techniques (e.g., upwind, TVD (Total Variation Diminishing) [145], ...) are implemented for the conversion between the values of these two categories. OpenFOAM contains a variety of solvers which can simulate complex physical phenomena such as combustion flames, shear flows and atmospheric flows.

Most of the solvers in OpenFOAM are structured based on Issa's PISO method (Pressure-Implicit with Splitting Operations) [146]. The PISO algorithm consists of one predictor step and several following corrector steps. It is efficient as it requires only few corrector steps to reach the accuracy needed. The numerical model used in this study is developed from the compressible solver reactingFoam. It originally aims at simulating the compressible flows including air convection and chemical reactions for combustion. In this study, the solver is extended to investigate the atmospheric boundary layer flow by adding Coriolis force, mean geophysical horizontal driving force and the wall model conditions. The code runs in a high performance cluster bwGRiD Cluster Baden-Württemberg [147].

4.1 Discretization of the Equations

For the discretization of the equations, the momentum equation (3.18) is taken as an example. If the first-order Euler implicit time difference scheme and linear interpolation of values from volume-centered type to face-centered type are used, the discretized form of Eq. (3.18) is as follows:

- X-direction:

$$\begin{aligned}
& \frac{(\rho_{ijk}^n(U_{ijk}^* - U_{ijk}^n))}{\Delta t} + \frac{(\rho U)_{i+\frac{1}{2},jk}^n(U_{ijk}^* + U_{i+1,jk}^*) - (\rho U)_{i-\frac{1}{2},jk}^n(U_{i-1,jk}^* + U_{ijk}^*)}{2\Delta x} \\
& + \frac{(\rho V)_{i,j+\frac{1}{2},k}^n(U_{ijk}^* + U_{i,j+1,k}^*) - (\rho V)_{i,j-\frac{1}{2},k}^n(U_{i,j-1,k}^* + U_{ijk}^*)}{2\Delta y} \\
& + \frac{(\rho W)_{ij,k+\frac{1}{2}}^n(U_{ijk}^* + U_{ij,k+1}^*) - (\rho W)_{ij,k-\frac{1}{2}}^n(U_{ij,k-1}^* + U_{ijk}^*)}{2\Delta z} \\
& = - \frac{\partial \bar{p}}{\partial x} \Big|_{ijk}^n - \left(\frac{\partial \tau_{xx}}{\partial x} + \frac{\partial \tau_{xy}}{\partial y} + \frac{\partial \tau_{xz}}{\partial z} \right) \Big|_{ijk}^n \\
& - \left(\frac{\partial \tau_{t,xx}^D}{\partial x} + \frac{\partial \tau_{t,xy}^D}{\partial y} + \frac{\partial \tau_{t,xz}^D}{\partial z} \right) \Big|_{ijk}^n - (2\rho (\Omega_y W - \Omega_z V))|_{ijk}^n,
\end{aligned} \tag{4.1}$$

- Y-direction:

$$\begin{aligned}
& \frac{(\rho_{ijk}^n(V_{ijk}^* - V_{ijk}^n))}{\Delta t} + \frac{(\rho U)_{i+\frac{1}{2},jk}^n(V_{ijk}^* + V_{i+1,jk}^*) - (\rho U)_{i-\frac{1}{2},jk}^n(V_{i-1,jk}^* + V_{ijk}^*)}{2\Delta x} \\
& + \frac{(\rho V)_{i,j+\frac{1}{2},k}^n(V_{ijk}^* + V_{i,j+1,k}^*) - (\rho V)_{i,j-\frac{1}{2},k}^n(V_{i,j-1,k}^* + V_{ijk}^*)}{2\Delta y} \\
& + \frac{(\rho W)_{ij,k+\frac{1}{2}}^n(V_{ijk}^* + V_{ij,k+1}^*) - (\rho W)_{ij,k-\frac{1}{2}}^n(V_{ij,k-1}^* + V_{ijk}^*)}{2\Delta z} \\
& = - \frac{\partial \bar{p}}{\partial y} \Big|_{ijk}^n - \left(\frac{\partial \tau_{yx}}{\partial x} + \frac{\partial \tau_{yy}}{\partial y} + \frac{\partial \tau_{yz}}{\partial z} \right) \Big|_{ijk}^n \\
& - \left(\frac{\partial \tau_{t,yx}^D}{\partial x} + \frac{\partial \tau_{t,yy}^D}{\partial y} + \frac{\partial \tau_{t,yz}^D}{\partial z} \right) \Big|_{ijk}^n - (2\rho (\Omega_z U - \Omega_x W))|_{ijk}^n,
\end{aligned} \tag{4.2}$$

- Z-direction:

$$\begin{aligned}
& \frac{(\rho_{ijk}^n(W_{ijk}^* - W_{ijk}^n))}{\Delta t} + \frac{(\rho U)_{i+\frac{1}{2},jk}^n(W_{ijk}^* + W_{i+1,jk}^*) - (\rho U)_{i-\frac{1}{2},jk}^n(W_{i-1,jk}^* + W_{ijk}^*)}{2\Delta x} \\
& + \frac{(\rho V)_{i,j+\frac{1}{2},k}^n(W_{ijk}^* + W_{i,j+1,k}^*) - (\rho V)_{i,j-\frac{1}{2},k}^n(W_{i,j-1,k}^* + W_{ijk}^*)}{2\Delta y} \\
& + \frac{(\rho W)_{ij,k+\frac{1}{2}}^n(W_{ijk}^* + W_{ij,k+1}^*) - (\rho W)_{ij,k-\frac{1}{2}}^n(W_{ij,k-1}^* + W_{ijk}^*)}{2\Delta z} \\
& = - \frac{\partial \bar{p}}{\partial z} \Big|_{ijk}^n - \left(\frac{\partial \tau_{zx}}{\partial x} + \frac{\partial \tau_{zy}}{\partial y} + \frac{\partial \tau_{zz}}{\partial z} \right) \Big|_{ijk}^n \\
& - \left(\frac{\partial \tau_{t,zx}^D}{\partial x} + \frac{\partial \tau_{t,zy}^D}{\partial y} + \frac{\partial \tau_{t,zz}^D}{\partial z} \right) \Big|_{ijk}^n - (2\rho (\Omega_x V - \Omega_y U))|_{ijk}^n - (\rho g)|_{ijk}^n.
\end{aligned} \tag{4.3}$$

In Eqs. (4.1)–(4.3), the superscript n denotes the value at the n^{th} time step and the superscript $*$ represents the predicted value. The subscript i, j, k mean the values at the i^{th} grid node along x -direction, j^{th} along y -direction and k^{th} along z -direction. U , V and W are the velocity components. ρ is the air density. Δt is the time step. Δx , Δy and Δz are the grid mesh size along x , y and z direction, respectively. For the discretization of the source terms in RHS of Eqs. (4.1)–(4.3), if a second order central difference discretization scheme is used, the source terms in RHS of Eq. (4.1) can be written as:

$$-\left.\frac{\partial \bar{p}}{\partial x}\right|_{ijk}^n = -\left(\frac{\bar{p}|_{i+1,jk}^n - \bar{p}|_{i-1,jk}^n}{2\Delta x}\right), \quad (4.4)$$

$$\begin{aligned} -\left.\left(\frac{\partial \tau_{xx}}{\partial x} + \frac{\partial \tau_{xy}}{\partial y} + \frac{\partial \tau_{xz}}{\partial z}\right)\right|_{ijk}^n &= -\left(\frac{\tau_{xx}|_{i+1,jk}^n - \tau_{xx}|_{i-1,jk}^n}{2\Delta x} + \frac{\tau_{xy}|_{i,j+1,k}^n - \tau_{xy}|_{i,j-1,k}^n}{2\Delta y}\right. \\ &\quad \left.+ \frac{\tau_{xz}|_{ij,k+1}^n - \tau_{xz}|_{ij,k-1}^n}{2\Delta z}\right), \end{aligned} \quad (4.5)$$

$$\begin{aligned} -\left.\left(\frac{\partial \tau_{t,xx}^D}{\partial x} + \frac{\partial \tau_{t,xy}^D}{\partial y} + \frac{\partial \tau_{t,xz}^D}{\partial z}\right)\right|_{ijk}^n &= -\left(\frac{\tau_{t,xx}^D|_{i+1,jk}^n - \tau_{t,xx}^D|_{i-1,jk}^n}{2\Delta x} + \frac{\tau_{t,xy}^D|_{i,j+1,k}^n - \tau_{t,xy}^D|_{i,j-1,k}^n}{2\Delta y}\right. \\ &\quad \left.+ \frac{\tau_{t,xz}^D|_{ij,k+1}^n - \tau_{t,xz}^D|_{ij,k-1}^n}{2\Delta z}\right). \end{aligned} \quad (4.6)$$

Similarly, the source terms of Eq. (4.2) and Eq. (4.3) can be calculated.

The discretized equations (4.1)–(4.3) can be re-organized as the form of

$$\begin{aligned} &\left(\frac{\rho_{ijk}^n}{\Delta t} + \frac{(\rho U)_{i+\frac{1}{2},jk}^n - (\rho U)_{i-\frac{1}{2},jk}^n}{2\Delta x} + \frac{(\rho V)_{i,j+\frac{1}{2},k}^n - (\rho V)_{i,j-\frac{1}{2},k}^n}{2\Delta y} + \frac{(\rho W)_{ij,k+\frac{1}{2}}^n - (\rho W)_{ij,k-\frac{1}{2}}^n}{2\Delta z}\right)U_{ijk}^* \\ &+ \frac{(\rho U)_{i+\frac{1}{2},jk}^n}{2\Delta x}U_{i+1,jk}^* - \frac{(\rho U)_{i-\frac{1}{2},jk}^n}{2\Delta x}U_{i-1,jk}^* + \frac{(\rho V)_{i,j+\frac{1}{2},k}^n}{2\Delta y}U_{i,j+1,k}^* \\ &- \frac{(\rho V)_{i,j-\frac{1}{2},k}^n}{2\Delta y}U_{i,j-1,k}^* + \frac{(\rho W)_{ij,k+\frac{1}{2}}^n}{2\Delta z}U_{ij,k+1}^* - \frac{(\rho W)_{ij,k-\frac{1}{2}}^n}{2\Delta z}U_{ij,k-1}^* \\ &= \frac{\rho_{ijk}^n}{\Delta t}U_{ijk}^n - \left.\frac{\partial \bar{p}}{\partial x}\right|_{ijk}^n - \left.\left(\frac{\partial \tau_{xx}}{\partial x} + \frac{\partial \tau_{xy}}{\partial y} + \frac{\partial \tau_{xz}}{\partial z}\right)\right|_{ijk}^n \\ &- \left.\left(\frac{\partial \tau_{t,xx}^D}{\partial x} + \frac{\partial \tau_{t,xy}^D}{\partial y} + \frac{\partial \tau_{t,xz}^D}{\partial z}\right)\right|_{ijk}^n - (2\rho(\Omega_y W - \Omega_z V))|_{ijk}^n, \end{aligned} \quad (4.7)$$

$$\begin{aligned}
& \left(\frac{\rho_{ijk}^n}{\Delta t} + \frac{(\rho U)_{i+\frac{1}{2},jk}^n - (\rho U)_{i-\frac{1}{2},jk}^n}{2\Delta x} + \frac{(\rho V)_{i,j+\frac{1}{2},k}^n - (\rho V)_{i,j-\frac{1}{2},k}^n}{2\Delta y} + \frac{(\rho W)_{ij,k+\frac{1}{2}}^n - (\rho W)_{ij,k-\frac{1}{2}}^n}{2\Delta z} \right) V_{ijk}^* \\
& + \frac{(\rho U)_{i+\frac{1}{2},jk}^n}{2\Delta x} V_{i+1,jk}^* - \frac{(\rho U)_{i-\frac{1}{2},jk}^n}{2\Delta x} V_{i-1,jk}^* + \frac{(\rho V)_{i,j+\frac{1}{2},k}^n}{2\Delta y} V_{i,j+1,k}^* \\
& - \frac{(\rho V)_{i,j-\frac{1}{2},k}^n}{2\Delta y} V_{i,j-1,k}^* + \frac{(\rho W)_{ij,k+\frac{1}{2}}^n}{2\Delta z} V_{ij,k+1}^* - \frac{(\rho W)_{ij,k-\frac{1}{2}}^n}{2\Delta z} V_{ij,k-1}^* \\
& = \frac{\rho_{ijk}^n}{\Delta t} V_{ijk}^n - \frac{\partial \bar{p}}{\partial y} \Big|_{ijk}^n - \left(\frac{\partial \tau_{yx}}{\partial x} + \frac{\partial \tau_{yy}}{\partial y} + \frac{\partial \tau_{yz}}{\partial z} \right) \Big|_{ijk}^n \\
& - \left(\frac{\partial \tau_{t,yx}^D}{\partial x} + \frac{\partial \tau_{t,yy}^D}{\partial y} + \frac{\partial \tau_{t,yz}^D}{\partial z} \right) \Big|_{ijk}^n - (2\rho (\Omega_z U - \Omega_x W)) \Big|_{ijk}^n,
\end{aligned} \tag{4.8}$$

$$\begin{aligned}
& \left(\frac{\rho_{ijk}^n}{\Delta t} + \frac{(\rho U)_{i+\frac{1}{2},jk}^n - (\rho U)_{i-\frac{1}{2},jk}^n}{2\Delta x} + \frac{(\rho V)_{i,j+\frac{1}{2},k}^n - (\rho V)_{i,j-\frac{1}{2},k}^n}{2\Delta y} + \frac{(\rho W)_{ij,k+\frac{1}{2}}^n - (\rho W)_{ij,k-\frac{1}{2}}^n}{2\Delta z} \right) W_{ijk}^* \\
& + \frac{(\rho U)_{i+\frac{1}{2},jk}^n}{2\Delta x} W_{i+1,jk}^* - \frac{(\rho U)_{i-\frac{1}{2},jk}^n}{2\Delta x} W_{i-1,jk}^* + \frac{(\rho V)_{i,j+\frac{1}{2},k}^n}{2\Delta y} W_{i,j+1,k}^* \\
& - \frac{(\rho V)_{i,j-\frac{1}{2},k}^n}{2\Delta y} W_{i,j-1,k}^* + \frac{(\rho W)_{ij,k+\frac{1}{2}}^n}{2\Delta z} W_{ij,k+1}^* - \frac{(\rho W)_{ij,k-\frac{1}{2}}^n}{2\Delta z} W_{ij,k-1}^* \\
& = \frac{\rho_{ijk}^n}{\Delta t} W_{ijk}^n - \frac{\partial \bar{p}}{\partial z} \Big|_{ijk}^n - \left(\frac{\partial \tau_{zx}}{\partial x} + \frac{\partial \tau_{zy}}{\partial y} + \frac{\partial \tau_{zz}}{\partial z} \right) \Big|_{ijk}^n \\
& - \left(\frac{\partial \tau_{t,zx}^D}{\partial x} + \frac{\partial \tau_{t,zy}^D}{\partial y} + \frac{\partial \tau_{t,zz}^D}{\partial z} \right) \Big|_{ijk}^n - (2\rho (\Omega_x V - \Omega_y U)) \Big|_{ijk}^n - (\rho g) \Big|_{ijk}^n.
\end{aligned} \tag{4.9}$$

4.2 Pressure-Implicit with Splitting Operations (PISO) Method

In order to solve the discretized Navier-Stokes equations, in previous studies, two major categories of algorithms have been developed [148]: coupled method and segregated method (see Fig. 4.1).

In the type of coupled method, all the unknown variables are solved coupled in each grid cell. This type of method is mostly used in the compressible flows with high Reynolds number such as the explosion and shock-wave capturing. The disadvantage of this method is its relative low efficiency and excessive memory-consuming. That is because in a computation domain with N grid cells, at least $4N$ equations need to

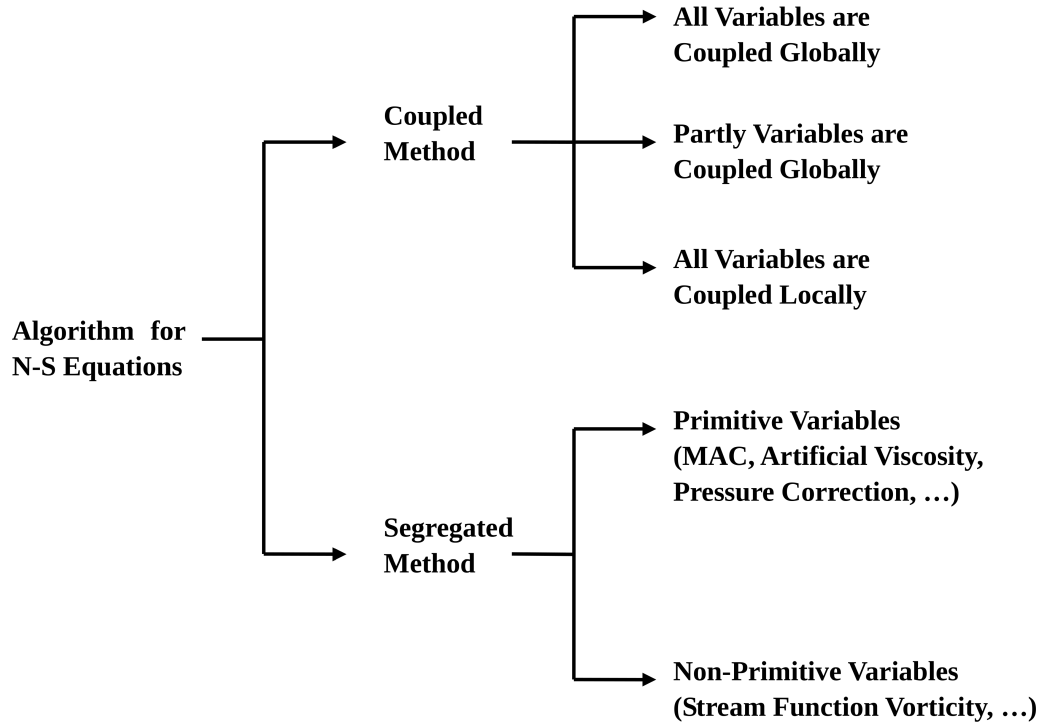


Figure 4.1: Categories of the numerical methods to solve the flow field.

be solved together (three momentum equations and one mass equation in each cell). Thus, the coupled method requires a long simulation time and large storage space.

The other type is called segregated method. Compared with the coupled method, instead of solving all the governing equations coupled, the equations are solved in order. The segregated methods include non-primitive variables method and primitive variables method. A typical non-primitive variables method is the Stream Function Vorticity method [149]. In the Stream Function Vorticity method, vorticity and flow function is solved instead of solving the original variables (velocity and pressure). In that case, problems caused by the unknown pressure field are avoided. However, this method is not suitable to be extended to a higher dimension. It is also difficult to define the boundary conditions for the vorticity in some special cases [149].

Another branch of segregated method is the primitive variables method. It contains several famous methods such as the MAC (Mark And Cell) method [150] and the artificial viscosity method [151]. In the MAC method, a set of the marker particles is distributed in the initial flow field, and these marker particles move with the fluid, identifying the location of the fluid and the free surface [150]. In the artificial viscosity method, an extra artificial viscosity is induced to increase the viscosity dissipation so that the shock zones with very stiff discontinuities can be investigated [151]. Within

these primitive variables methods, the most common type used in engineering field is the pressure correction method. The basic idea of pressure correction method is:

1. Prescribe an initial pressure field P_0 and velocity field U_0 , calculating the coefficients required in the equations
2. Solve the momentum equations and obtain the predict velocity field U^p
3. Apply the continuity equation to derive the pressure equation
4. Correct the pressure field P^* from the pressure equation using the predict velocity field U^p
5. Correct the velocity field U^* using the corrected pressure field P^*
6. Solve other scalar equations such as temperature and chemical species
7. Check whether the solution is converged or not. If not, return to step 2; If yes, step forward to the next time step

The pressure correction method contains a bunch of similar methods such as SIMPLE (Semi-Implicit Method for Pressure-Linked Equations) [152], SIMPLER (SIMPLE Revised) [153] and PISO method [146] which is adopted in this study. PISO was first proposed by Issa in 1986. Compared with other methods which have one corrector step, PISO method includes one predictor step and a cluster of following corrector steps. The flow chart of the PISO algorithm is shown in Fig. 4.2.

At the beginning of the simulation, the initial velocity U_0 and pressure P_0 fields are assumed so that all the coefficients and terms needed in the momentum equations can be calculated. Then the prescribed pressure field P_0 is used in the momentum equation to derive the predict velocities fields U^p . Since the continuity equation needs fulfilled, the pressure equation can be acquired based on the continuity equation. After solving the pressure equation using the value of U^p , the corrected pressure P^* and velocity U^* fields are obtained. Later, by using first corrected velocities U^* in the pressure equation, the pressure field can be corrected again P^{**} and thus the velocity field U^{**} . These second corrected fields are attributed to be exact. PISO method is useful in solving unsteady problem. Although it requires extra storage space for the data after the first corrector step, it is still quite effective and has been applied in many commercial softwares [154].

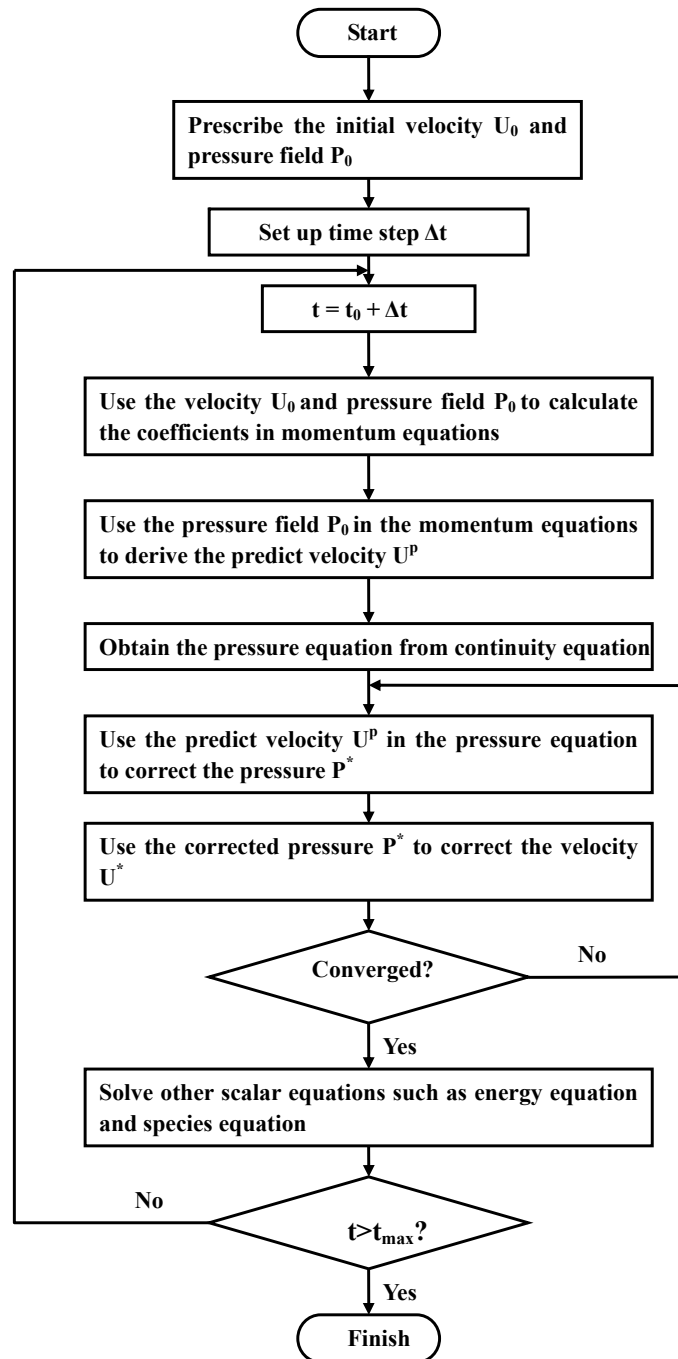


Figure 4.2: Flow chart for PISO algorithm (after Versteeg and Malalasekera [154]).

4.3 Implementation of the PISO Method in OpenFOAM

After the discretization of the equations, the form of the Eqs. (4.7)-(4.9) can be written as the following general form:

$$C \vec{U} = r - \nabla p + \rho \vec{g}. \quad (4.10)$$

In Eq. (4.10), C represents the coefficient matrix multiplying \vec{U} which is the required solution. r are the explicit source terms excluding the pressure gradient and gravity. p is the modified pressure field. $\rho \vec{g}$ denotes the gravity where ρ is the air density and \vec{g} denotes the gravitational acceleration. A different form of pressure field $p_{\text{rgh}} = p - \rho g z$ is used in OpenFOAM. In that case, the sum of the pressure gradient and gravitational acceleration is written as:

$$-\nabla p + \rho \vec{g} = -\nabla(p_{\text{rgh}} + \rho g z) + \rho \vec{g} = -\nabla p_{\text{rgh}} - \nabla \rho g z. \quad (4.11)$$

Thus, Eq. (4.10) becomes

$$C \vec{U} = r - \nabla p_{\text{rgh}} - \nabla \rho g z. \quad (4.12)$$

As described in section 4.2, using the assumed initial velocities \vec{U}_0 and pressure field P_0 , the coefficients needed in Eq. (4.12) such as C and the explicit source terms r can be calculated. Then the predicted velocity field U^p can be calculated by solving the momentum equation (4.12). In OpenFOAM platform, this operation is achieved by applying the following function:

```
fvVectorMatrix UEqn
(
    fvm::ddt(rho, U)
  + fvm::div(phi, U)
  + turbulence->divDevRhoReff(U)
  - rho*fCoriolis \ Coriolis acceleration
);

UEqn.relax();

if (momentumPredictor)
{
    solve(UEqn ==
          fvc::reconstruct
```



```

(
    (
        - ghf*fvc::snGrad(rho)
        - fvc::snGrad(p_rgh)
    )*mesh.magSf()
)
, mesh.solver(U.select(finalIter))
);
}

```

It should be noticed that the source term denoting the effect of the Coriolis force is added.

The coefficient matrix C in Eq. (4.12) can be split into two parts, diagonal part A and off-diagonal part H' :

$$C = A + H'. \quad (4.13)$$

Therefore, Eq. (4.12) can be written as:

$$A \vec{U} = -H' \vec{U} + r - \nabla p_{\text{rgh}} - \nabla \rho g z. \quad (4.14)$$

Introducing $H = -H' \vec{U} + r$, which leads Eq. (4.14) to

$$A \vec{U} = H - \nabla p_{\text{rgh}} - \nabla \rho g z. \quad (4.15)$$

Both sides of Eq. (4.15) are multiplied by the inverse matrix of A and the density ρ , the equation is written as

$$\rho \vec{U} = \rho A^{-1} (H - \nabla p_{\text{rgh}} - \nabla \rho g z). \quad (4.16)$$

By taking the divergence of both sides of Eq. (4.16), Eq. (4.17) is obtained:

$$\nabla \cdot (\rho \vec{U}) = \nabla \cdot (\rho A^{-1} (H - \nabla p_{\text{rgh}} - \nabla \rho g z)). \quad (4.17)$$

From the continuity equation (3.11), it is known that

$$\nabla \cdot (\rho \vec{U}) = -\frac{\partial \rho}{\partial t}. \quad (4.18)$$

Since the corrected velocity should fulfill the continuity equation, it is possible to replace $\rho \vec{U}$ in Eq. (4.17) with the RHS of Eq. (4.18), which leads to:

$$-\frac{\partial \rho}{\partial t} = \nabla \cdot (\rho A^{-1} (H - \nabla p_{\text{rgh}} - \nabla \rho g z)). \quad (4.19)$$

Eq. (4.19) can be reorganized as

$$\nabla \cdot (\rho A^{-1} \nabla p_{\text{rgh}}) = \frac{\partial \rho}{\partial t} + \nabla \cdot (\rho A^{-1} (H - \nabla \rho g z)). \quad (4.20)$$

Eq. (4.20) is the pressure equation required in the PISO algorithm, which has been discussed in section 4.2.

The first corrected pressure P^* can be calculated by solving Eq. (4.20) using the value of predicted velocity field U^P . This calculation is performed in the following code:

```

volScalarField rUA = 1.0/UEqn.A(); //1/A

surfaceScalarField rhorUAF(" (rho*(1/A(U))) ", fvc::
    interpolate(rho*rUA)); //rho*(1/A)

U = rUA*UEqn.H(); //(H/A)

phi = fvc::interpolate(rho)*
(
    (fvc::interpolate(U) & mesh.Sf())
    + fvc::ddtPhiCorr(rUA, rho, U, phi)
); //rho*(H/A)

surfaceScalarField buoyancyPhi = -rhorUAF*ghf*fvc::snGrad(
    rho)*mesh.magSf(); //-rho*(1/A)*(nabla rho) g z

phi += buoyancyPhi; //rho*(H/A)-rho*(1/A)*(nabla rho) g z

fvScalarMatrix p_rghEqn
(
    fvc::ddt(rho) + psi*correction(fvm::ddt(p_rgh))
    + fvc::div(phi)
    - fvm::laplacian(rhorUAF, p_rgh)
);

p_rghEqn.solve
(
    mesh.solver
    (
        p_rgh.select
        (
            finalIter
            && corr == nCorr-1

```

```

        && nonOrth == nNonOrthCorr
    )
)
);

```

Afterwards, the velocity is corrected to \vec{U}^* by applying P^* in Eq. (4.16).

```

phi += p_rghEqn.flux(); // Explicitly relax
    pressure for momentum corrector
p_rgh.relax();

U += rUA*fvc::reconstruct((buoyancyPhi + p_rghEqn.
    flux())/rhorUAf);
U.correctBoundaryConditions();

```

After having obtained the first corrected pressure P^* and velocity \vec{U}^* , the values of P^* and \vec{U}^* can be used as the predicted value for the next corrector step to obtain the second corrected pressure P^{**} and velocity \vec{U}^{**} until the solution is converged to the accuracy needed. Then the simulation go forward to the next time step. These following corrector steps are performed in OpenFOAM by repeatedly solving the pressure function using the latest updated value from the last corrector step.

5. Results and Discussion

In this chapter, the results are presented and discussed. Some of the results have been published by Cao et al. [122] and Cao and Gutheil [155].

5.1 Box Model

For the box model, the primary focus is on capturing the temporal variations of the chemical species mixing ratios and analyzing the detailed chemical reaction mechanisms. The mechanism without any NO_x and chlorine related reactions is analyzed first. It involves 55 reactions (from reaction (R1) to (R55) in Appendix B) and 30 chemical species. This chemical reaction mechanism is referred as 'bromine only mechanism' in the following context. Then, 31 reactions (reactions (R56) through (R86)) and 9 nitrogen containing species are added in order to investigate the effect of NO_x species. Similar constant values of the uptake coefficient ($\gamma = 0.06$) are taken for these NO_x related heterogeneous reactions (R83), (R85) and (R86). Since NO_x is converted to PAN (peroxyacetyl nitrate), which can be hardly photolyzed, fluxes of nitrogen containing species produced from the snow are added to the model (see Tab. 5.1). The emission rates of NO, NO_2 , H_2O_2 and HCHO are estimated based on the measurements [156, 157, 158], and the production ratio of HONO and NO_2 is 1.0 [159]. The photolysis of nitrate in the snow pack can be the major source of the nitrogen containing fluxes. Finally, 49 chlorine related reactions (reactions (R87) through (R135))

Table 5.1: Emission fluxes from the snow [122].

Species	Emission rates [molec. $\text{cm}^{-2}\text{s}^{-1}$]
NO	1.6×10^7
NO_2	1.6×10^7
HONO	1.6×10^7
H_2O_2	1.6×10^8
HCHO	6.0×10^7

Table 5.2: Initial gas composition [122], ppm = parts per million, ppb = parts per billion, ppt = parts per trillion.

Species	Mixing ratio	Species	Mixing ratio
O ₃	40 ppb	C ₂ H ₆	2.5 ppb
H ₂ O	800 ppm	C ₂ H ₄	100 ppt
Br ₂	0.3 ppt	C ₂ H ₂	600 ppt
HBr	0.01 ppt	C ₃ H ₈	1.2 ppb
CH ₄	1.9 ppm	NO	5 ppt
CO ₂	371 ppm	NO ₂	10 ppt
CO	132 ppb	Cl ₂	0.3 ppt
HCHO	100 ppt	HCl	0.01 ppt
CH ₃ CHO	100 ppt		

and 10 chlorine containing species are included. When the latter mechanism is used, the time integral concentrations of the bromine and chlorine atoms during the ozone depletion are determined.

The initial gas phase species mixing ratios are listed in Tab. 5.2. The prescribed initial trigger of bromine species in air is 0.3 ppt Br₂ and 0.01 ppt HBr. This small amount of active bromine may come from the degradation of natural organohalogen compounds, for instance CHBr₃) [85]. All other species not listed have initial concentration of zero (except for air).

5.1.1 Bromine Only Chemical Reaction Mechanism

Figure 5.1 displays the modeled mixing ratios of the relevant species as a function of time for the boundary layer heights of 200 m, and Fig. 5.1(b) is a column presentation of Fig. 5.1(a). It can be seen that ozone depletion starts after five days and lasts for about 40 h for a 200 m boundary layer thickness. Before day five, little ozone is consumed. At this early stage, HOBr and BrO mixing ratios show exponential growth, and these two species constitute the majority contributions of bromine species. Due to the existence of ozone, the Br atoms are instantly converted to BrO, and thus, they can hardly be observed at this time. As the mixing ratio of HOBr is increasing, a large amount of reactive bromine is released from the saline surface, leading to an explosive increase of the total bromine loading and a rapid decrease of ozone. After six days, BrO builds up to reach a peak level of 60 ppt, and then it rapidly decreases. When the HOBr mixing ratio increases to its maximum value of about 65 ppt, the ozone mole fraction falls down below 1 ppb. Thereafter, the mixing ratio of HOBr falls rapidly, the

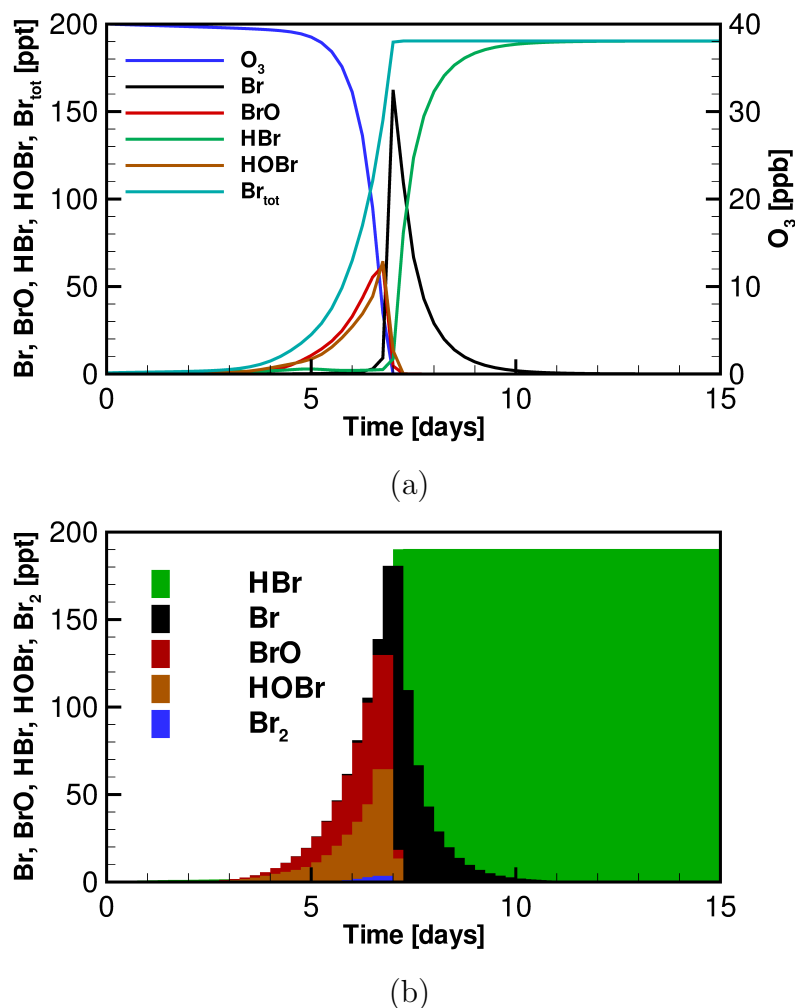


Figure 5.1: Time variation of ozone and bromine species for bromine only mechanism with the boundary layer height of 200 m [122].

mixing ratio of Br atom abruptly builds up to be the main constituent of the bromine stock, which increases to its maximum value of about 160 ppt. This large amount of Br is then removed by the aldehydes (for instance HCHO and CH_3CHO) in the natural air, forming HBr. At the end of the depletion event, a high level of HBr is left in the air, which is confirmed by the aerosol measurements of Langendörfer et al. [160].

Considering the temporal behavior of the species as discussed above, the whole ozone depletion process may be divided into three time periods. At the beginning of the event, the gaseous halogen mixing ratios in the air are low, only a small fraction of ozone is slowly consumed, this period may be called “induction stage”, in which the ozone depletion rate is less than 0.1 ppb h^{-1} . This period is followed by the “depletion stage”, where a large amount of inert halogens are released by the frequent collisions between the saline surface and HOBr molecules in the air. The ozone in the atmospheric

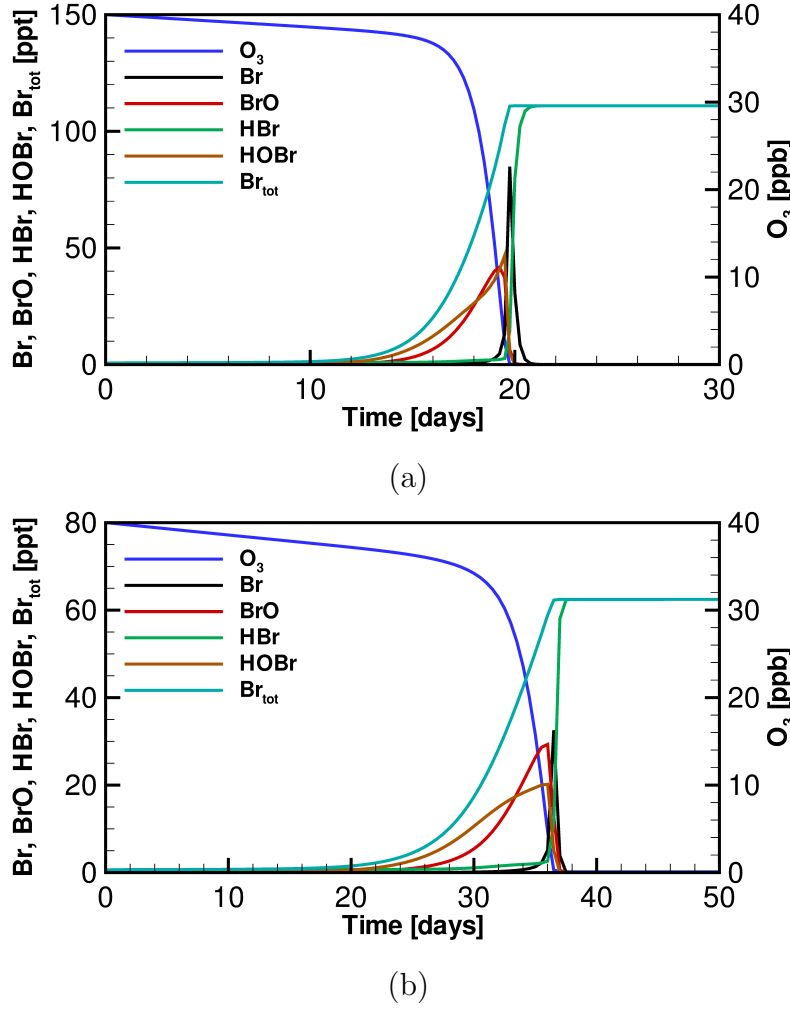


Figure 5.2: Time variation of ozone and bromine species for bromine only mechanism with the boundary layer height of (a) 500 m; (b) 1000 m [122].

boundary layer is severely consumed at this stage and the depletion rate is higher than 0.1 ppb h^{-1} . In the last time period, the “end stage”, ozone mixing ratio drops down below 10% of its original value (4 ppb in this study). The remaining halogen species are hydrogen halides, and the total halogen mixing ratio remains almost constant. For a 200 m boundary layer height and 0.3 ppt initial Br₂, the “induction stage” and “depletion stage” last for 5.1 days and 1.8 days, respectively.

When the boundary layer height (L_{mix}) is raised to 500 m and 1000 m (see Fig. 5.2), the depletion stage commences after 15 days and even more than 30 days, respectively, and the duration of the depletion stage is extended to about 3-5 days. The profiles of the bromine species mixing ratios and their changes during the ozone depletion event are similar to those simulated at $L_{\text{mix}} = 200 \text{ m}$ (Fig. 5.2a), but the peak values are considerably lower. The maximum values of BrO are in the range of 30–40 ppt, as

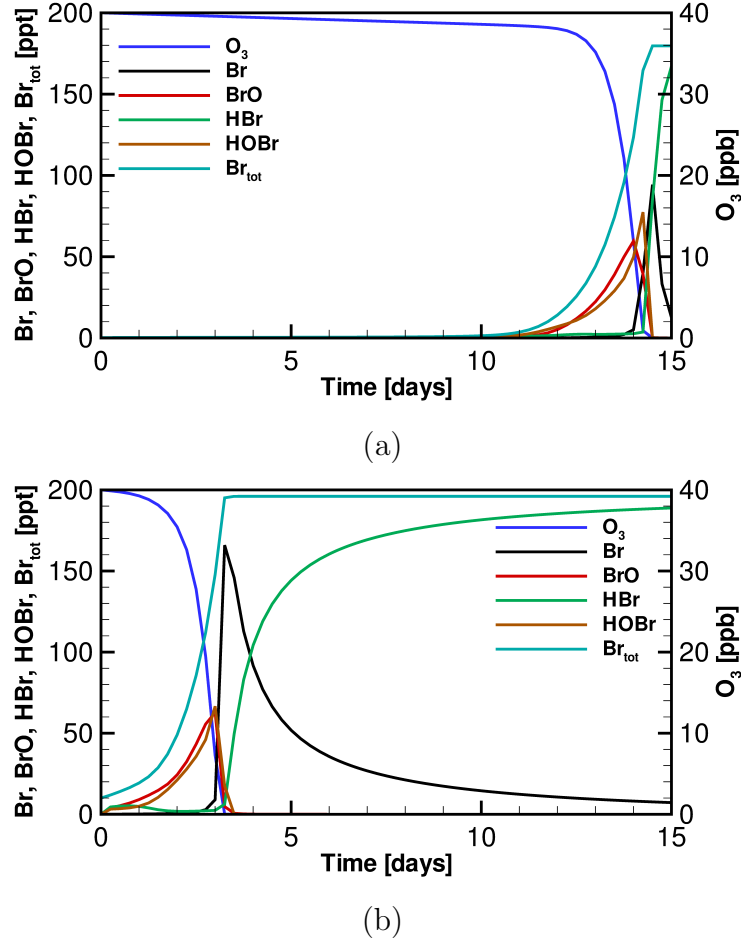


Figure 5.3: Time variation of ozone and bromine species for bromine only mechanism, when the initial Br_2 mixing ratio is (a) 0.1 ppt; (b) 0.5 ppt.

compared to 60 ppt at $L_{\text{mix}} = 200$ m. The results for 1000 m boundary layer height can be compared with the measurements and simulations conducted by Liao et al. [51], who found the mixing ratio of BrO between 20-30 ppt and HOBr around 20 ppt.

Different values of the initial Br_2 mixing ratio have been tested. From Fig. 5.3, it is seen that for a reduced value of 0.1 ppt initial Br_2 mixing ratio, the “induction stage” is prolonged, and for a higher initial value of 0.5 ppt, it is reduced, whereas the duration of the “depletion stage” is hardly affected. Thus, it can be concluded that the ozone depletion is caused by the activated bromine from the sea ice surface, whereas the initial bromine serves as a trigger to the ozone depletion event.

Exploratory simulations turning off the activation processes on aerosol or at the ice/snow surface were conducted. The results of the simulations are presented in Fig. 5.4 for three different values of boundary layer height. It is seen that both the activation processes at the ice/snow surface and the aerosol play a significant role, since

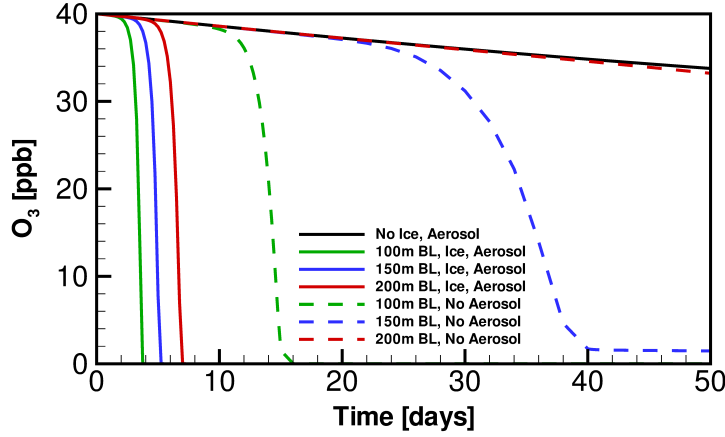
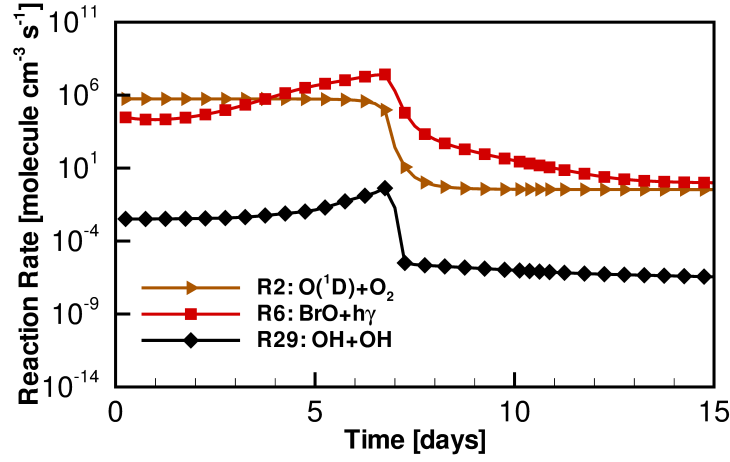


Figure 5.4: Effect of heterogeneous reaction rate on the ozone depletion time [122].

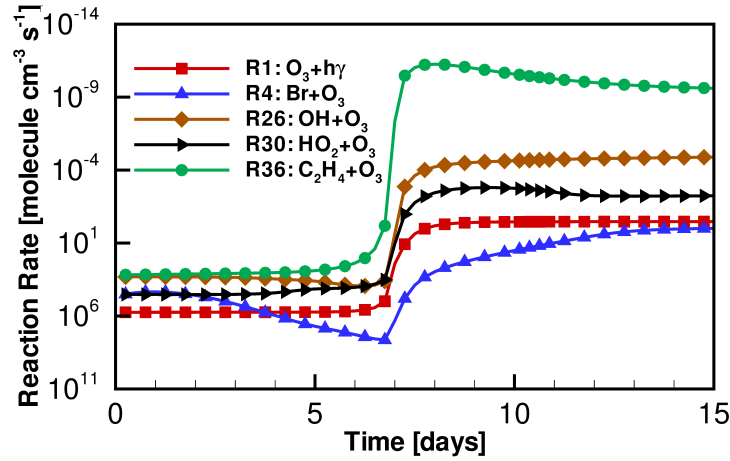
both of them lead to a strong enhancement of the ozone depletion. The existence of ice/snow surface is the major factor causing the ozone depletion, whereas the aerosol activation leads to an acceleration of the ozone depletion. This is because that the total halogen loading in the atmosphere is determined by the activation at the ice/snow surface, and the heterogeneous process on the aerosol surface helps to re-activate the halogen stored in hydrogen halides. It is also found that for a 200 m or higher boundary layer, the ozone depletion event will not happen if either aerosol or ice/snow surface activation is turned off. Thus, both activation processes are needed for a boundary layer higher than 200 m. Since the height of the stable boundary layers measured in polar regions mostly vary from 100 m to 500 m [97], the remainder of the study concerns a boundary layer height of 200 m.

Table 5.3: List of ozone relevant reactions (Type F: Ozone formation reaction; Type D: Ozone depletion reaction) [122].

Reaction	No.	Type
$\text{O}_3 + h\nu \rightarrow \text{O}(^1\text{D}) + \text{O}_2$	(R1)	D
$\text{O}(^1\text{D}) + \text{O}_2 \rightarrow \text{O}_3$	(R2)	F
$\text{Br} + \text{O}_3 \rightarrow \text{BrO} + \text{O}_2$	(R4)	D
$\text{BrO} + h\nu \xrightarrow{\text{O}_2} \text{Br} + \text{O}_3$	(R6)	F
$\text{OH} + \text{O}_3 \rightarrow \text{HO}_2 + \text{O}_2$	(R26)	D
$\text{OH} + \text{OH} \xrightarrow{\text{O}_2} \text{H}_2\text{O} + \text{O}_3$	(R29)	F
$\text{HO}_2 + \text{O}_3 \rightarrow \text{OH} + 2\text{O}_2$	(R30)	D
$\text{C}_2\text{H}_4 + \text{O}_3 \rightarrow \text{HCHO} + \text{CO} + \text{H}_2\text{O}$	(R36)	D



(a)



(b)

Figure 5.5: Temporal behavior of ozone relevant reaction rates in a 200 meters boundary layer: (a) formation (b) depletion [122]. Note that a reverse direction of vertical axis is used in the bottom panel.

The reactions directly affecting ozone mixing ratio are listed in Table 5.3, note that the complete mechanism is provided in the Supplement. Reactions (R2), (R6) and (R29) cause ozone formation, whereas reactions (R1), (R4), (R26), (R30), and (R36) lead to ozone depletion. The temporal evolution of these ozone relevant reaction rates are plotted in Fig. 5.5 in logarithmic scale for the case of 200 m boundary layer height. The relevance of these reactions is discussed below in connection with the sensitivity analysis, which reveals that the reactions discussed here have a high relative sensitivity and therefore, they dominate the entire process under consideration. In the

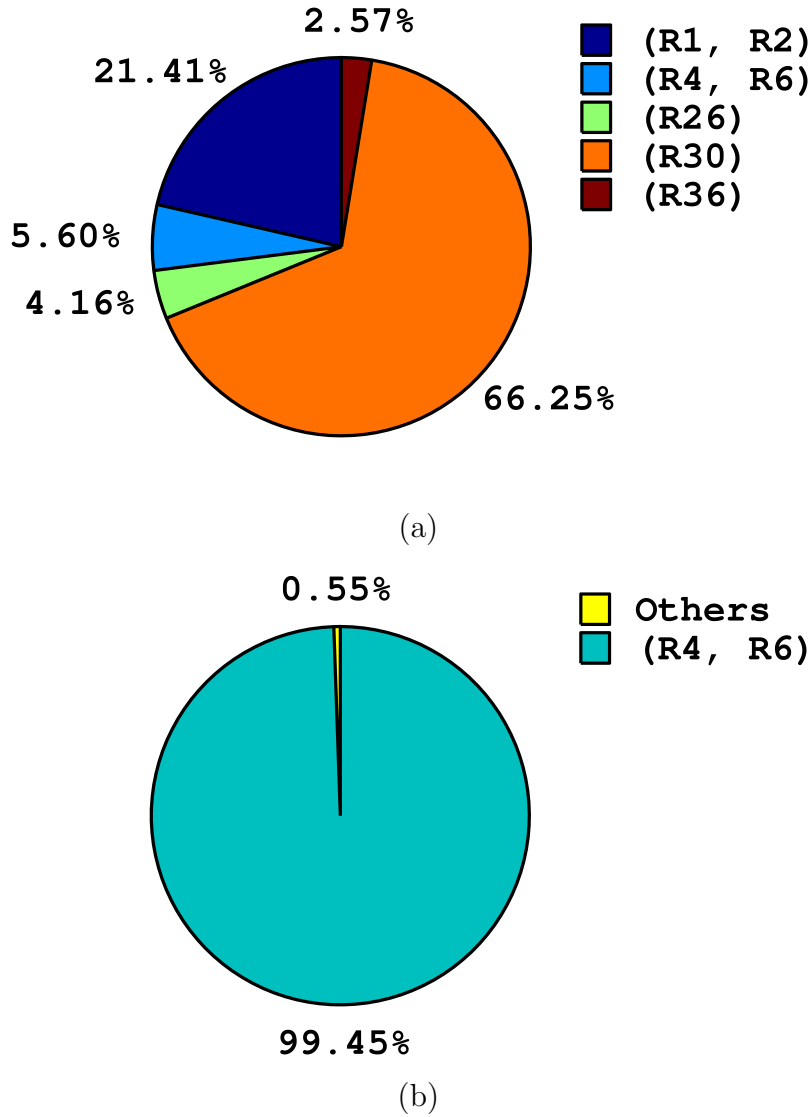


Figure 5.6: Contribution to ozone depletion at: (a) day 2 (induction stage) (b) day 6 (depletion stage) [122].

top part of the figure, ozone forming reactions are displayed, and in the bottom part, the rates for ozone depletion reactions are depicted in reverse vertical axial direction. It can be seen that during the ozone induction stage (before day 5), the fastest ozone enhancement reaction is (R2) while the fastest depletion reaction is (R1). Most of the ozone molecules are involved in this reaction pair during the induction stage. When the ozone depletion starts (after day 5), the most rapid ozone reaction pair consists of formation reaction (R6) and depletion reaction (R4). This reaction pair is about two orders of magnitude faster than the reaction pair (R1) and (R2) in the depletion stage.

Although most of the ozone molecules are involved in these fastest reaction pairs as

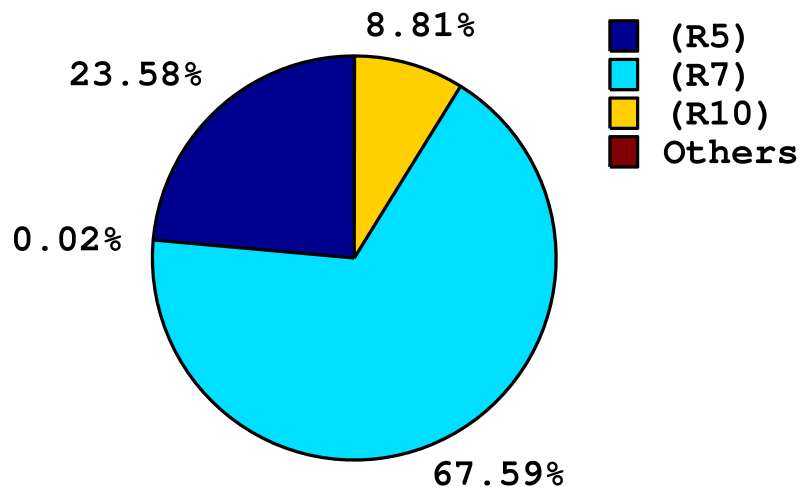


Figure 5.7: Contribution to Br formation at day 6 (depletion stage) [122].

mentioned above, it is actually the rate difference of these reaction pairs causing the ozone depletion. Therefore, the contributions to the total ozone destruction by various reactions and reaction pairs at different time steps are investigated. Figure 5.6 shows the instantaneous contributions to ozone depletion at day 2 (induction stage) and day 6 (depletion stage). In the induction stage, although most of the ozone molecules are involved in the reaction pair of (R1) and (R2) as discussed above, it is seen from Fig. 5.6a that the largest ozone consumption attributes to



On the contrary, during the depletion stage (cf. Fig. 5.6b), most of the ozone molecules are consumed by the rate difference between



and



This rate difference between (R4) and (R6) is due to the higher Br mixing ratio during the ozone depletion stage. The increase of the Br mixing ratio is mainly attributed by the self-reaction



which is confirmed by the result displayed in Fig. 5.7 showing the fractions of Br production at day 6.

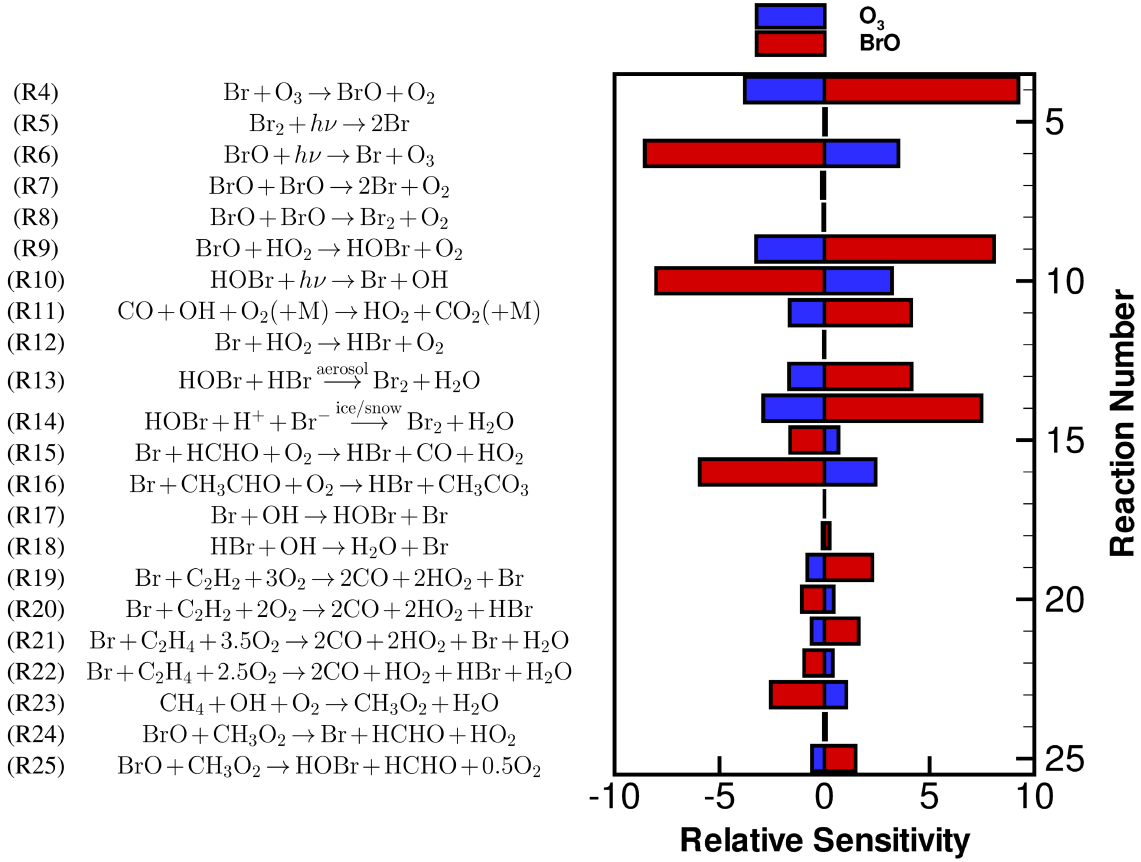


Figure 5.8: Relative sensitivities of ozone and BrO concentrations for bromine containing reactions at day 6 for a 200 m boundary layer height [122].

In the present study, the relevance of different chemical reaction steps is discussed in the framework of a sensitivity analysis (see Eq. (3.10)), which will be used to reduce the present mechanism to a skeletal reaction scheme for application in 3-D simulations. Figure 5.8 shows the relative sensitivities for ozone and BrO concentrations at day 6, which is the time, when major ozone depletion occurs. Red and blue bars show the sensitivity coefficients for BrO and for O₃, respectively, where it can be seen that they have opposite signs, which means that ozone is destroyed/formed as BrO is built up/consumed, a negative sign corresponds to depletion. Reactions (R4) and (R6), which constitute the fastest ozone pair as mentioned above, have a high impact on the ozone and BrO concentrations. HOBr production and destruction reactions, (R9) and (R10), are important since HOBr is involved in the heterogeneous bromine liberation process. The heterogeneous reactions, (R13) and (R14), are also crucial for the same reason. This means that it is very important to have a good knowledge of the chemical reaction rates of these reaction steps because of their dominance of the ozone depletion

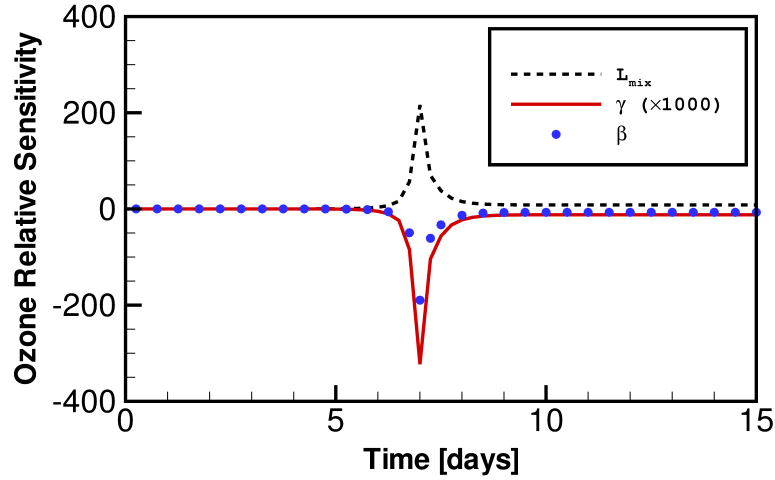


Figure 5.9: Temporal evolution of ozone concentration sensitivities for mixing length L_{mix} , uptake coefficient γ and surface coverage ratio β [122].

mechanism.

The temporal sensitivity evolution of ozone concentration for boundary layer height L_{mix} , saline surface uptake coefficient γ and reactive surface ratio β is displayed in Fig. 5.9. When the depletion process starts after 5 days, the absolute values of these sensitivities increase sharply and reach their peaks at around day 7 (cf. Fig. 5.9). The sensitivity of γ is smaller compared to the other two parameters because at the ice/snow surface, collision kinetics is less dominant compared to the transport of the air. Since all the physical properties considered here affect the ozone depletion through the heterogeneous reactions, it is demonstrated that the heterogeneous liberation process is very important throughout the ozone depletion state. Therefore, the effect of these parameters are studied in more detail.

The relative sensitivity of L_{mix} is positive, which means that for increased boundary layer height, the ozone depletion occurs later and less abrupt. This is consistent with the results shown in Fig. 5.2. Similarly, the negative sensitivities of γ and β cause a decrease of the ozone concentration with increased γ and β , which means that the ozone depletion is enhanced for higher values. This can be explained as follows: if the reaction probability between HOBr and the reactive surface is larger (i.e. a more reactive surface area is offered for the heterogeneous reactions), more bromine atoms are released, leading to the acceleration of the ozone depletion.

The reactive surface area ratio, β , is influenced by the physical structure and the roughness of the fresh ice surface covered by snow, which affects the heterogeneous reaction (R14). Figure 5.10a shows the variation of the ozone depletion time with the reactive surface ratio β . The vertical axis represents the total time needed until ozone

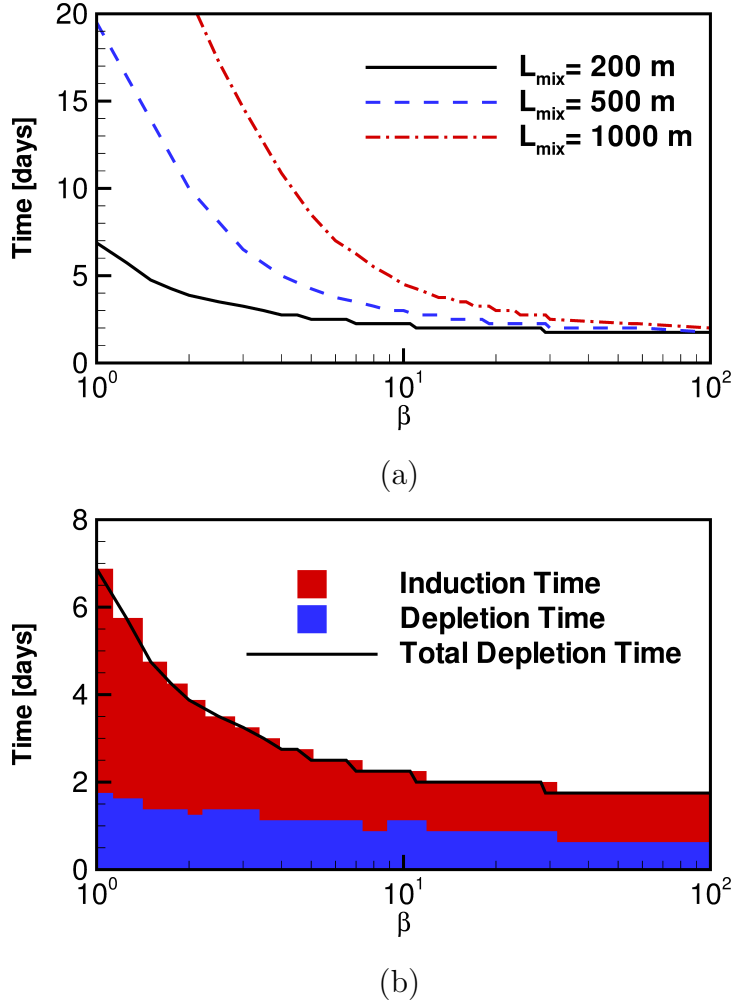


Figure 5.10: Impact of the reactive surface ratio on the (a) total ozone depletion time for three different boundary layer heights (b) induction and depletion time for a 200 m boundary layer height [122].

mixing ratio is less than 4 ppb (10 % of the initial mixing ratio), and the horizontal axis shows the value of β in log scale. Obviously, in different boundary layer conditions, when $\beta < 10$, the increase of β significantly reduces the total time including induction and depletion. All the depletion events with different boundary layer heights are completed within ten days if $\beta > 5$. When β approaches 100, all curves approximate the minimum limit of two days. This means that the maximum ozone depletion event rate caused by local chemistry is two days at 200 m boundary layer height. In Fig. 5.10b, it can be seen that the shortening of the ozone depletion time is mainly contributed by the time decrease of the “induction stage”. The time length of the “depletion stage” remains stable. When β approaches the value of 100, the simulated shortest ozone depletion event includes 28 h induction stage and 20 h depletion stage. From some

observations [45, 34, 161], extremely rapid ozone decrease with a drop of 30 ppb within several hours is found. However, it is usually assumed that most of this rapid decrease is caused by the transport of ozone-lacking air parcels to the measuring location [79]. To solve this question of chemistry versus transport, the consideration of the horizontal transport process is needed, which is beyond the box model study.

The following sections concern the extension of the present bromine mechanism through considering the chemical reactions including NO_x and chlorine.

5.1.2 NO_x Related Chemical Reaction Mechanism

The role of NO_x chemistry may be investigated by adding reactions (R56) to (R86) to the present chemical reaction system (see Appendix B). The NO_x mechanism adds

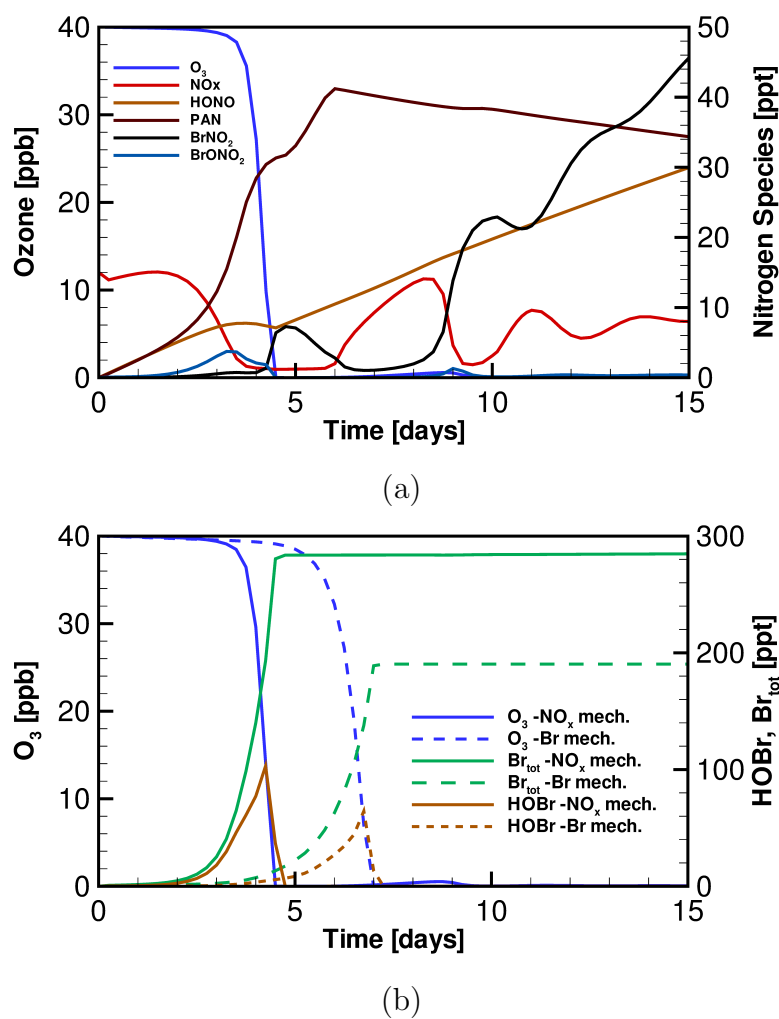


Figure 5.11: Time variation of ozone, nitrogen containing species and bromine concentrations for a boundary layer height of 200 m [122].

Table 5.4: List of NO_x relevant reactions [122] (Type F: NO_x formation reaction; Type D: NO_x depletion reaction).

Reaction	No.	Type
$\text{HO}_2 + \text{NO}_2(+\text{M}) \rightarrow \text{HNO}_4(+\text{M})$	(R62)	D
$\text{HNO}_4(+\text{M}) \rightarrow \text{HO}_2 + \text{NO}_2(+\text{M})$	(R63)	F
$\text{Br} + \text{NO}_2(+\text{M}) \rightarrow \text{BrNO}_2(+\text{M})$	(R77)	D
$\text{BrO} + \text{NO}_2(+\text{M}) \rightarrow \text{BrONO}_2(+\text{M})$	(R79)	D
$\text{BrONO}_2 + h\nu \rightarrow \text{BrO} + \text{NO}_2$	(R81)	F
$\text{BrNO}_2 + h\nu \rightarrow \text{Br} + \text{NO}_2$	(R82)	F
$\text{HNO}_3 + h\nu \xrightarrow{\text{aerosol}} \text{NO}_2 + \text{OH}$	(R85)	F

9 chemical species and 31 chemical reactions to the bromine mechanism. In Fig. 5.11, ozone, bromine and NO_x concentration profiles are plotted for $L_{\text{mix}} = 200$ m. During the ozone destruction period between days 3 and 4.5, the initial 15 ppt NO_x and fluxes of nitrogen containing species from the snow (see Tab. 5.1) are converted into BrONO₂ and other nitrogen containing species such as BrNO₂. The major sink of the nitrogen is PAN. Moreover, because an additional HOBr flux is generated by the BrONO₂ hydrolysis process (R83) and (R86) at the aerosol surfaces and the ice/snow pack, the peak value of HOBr activated from sea salts reaches more than 110 ppt compared to 65 ppt released by the chemical reaction mechanism without NO_x reactions, see Fig. 5.11b. It is illustrated that the total bromine concentration increases from about 190 ppt to approximately 280 ppt. This large value approaches the extreme bromine observation value of about 260 ppt reported by Impey et al. [88]. Figure 5.11 shows that the ozone depletion process starts after 3 days and ends before day 4.5. Thus, the

Table 5.5: Overview of NO_x relevant reactions [122].

Reaction	No.	Period
$\text{HO}_2 + \text{NO}_2(+\text{M}) \rightarrow \text{HNO}_4(+\text{M})$ $\text{HNO}_4(+\text{M}) \rightarrow \text{HO}_2 + \text{NO}_2(+\text{M})$	(R62) (R63)	Induction
$\text{BrO} + \text{NO}_2(+\text{M}) \rightarrow \text{BrONO}_2(+\text{M})$ $\text{BrONO}_2 + h\nu \rightarrow \text{BrO} + \text{NO}_2$ $\text{BrONO}_2 \xrightarrow{\text{H}_2\text{O}} \text{HOBr} + \text{HNO}_3$ $\text{HNO}_3 \xrightarrow{\text{aerosol}} \text{NO}_2 + \text{OH}$	(R79) (R81) (R83, R86) (R85)	Depletion
$\text{Br} + \text{NO}_2(+\text{M}) \rightarrow \text{BrNO}_2(+\text{M})$ $\text{BrNO}_2 + h\nu \rightarrow \text{Br} + \text{NO}_2$	(R77) (R82)	After Depletion

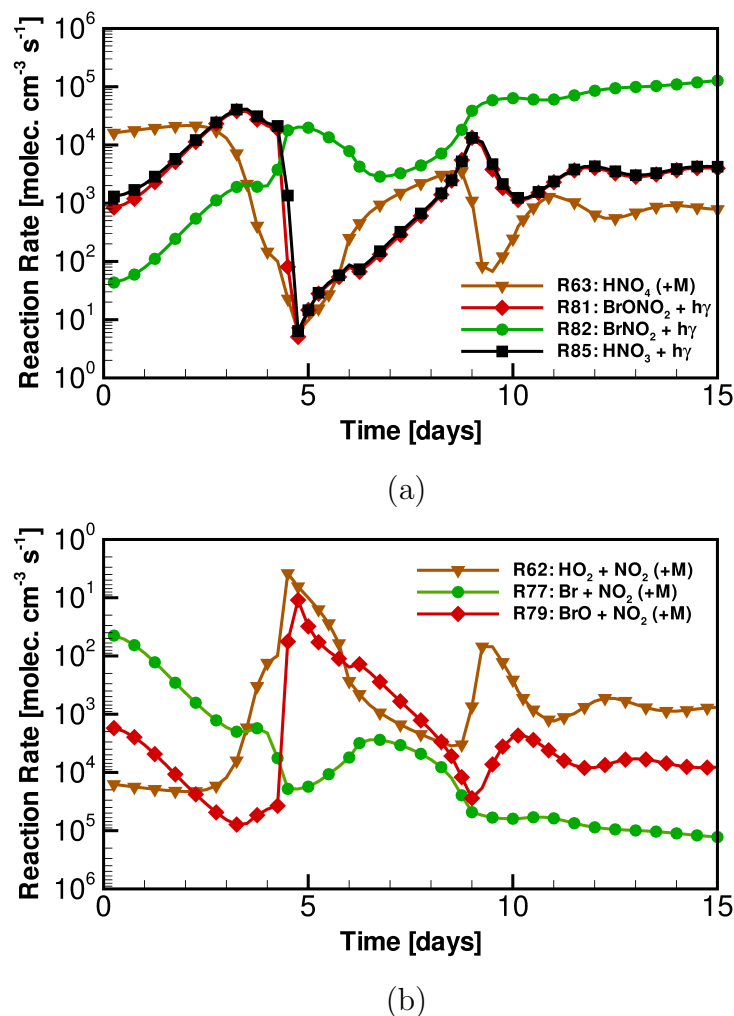


Figure 5.12: Temporal change of NO_x relevant reaction rates in 200 m boundary layer height: (a) formation (b) depletion [122].

induction period is shorter by about two days whereas the depletion stage is about the same compared with the results using the bromine only mechanism.

The reactions strongly and directly affecting NO_x mixing ratios are listed in Tab. 5.4, and their reaction rate evolutions are shown in Fig. 5.12. It is seen that NO_x mixing ratios are largely influenced by different reactions in different time stages. Table 5.5 gives a summary of the major chemical reactions affecting NO_x mixing ratios. In the early induction stage before day 3, the formation reaction (R63) and the depletion reaction (R62) are the most rapid NO_x related reactions. Most of the NO_x molecules participate in this reaction pair. However, in the induction stage, most of the NO_x molecules are converted to BrONO₂, leading to the enhancement of the BrONO₂ mixing ratio in the air. After the ozone depletion has started, the reactions (R79), (R81)

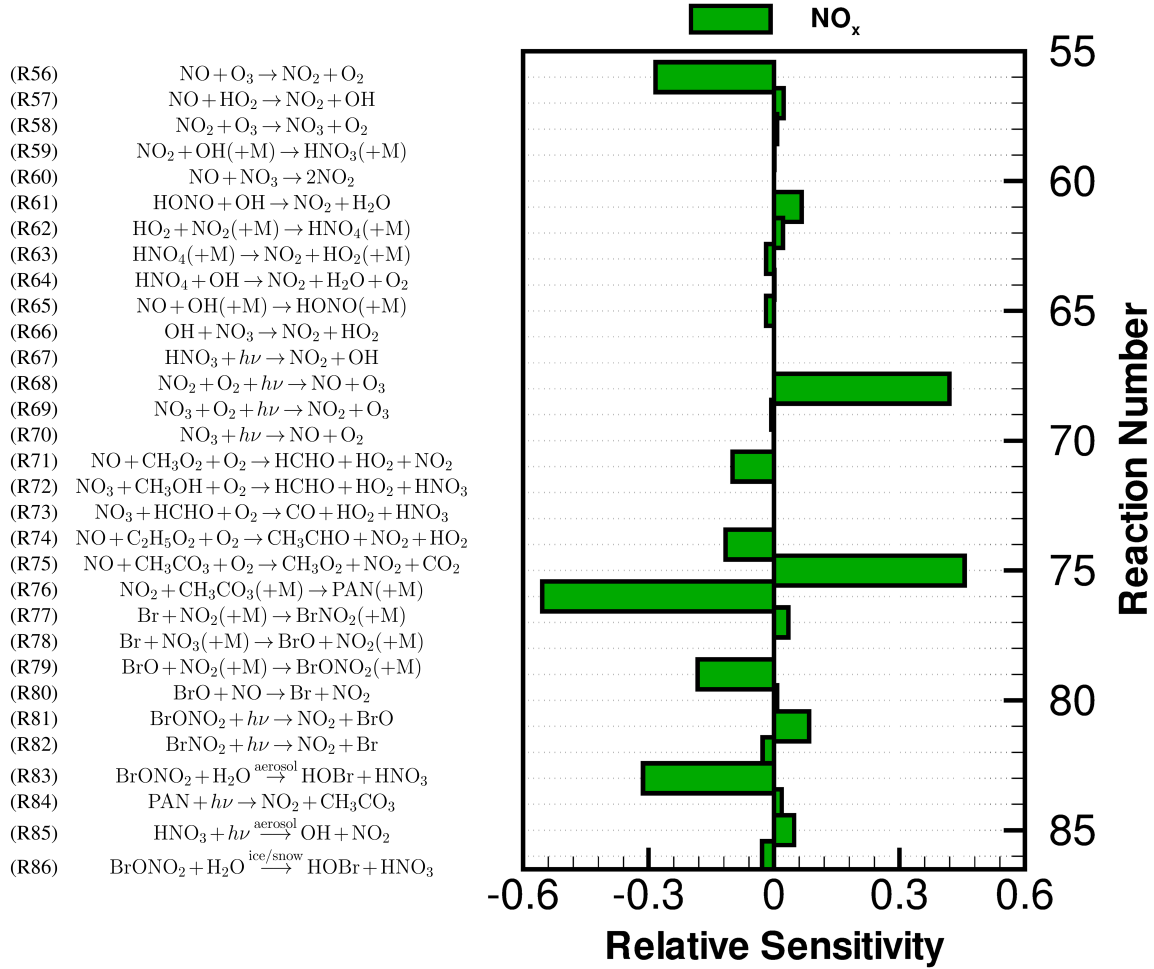


Figure 5.13: Relative sensitivities of NO_x concentrations at day 4 for a boundary layer height of 200 m [122].

and (R85) related to BrONO_2 become more important. The hydrolysis reactions (R83) and (R86) of BrONO_2 constitute the most efficient NO_x cycle during ozone depletion. Since most of the NO_x molecules are involved in this BrONO_2 related cycle at this time, the reaction rates of (R62) and (R63) shortly drop. As depletion ends after 4.4 days, the NO_x related reaction pair (R77) and (R82) becomes prominent. The rate difference between (R77) and (R82) causes the formation of BrNO_2 at the end of the depletion event, which is also observed in Fig. 5.11a.

The relative sensitivities of NO_x concentrations at day 4, which is within the ozone depletion stage (between day 3 and 4.5) is displayed in Fig. 5.13. PAN is the major sink of nitrogen. Reaction (R75), which modifies the CH_3CO_3 concentration, decreases the PAN mixing ratio. Reaction (R76) leads to formation of PAN, and therefore, the NO_x concentration is reduced. Reactions (R56) and (R68), which determine the gaseous

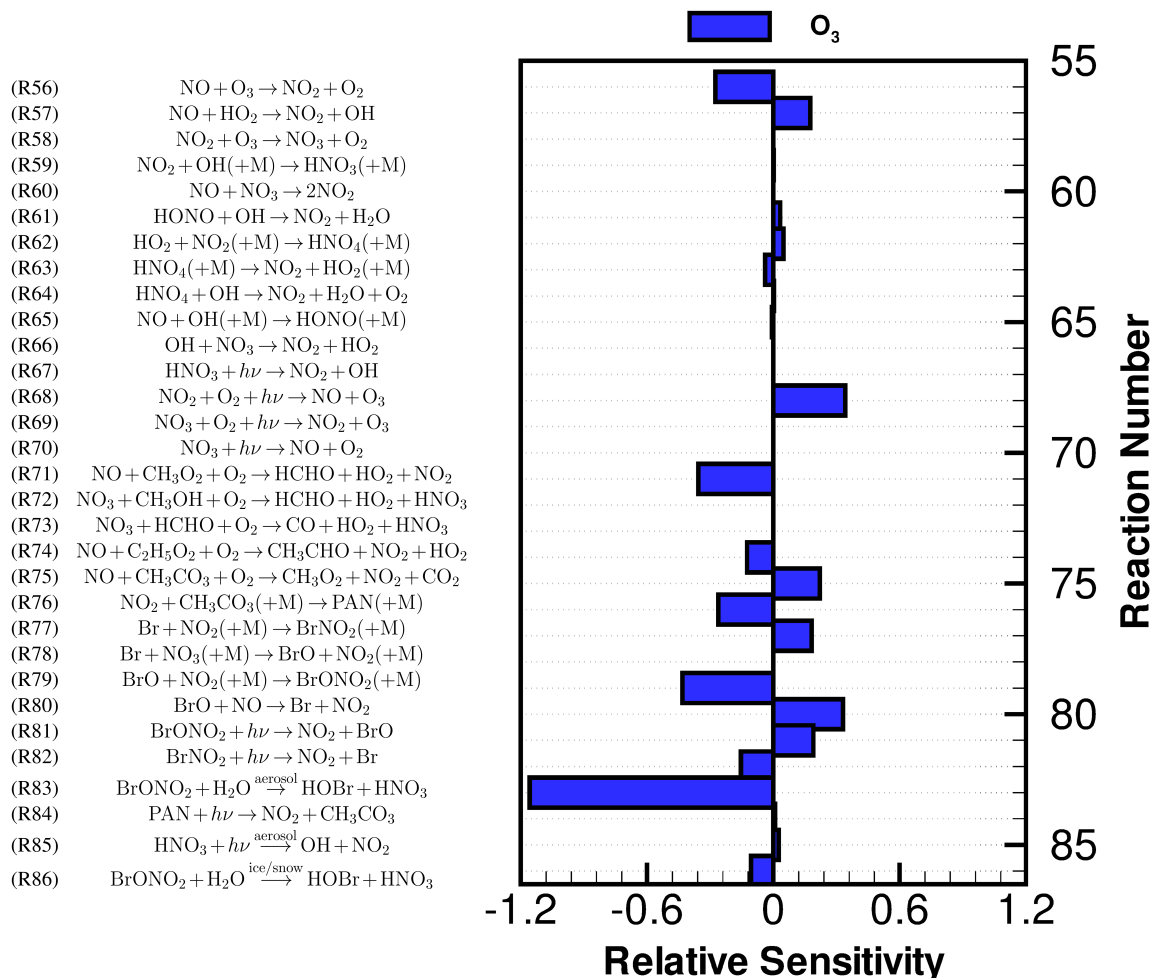


Figure 5.14: Relative sensitivities of O_3 concentrations at day 4 for a boundary layer height of 200 m [122].

NO and NO_2 ratio, are also crucial. It is worth noting that the hydrolysis reaction of BrONO_2 at the aerosol surface (R83) has a large impact on NO_x concentrations at this time. The BrONO_2 formation reaction (R79) and consumption reactions (R81) also have relatively high sensitivities within the ozone depletion stage. Thus, the importance of the chemical reaction cycle associated with BrONO_2 during the ozone depletion period is confirmed.

The relative sensitivities of the O_3 concentration for reactions related to NO_x at day 4 are shown in Fig. 5.14. The importance of each reaction on O_3 concentration is similar to those for the NO_x concentrations shown in Fig. 5.13. However, the sensitivities for PAN related reactions (reactions R75 and R76) are lower for ozone compared to NO_x . For ozone, the most important NO_x related reaction is the hydrolysis reaction of BrONO_2 at the aerosol surface (R83), since in this reaction, the HOBr concentration

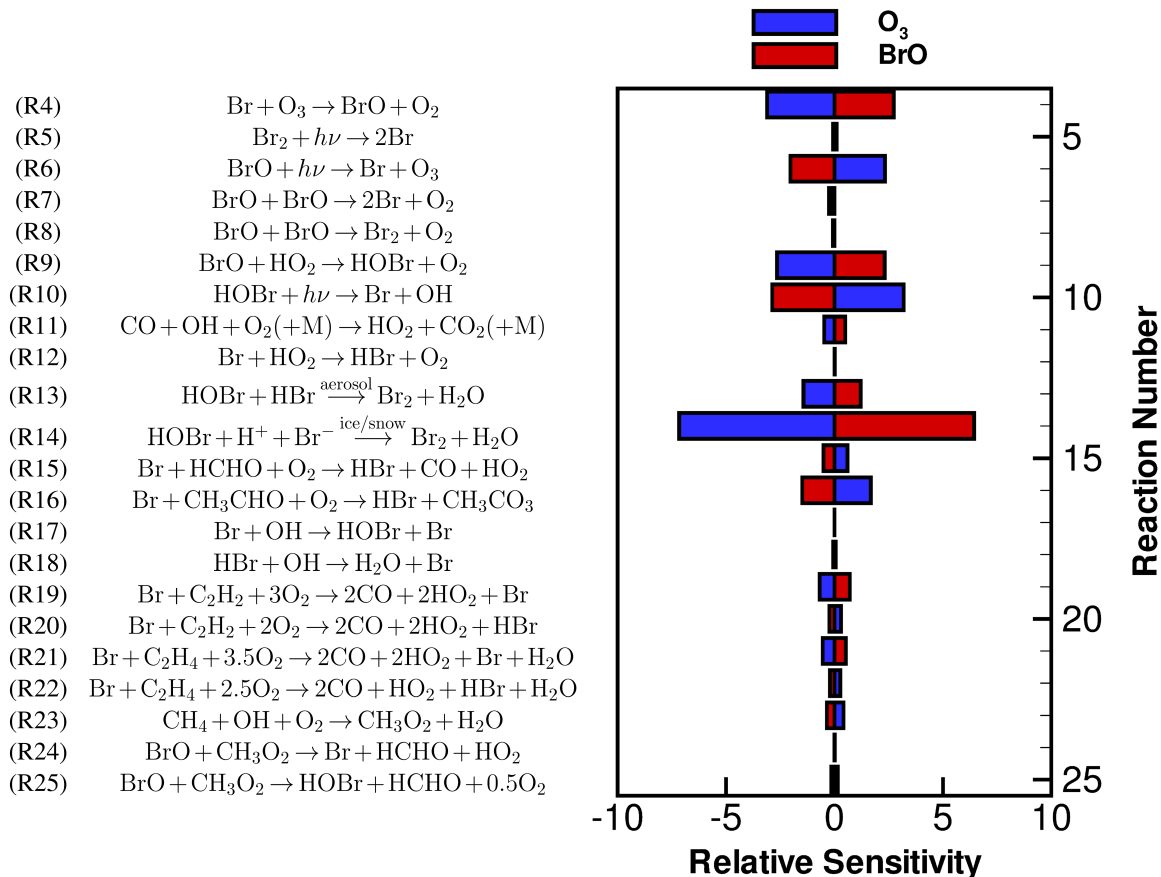


Figure 5.15: Relative sensitivities of O₃ and BrO concentrations at day 4 for a boundary layer height of 200 m [122].

is enhanced, leading to a reduced ozone concentration.

The importance of nitrogen related reactions versus bromine related reactions at day 4 is shown in Figs. 5.14 and 5.15. The bromine related reactions have a much higher sensitivity for ozone depletion compared to nitrogen related reactions at this time. A comparison of the sensitivity of bromine related reactions at day 6 for the bromine only mechanism, cf. Fig. 5.8, and the present mechanism at day 4 shows a relative higher sensitivity of the heterogeneous reaction (R14) due to the increased HOBr concentration in the NO_x mechanism (see Fig. 5.11a); this leads to a reduced importance of reactions (R4) and (R6) in the mechanism including NO_x related reactions. However, note that the time until O₃ depletion starts is considerably influenced by the presence of NO_x which is discussed below.

As discussed in section 2.2, nitrogen containing species are involved in both the

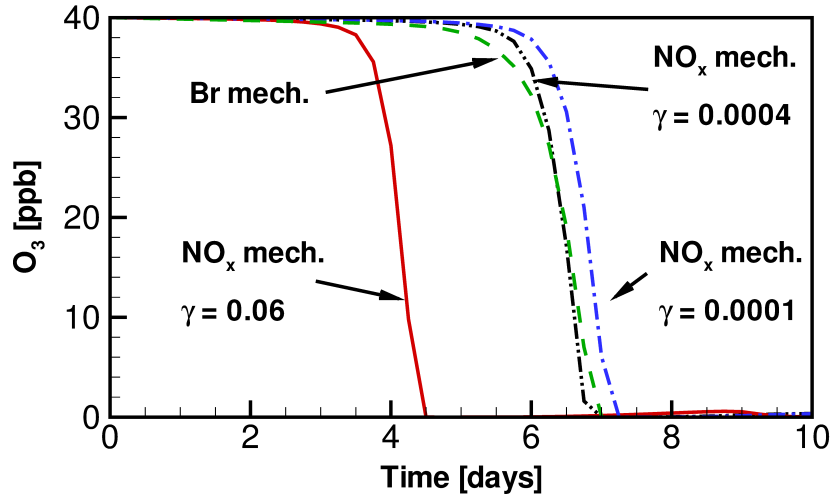
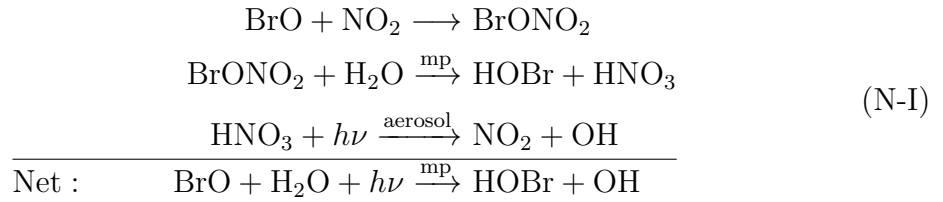
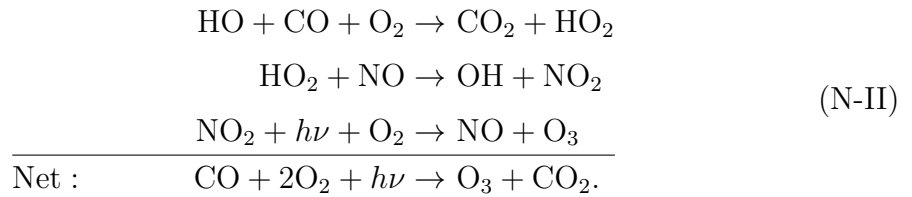


Figure 5.16: Ozone depletion rates with different values of BrONO_2 hydrolysis uptake coefficient [122].

ozone destruction cycle (N-I) and the production cycle (N-II):



and



The net effect on ozone depletion through NO_x species results from the balance between cycle (N-I) and (N-II). Thus, if the heterogeneous BrONO_2 hydrolysis reactions (R83) and (R86) are negligible ($\gamma = 0.0001$), which means that only a small amount of additional HOBr molecules can be formed through the nitrogen related reactions, the presence of nitrogen containing species slows down the ozone depletion as shown in Fig. 5.16. In contrast, when the value of the uptake coefficient of $\gamma = 0.06$ is used in reactions (R83) and (R86), ozone, in fact, is depleted earlier than computed with the bromine only mechanism. A critical turning value for the uptake coefficient of reactions (R83) and (R86) can be identified as $\gamma = 0.0004$. In this situation, the ozone produced by the nitrogen cycle equals the amount of ozone destroyed by the additional

HOBr induced by nitrogen heterogeneous reactions (R83) and (R86). Then, no effect of NO_x species on ozone concentration is observed, and the ozone depletion predicted equals the one in the bromine only mechanism. However, as the value of the uptake coefficient for the heterogeneous BrONO_2 hydrolysis reactions at the ice/snow surfaces or the aerosols is usually significantly larger than the obtained critical value in the present model. It might be concluded that the presence of the small amount of NO_x (15 ppt in the model) in the polar boundary layer may result in the acceleration of the reactive halogen release and the ozone depletion event.

The next section concerns the influence of chlorine related chemical reactions on ozone depletion.

5.1.3 Chlorine Related Chemical Reaction Mechanism

The detailed mechanism including both nitrogen and chlorine related species consists of 135 chemical reactions among 49 species, see Supplement. For the present computations, the reaction rate ratio $K_{\text{Br}_2/\text{BrCl}}$, of Br_2 and BrCl from the ice/snow surface, see reactions (R14) and (R129), equals 1.0, which means half of the deposited HOBr molecules are converted to Br_2 while the other half activate BrCl . Figure 5.17 shows the major chlorine containing species and ozone mixing ratio profiles versus time for a boundary layer height of 200 m. Compared to the NO_x related mechanism, the induction stage and the depletion stage in the chlorine related chemical reaction mechanism last 7.4 and 1.4 days, respectively. The total chlorine concentration amounts to 100 ppt

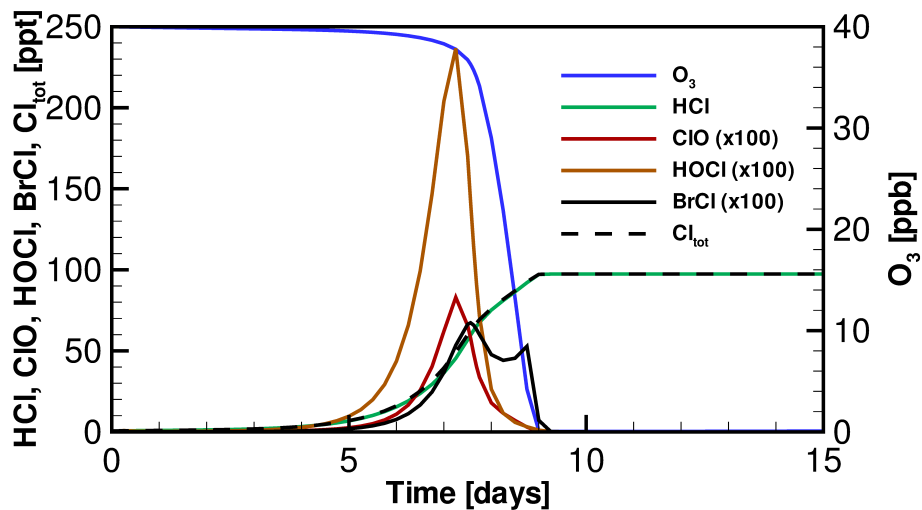


Figure 5.17: Time evolution of ozone, chlorine containing species and total chlorine concentrations, when the boundary layer height is 200 m [122].

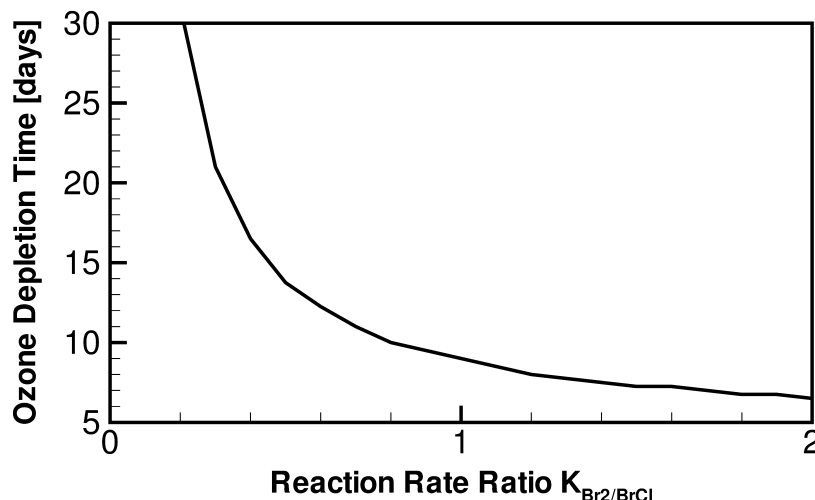


Figure 5.18: Impact of the reaction rate ratio of (R14) and (R129), $K_{Br_2/BrCl}$, on the ozone depletion time [122].

at the end of the event, mostly in the form of HCl. The mixing ratio of gaseous ClO is about 0.8 ppt, which is consistent with the measurements of Perner et al. [162] at Ny-Ålesund, reporting the ClO mixing ratio to be less than 2 ppt.

A parameter study is conducted for influence of the reaction rate ratio $K_{Br_2/BrCl}$ from the ice/snow surface, cf. (R14) and (R129), on the total ozone depletion time (ozone mixing ratio drops to less than 4 ppb). Figure 5.18 shows the total ozone depletion time to be about 6.5 days for $K_{Br_2/BrCl} = 2.0$. As the value of this ratio decreases, which means that less Br_2 is produced while more $BrCl$ molecules are released from the ground surface, the ozone depletion event is retarded. When the production ratio is less than 0.2, ozone depletion is hardly observed. This reveals that the ozone depletion time is strongly dependent on the reaction rate ratio $K_{Br_2/BrCl}$ for the formation of Br_2 and $BrCl$ from the ice/snow surface. Adams et al. [128] found in laboratory research that the major reaction product is Br_2 when the ice surface contains sufficient Br^- , whereas $BrCl$ is released as the major product if Br^- is significantly depleted in the ice or snow pack before ozone is consumed. Therefore, it can be concluded that the chemical composition of the ground surface is important for the ozone depletion rate.

The change of active bromine and chlorine radical concentrations with time versus ozone concentration is plotted in Fig. 5.19. As the ozone depletes, an exponential increase of the active bromine radicals is observed, whereas the enhancement of Cl is approximately steady. Thus, the destruction of ozone is dominantly dependent on Br atoms and not on the Cl atoms. The calculated ratio of $[Br/Cl]$ during ozone depletion is of the order 10^3 . This means that more than 99% of the ozone is consumed directly

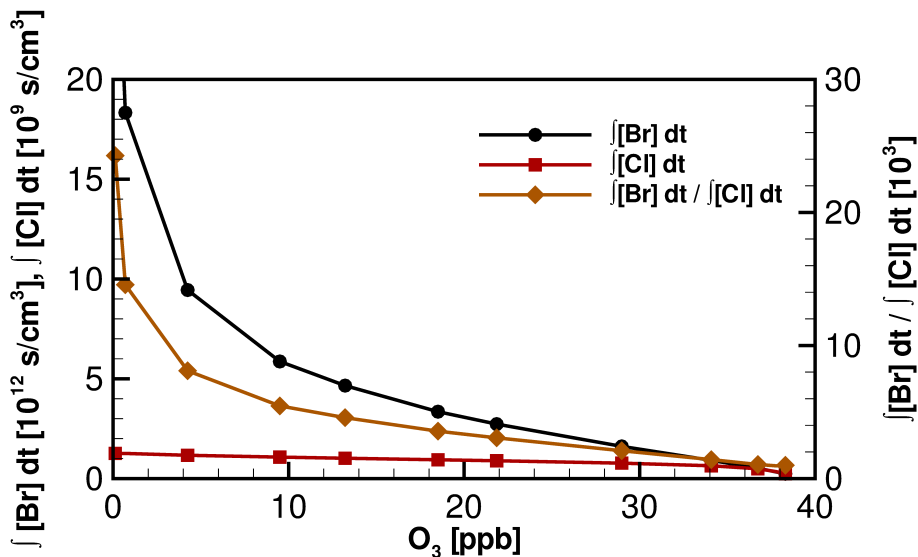


Figure 5.19: Time integrated halogen atom concentrations and the $[Br]/[Cl]$ ratio versus the ozone mixing ratio [122].

by Br radicals. Previous experimental studies using the VOC decay measurement method suggest various values for the $[Br]/[Cl]$ ratio, ranging from tens to more than ten thousand [163, 164, 165, 166]. However, most of the studies find values in the order of some hundreds. Michalowski et al. [93] suggested that the possible reason for the relatively high modeled value of the $[Br/Cl]$ ratio may be an underestimation of the Cl mixing ratio. Spicer et al. [167] recommend that an additional unknown Cl source should be assumed, which has not yet been considered in any model study until now.

The present investigation of the influence of chlorine chemistry shows that chlorine containing species have minor direct influence on ozone depletion compared to NO_x and bromine.

5.1.4 Skeletal Chemical Reaction Mechanism

In order to implement an affordable and reliable chemical reaction mechanism in the 3-D simulations, it is necessary to determine the possible removal of chemical reactions from the system. Thus, a closer look at the reactions with low sensitivities in the bromine only mechanism is necessary. For instance, although reaction (R5) has a relative lower sensitivity for ozone and bromine species (see Fig. 5.8), this reaction should be kept, because the initial bromine in the mechanism stems mainly in the form of Br_2 , and (R5) is the only reaction for converting the initial Br_2 into Br, so that the initial bromine can get involved into the reaction cycle.

A comparison of the temporal changes of the relative sensitivities of reactions (R7),

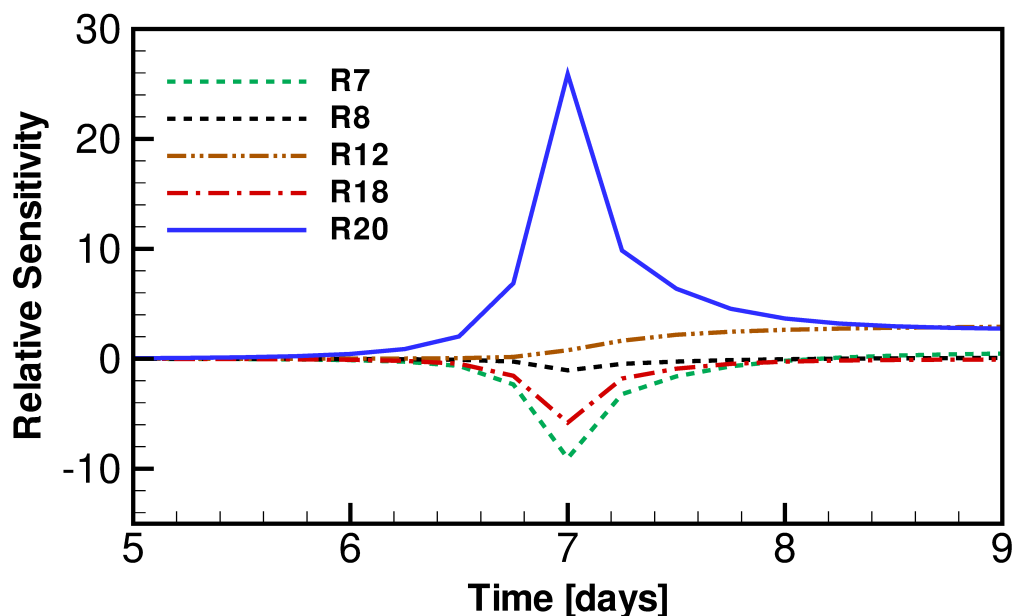


Figure 5.20: Temporal behavior of relative sensitivities of ozone for a 200 meters boundary layer height.

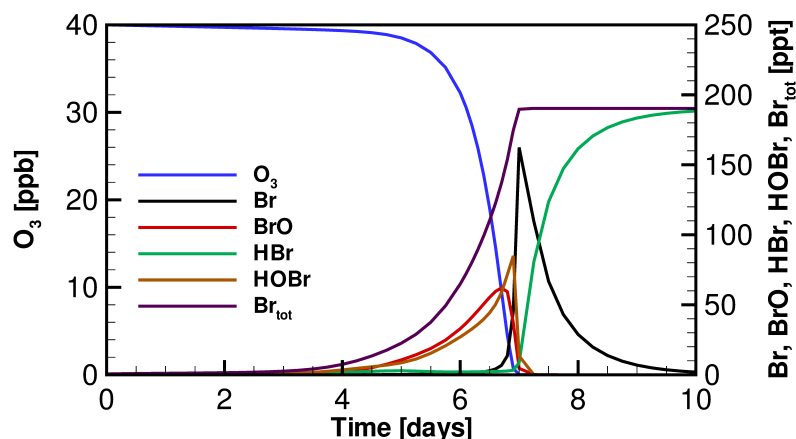
(R8), (R12), (R18), and (R20) (see Appendix B and Tab. 5.6) is shown in Fig. 5.20. The sensitivity of (R20) increases after day 5, which is the start of the "depletion stage", peaking at day 7, then it decreases rapidly. Reaction (R12) is more significant during the "end stage". All the reactions shown in Fig. 5.20 are removed in the skeletal mechanism except for (R20) and (R7).

The sensitivity analysis performed concerns the principal chemical species O_3 , Br, BrO, and HOBr over the whole time period, and totally, 27 reactions and the four species C_2H_5 , C_2H_6 , CH_3OH , and $\text{C}_2\text{H}_5\text{O}$, are removed from the original detailed bromine only mechanism. The remaining 28 reactions among 26 species are marked in Tab. 5.6.

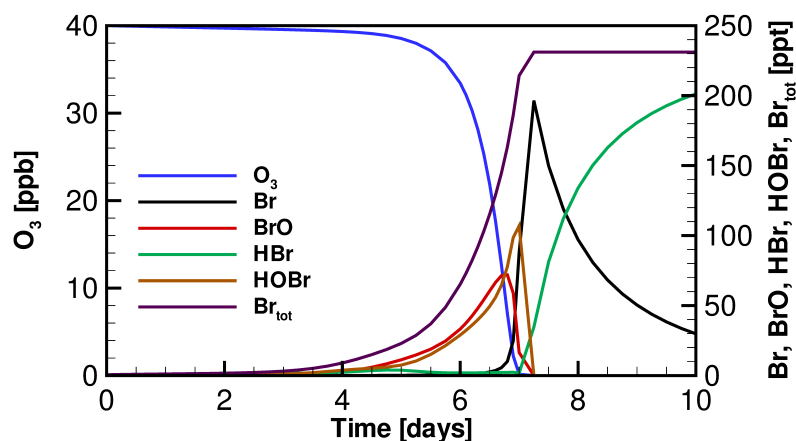
The time variation of mixing ratio of ozone and bromine species for the boundary layer height of 200 m using the detailed chemical reaction mechanism may be compared to the corresponding results obtained with the skeletal mechanism displayed in Fig. 5.21. It can be seen that the major features such as evolution and peak values of species concentrations are maintained, and the skeletal mechanism is suitable to be implemented into the 3-D model.

Table 5.6: Bromine only mechanism for ozone depletion and bromine explosion.

No.	Reaction	k [(molec. /cm ³) ¹⁻ⁿ /s]	Reac. order	Reference	Skeletal
R1	$O_3 + h\nu \rightarrow O(^1D) + O_2$	$4.70 \cdot 10^{-7}$	1	Lehrer et al. [105]	*
R2	$O(^1D) + O_2 \rightarrow O_3$	$4.20 \cdot 10^{-11}$	2	Atkinson et al. [168]	*
R3	$O(^1D) + H_2O \rightarrow 2OH$	$2.30 \cdot 10^{-10}$	2	Atkinson et al. [168]	*
R4	$Br + O_3 \rightarrow BrO + O_2$	$7.65 \cdot 10^{-13}$	2	Atkinson et al. [168]	*
R5	$Br_2 + h\nu \rightarrow 2Br$	0.021	1	Lehrer et al. [105]	*
R6	$BrO + h\nu \xrightarrow{O_2} Br + O_3$	0.014	1	Lehrer et al. [105]	*
R7	$BrO + BrO \rightarrow 2Br + O_2$	$1.92 \cdot 10^{-12}$	2	Atkinson et al. [168]	*
R8	$BrO + BrO \rightarrow Br_2 + O_2$	$5.42 \cdot 10^{-13}$	2	Atkinson et al. [168]	*
R9	$BrO + HO_2 \rightarrow HOBr + O_2$	$4.31 \cdot 10^{-11}$	2	Atkinson et al. [168]	*
R10	$HOBr + h\nu \rightarrow Br + OH$	$3.00 \cdot 10^{-4}$	1	Lehrer et al. [105]	*
R11	$CO + OH \xrightarrow{O_2} HO_2 + CO_2$	$2.40 \cdot 10^{-13}$	2	Atkinson et al. [168]	*
R12	$Br + HO_2 \rightarrow HBr + O_2$	$1.42 \cdot 10^{-12}$	2	Atkinson et al. [168]	*
R13	$HOBr + HBr \xrightarrow{aerosol} Br_2 + H_2O$	See text			*
R14	$HOBr + H^+ + Br^- \xrightarrow{snow/ice} Br_2 + H_2O$	See text			*
R15	$Br + HCHO \xrightarrow{O_2} HBr + CO + HO_2$	$7.65 \cdot 10^{-13}$	2	Atkinson et al. [168]	*
R16	$Br + CH_3CHO \xrightarrow{O_2} HBr + CH_3CO_3$	$3.22 \cdot 10^{-12}$	2	Atkinson et al. [168]	*
R17	$Br_2 + OH \rightarrow HOBr + Br$	$5.66 \cdot 10^{-11}$	2	Atkinson et al. [168]	*
R18	$HBr + OH \rightarrow H_2O + Br$	$1.23 \cdot 10^{-11}$	2	Atkinson et al. [168]	*
R19	$Br + C_2H_2 \xrightarrow{3O_2} 2CO + 2HO_2 + Br$	$4.20 \cdot 10^{-14}$	2	Borken [169]	*
R20	$Br + C_2H_2 \xrightarrow{2O_2} 2CO + HO_2 + HBr$	$8.92 \cdot 10^{-14}$	2	Borken [169]	*
R21	$Br + C_2H_4 \xrightarrow{3.5O_2} 2CO + 2HO_2 + Br + H_2O$	$2.53 \cdot 10^{-13}$	2	Barnes et al. [170]	*
R22	$Br + C_2H_4 \xrightarrow{2.5O_2} 2CO + HO_2 + HBr + H_2O$	$5.34 \cdot 10^{-13}$	2	Barnes et al. [170]	*
R23	$CH_4 + OH \xrightarrow{O_2} CH_3O_2 + H_2O$	$2.46 \cdot 10^{-15}$	2	Atkinson et al. [168]	*
R24	$BrO + CH_3O_2 \rightarrow Br + HCHO + HO_2$	$1.60 \cdot 10^{-12}$	2	Aranda et al. [171]	*
R25	$BrO + CH_3O_2 \rightarrow HOBr + HCHO + 0.5O_2$	$4.10 \cdot 10^{-12}$	2	Aranda et al. [171]	*
R26	$OH + O_3 \rightarrow HO_2 + O_2$	$3.94 \cdot 10^{-14}$	2	Atkinson et al. [168]	*
R27	$OH + HO_2 \rightarrow H_2O + O_2$	$1.26 \cdot 10^{-10}$	2	Atkinson et al. [168]	*
R28	$OH + H_2O_2 \rightarrow HO_2 + H_2O$	$1.56 \cdot 10^{-12}$	2	Atkinson et al. [168]	*
R29	$OH + OH \xrightarrow{O_2} H_2O + O_3$	$2.12 \cdot 10^{-12}$	2	Atkinson et al. [168]	*
R30	$HO_2 + O_3 \rightarrow OH + 2O_2$	$1.37 \cdot 10^{-15}$	2	Atkinson et al. [168]	*
R31	$HO_2 + HO_2 \rightarrow O_2 + H_2O_2$	$4.65 \cdot 10^{-12}$	2	Atkinson et al. [168]	*
R32	$C_2H_6 + OH \rightarrow C_2H_5 + H_2O$	$1.46 \cdot 10^{-13}$	2	Atkinson et al. [168]	*
R33	$C_2H_5 + O_2 \rightarrow C_2H_4 + HO_2$	$3.80 \cdot 10^{-15}$	2	Atkinson et al. [168]	*
R34	$C_2H_5 + O_2(+M) \rightarrow C_2H_5O_2(+M)$	$7.12 \cdot 10^{-12}$	2	Atkinson et al. [168]	*
R35	$C_2H_4 + OH \xrightarrow{1.5O_2} CH_3O_2 + CO + H_2O$	$8.20 \cdot 10^{-12}$	2	Atkinson et al. [168]	*
R36	$C_2H_4 + O_3 \rightarrow HCHO + CO + H_2O$	$4.33 \cdot 10^{-19}$	2	Sander et al. [98]	*
R37	$C_2H_2 + OH \xrightarrow{1.5O_2} HCHO + CO + HO_2$	$7.50 \cdot 10^{-13}$	2	Atkinson et al. [168]	*
R38	$C_3H_8 + OH \xrightarrow{2O_2} C_2H_5O_2 + CO + 2H_2O$	$8.13 \cdot 10^{-13}$	2	Atkinson et al. [168]	*
R39	$HCHO + OH \xrightarrow{O_2} CO + H_2O + HO_2$	$9.29 \cdot 10^{-12}$	2	Atkinson et al. [168]	*
R40	$CH_3CHO + OH \xrightarrow{O_2} CH_3CO_3 + H_2O$	$1.86 \cdot 10^{-11}$	2	Atkinson et al. [168]	*
R41	$CH_3O_2 + HO_2 \rightarrow CH_3O_2H + O_2$	$7.81 \cdot 10^{-12}$	2	Atkinson et al. [168]	*
R42	$CH_3OOH + OH \rightarrow CH_3O_2 + H_2O$	$3.97 \cdot 10^{-12}$	2	Atkinson et al. [168]	*
R43	$CH_3OOH + OH \rightarrow HCHO + OH + H_2O$	$2.09 \cdot 10^{-12}$	2	Atkinson et al. [168]	*
R44	$CH_3OOH + Br \rightarrow CH_3O_2 + HBr$	$5.19 \cdot 10^{-15}$	2	Atkinson et al. [168]	*
R45	$CH_3O_2 + CH_3O_2 \rightarrow CH_3OH + HCHO + O_2$	$3.06 \cdot 10^{-13}$	2	Atkinson et al. [168]	*
R46	$CH_3O_2 + CH_3O_2 \xrightarrow{O_2} 2HCHO + 2HO_2$	$1.50 \cdot 10^{-13}$	2	Atkinson et al. [168]	*
R47	$CH_3OH + OH \xrightarrow{O_2} HCHO + HO_2 + H_2O$	$7.68 \cdot 10^{-13}$	2	Atkinson et al. [168]	*
R48	$C_2H_5O_2 + C_2H_5O_2 \rightarrow C_2H_5O + C_2H_5O + O_2$	$6.80 \cdot 10^{-14}$	2	Atkinson et al. [168]	*
R49	$C_2H_5O + O_2 \rightarrow CH_3CHO + HO_2$	$7.44 \cdot 10^{-15}$	2	Sander et al. [98]	*
R50	$C_2H_5O + O_2 \rightarrow CH_3O_2 + HCHO$	$7.51 \cdot 10^{-17}$	2	Sander et al. [98]	*
R51	$C_2H_5O_2 + HO_2 \rightarrow C_2H_5OOH + O_2$	$1.31 \cdot 10^{-11}$	2	Atkinson et al. [168]	*
R52	$C_2H_5OOH + OH \rightarrow C_2H_5O_2 + H_2O$	$8.21 \cdot 10^{-12}$	2	Sander et al. [98]	*
R53	$C_2H_5OOH + Br \rightarrow C_2H_5O_2 + HBr$	$5.19 \cdot 10^{-15}$	2	Sander et al. [98]	*
R54	$OH + OH(+M) \rightarrow H_2O_2(+M)$	$5.21 \cdot 10^{-12}$	2	Atkinson et al. [168]	*
R55	$H_2O_2 + h\nu \rightarrow 2OH$	$2.00 \cdot 10^{-6}$	1	Lehrer et al. [105]	*



(a) Detailed mechanism



(b) Skeletal mechanism

Figure 5.21: Time variation of mixing ratio of ozone and bromine species for the boundary layer height of 200 m for the detailed and skeletal bromine only mechanism in the box model study.

5.2 Three-Dimensional Model

The full set of time and spatial dependent equations (Eqs. (3.11) – (3.14)) including convection, turbulent mixing and chemical production and consumption are solved in the three-dimensional model. The skeletal mechanism obtained above is used to calculate the chemical production or consumption source terms. Surfaces with different shapes are applied as the bottom boundary of the computational domain.

5.2.1 Model with a Flat Surface

5.2.1.1 Initial Conditions

A flat surface is used as the bottom boundary of the computational domain as shown in Fig. 5.22. The initial model settings representing the Arctic weather conditions are taken from the LES study of stable boundary layer from GABLS (Global energy and water cycle experiment Atmospheric Boundary Layer Study) initiative [126]. The initial settings are consistent with the measurement data detected by flight number 7 in the Beaufort Sea Arctic Stratus Experiment on October 1, 1994 [172]. The size of the computational domain is $400 \text{ m} \times 400 \text{ m} \times 400 \text{ m}$. The isotropic grid length of 6.25 m is used so that 65 grid nodes are uniformly distributed in each direction. It has been confirmed by Simpson et al. [79] that this mesh resolution is fine enough to capture the principal properties of the flow.

The geostrophic wind speed is 8 m s^{-1} along the horizontal x -direction as the initial imposed wind is $(8 \text{ m s}^{-1}, 0 \text{ m s}^{-1}, 0 \text{ m s}^{-1})$. It is possible that a strong wind condition can occur in polar regions and some studies [114, 115, 116, 117] have been done for the

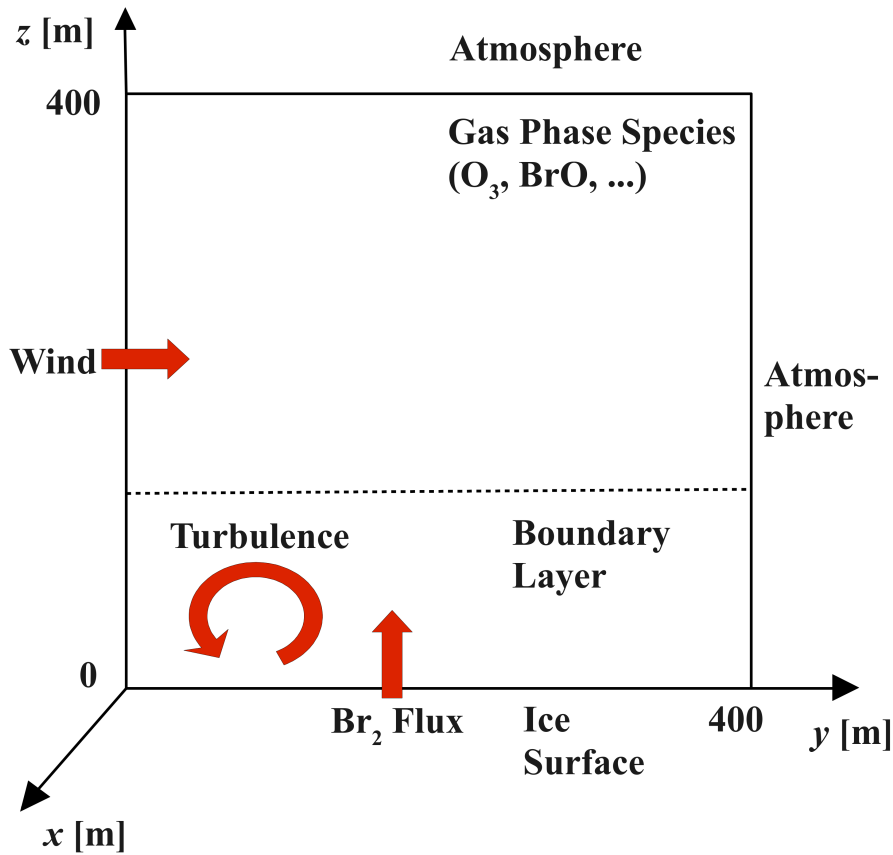


Figure 5.22: Schematic depiction of the simulation with a flat ground surface [155].

investigation of the ozone depletion under a stormy, blowing snow condition. However, most of the ozone depletion events in polar regions are reported with a low wind speed weather condition [79]. Therefore, the situation under 8 m s^{-1} wind speed is more focused on in the present study. A preliminary parameter study is conducted for the influence of the wind speed on the development of the boundary layer, which is presented in section 5.2.1.3.

The initial potential temperature profile consists of a 100 m well-mixed bottom layer of 265 K and an inverse temperature gradient of 0.01 K/m up to 400 m height. The underlying bottom surface is colder than the ambient air, thus a stable boundary layer develops. The temperature inversion suppresses the turbulent mixing, whereas the wind shear enhances the mixing. These overlying processes cause a reduction of the size of the eddies inside the stable boundary layer.

5.2.1.2 Boundary Conditions

At the top boundary of the computational domain, slip condition is used for the velocity. The vertical component $U_z = 0 \text{ m s}^{-1}$, and zero gradients are applied for the horizontal components U_x and U_y . Potential temperature attains a fixed gradient, $\frac{\partial \theta}{\partial z} = 0.01 \text{ K m}^{-1}$. The fixed gradient condition $\frac{\partial p}{\partial z} = -\rho g$ is used for the pressure. For all chemical species, Neumann (zero gradient) boundary conditions are used.

At the bottom boundary, the Monin-Obukhov similarity [173] is applied for the velocity. In the Monin-Obukhov similarity, the wall shear stress tensor at the surface is given as:

$$(\tau + \tau_t^D)_{i3,w} = -\rho u_*^2 \left[\frac{u_i(z_1)}{U(z_1)} \right] \quad (i = 1, 2). \quad (5.1)$$

τ is the molecular viscous stress tensor and τ_t^D is the deviatoric part of the subgrid stress tensor. The subscript “w” represents the value at the bottom wall surface. $i = 1, 2$ denotes the component along x or y direction. $z_1 = \delta_z/2$, where $\delta_z = 6.25 \text{ m}$ is the height of the first level of the grid along the vertical z direction. $u_i(z_1)$ is the resolved velocity at the height of z_1 and $U(z_1)$ is the horizontally averaged velocity at this height. The friction velocity u_* is calculated by

$$u_* = \frac{U(z_1)\kappa}{\log\left(\frac{z_1}{z_0}\right) + \beta_m \frac{z_1}{L}}. \quad (5.2)$$

z_0 is the roughness length expressing the roughness of the surface. In this simulation, $z_0 = 0.1 \text{ m}$ [126, 172] is used for the momentum and energy equations. This roughness length is high compared to the typical value of the roughness length for the sea ice or snow (about 10^{-6} to 10^{-3} m) in polar regions. However, using a lower z_0 value would result in an under-resolved surface layer [172]. $\kappa = 0.4$ is the Von Karman’s constant.

The constant $\beta_m = 4.8$ [97] and L is the Obukhov length. As $z_1 \ll L$ in the present model, a simplified friction velocity is used and the form is as follows:

$$u_* = \frac{U(z_1)\kappa}{\log(\frac{z_1}{z_0})}. \quad (5.3)$$

For the potential temperatures, in the validations of the 3-D model, a surface cooling of 0.25 K hour^{-1} is used for the initial 9 hours as the same condition used in the GABLS simulation [126]. For the investigation of the vertical distribution of chemical species in the order of days, in contrast to the GABLS simulation where surface cooling is used specially for a nocturnal boundary layer, a constant potential temperature of 260 K at the bottom surface is assumed, which refers to the average ice surface temperature in polar regions [155]. Similar as the shear stress tensor, the heat flux at the bottom of the surface is modeled as [173]:

$$q = -\frac{u_*\kappa[\theta_w - \Theta(z_1)]}{\log(\frac{z_1}{z_0}) + \beta_h}, \quad (5.4)$$

in which θ_w is the surface temperature, $\Theta(z_1)$ is the spatial averaged potential temperature at the height of z_1 . The constant β_h equals 7.8 [97]. The boundary condition for the pressure is the fixed gradient condition $\frac{\partial p}{\partial z} = -\rho g$. For the chemical species concentrations, zero gradient conditions are applied except the species HOBr, Br₂ and H₂O. For these species involved in the heterogeneous reactions, the vertical gradient of the species concentration is calculated based on the parametrization of the heterogeneous reaction occurring at the ice surface. The details of the parametrization are described in section 3.1 of the thesis.

At the lateral sides boundaries, periodic boundary conditions are used, which represents a computational domain with an infinite horizontal length.

5.2.1.3 Results

Figures 5.23 and 5.24 show a two-dimensional plot of the instantaneous velocity components in x and y directions, respectively, at position $x = 200 \text{ m}$ at different times. It is found that the initially imposed wind shear causes the development of the boundary layer, the thickness of the boundary layer increases and reaches a stable height after about 9 hours. Due to the combined effects of the surface friction and Coriolis force, near the top of the boundary layer, the value of the horizontal wind velocity along the x direction increases and exceeds the initial geostrophic wind speed of 8 m/s , whereas the velocity along y direction decreases. This super-geostrophic wind speed is called "low-level jet" [97], which is often found at night time or in polar regions.

The super-geostrophic jet of wind speed is also observed in the vertical distribution of the mean wind profiles shown in Fig. 5.25. The wind speed and angle are averaged

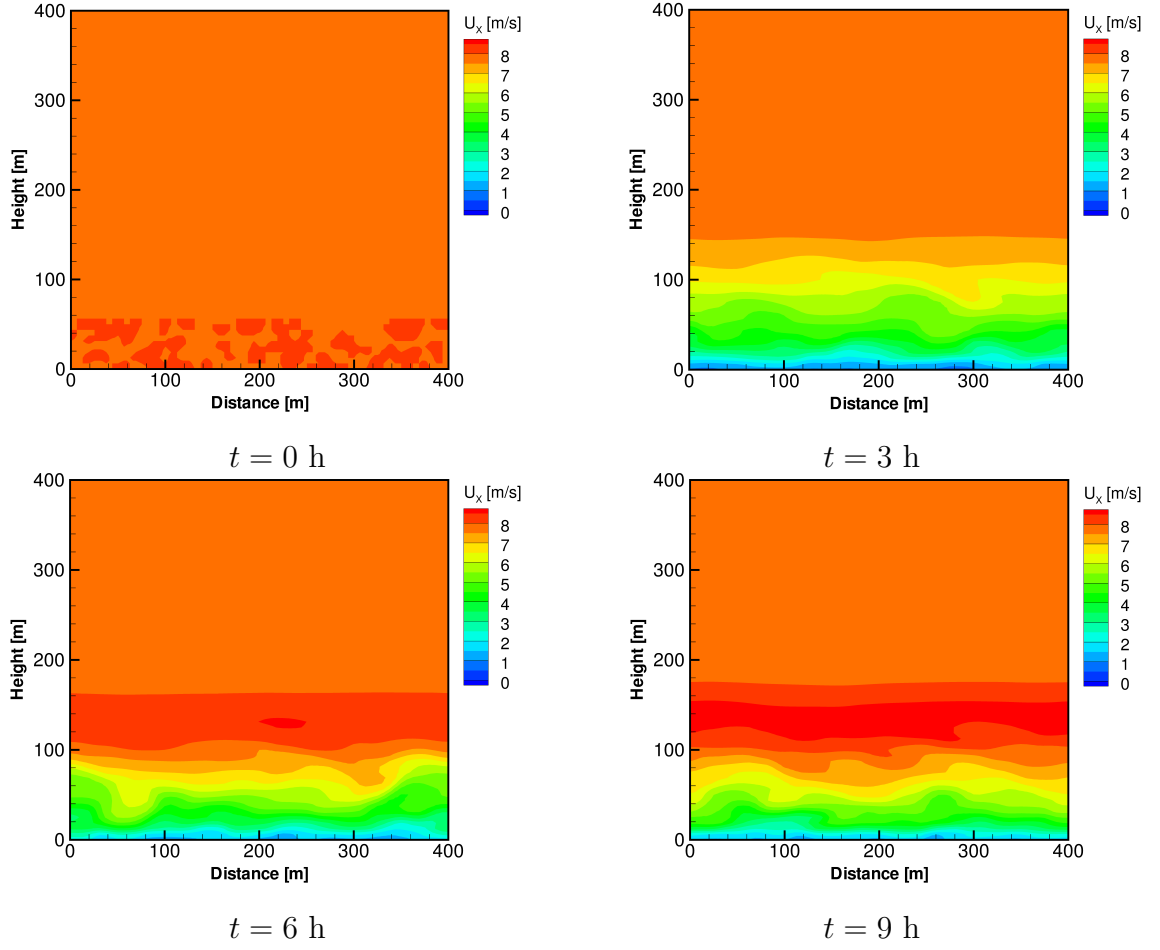


Figure 5.23: Instantaneous velocity in x direction at cut plane $x = 200$ m [155].

over the horizontal direction and over the 9th hour after the mean profiles have reached a quasi-steady state [126]. It is observed that the wind speed increases with height until it reaches the peak value of more than 9 m/s at around 150 m, then it decreases to the geostrophic wind speed. The angle between the geostrophic wind and the surface wind direction is about 36 degrees. These results are in agreement with the previous LES results of GABLS simulations [126], validating the present model and the numerical scheme. At the surface, the obtained value of the friction velocity is 0.22 m/s, which is within the value range 0.22-0.59 m/s in the field observational program CASES-99 (Cooperative Atmosphere-Surface Exchange Study) [174] conducted in the clear sky, calm near-surface wind and stable boundary layer conditions.

The instantaneous vertical velocity distribution at the 9th hour is shown in Fig. 5.26 both in (a) 3D view and (b) 2D at cut plane $x = 0$ m. In Fig. 5.26 (a), red and blue regions demonstrate that the air parcels are moving upwards and downwards, respectively. It represents that the resolved scale turbulent fluctuations enhance the mixing within the boundary layer. Besides, it can be also observed from Fig. 5.26 (b)

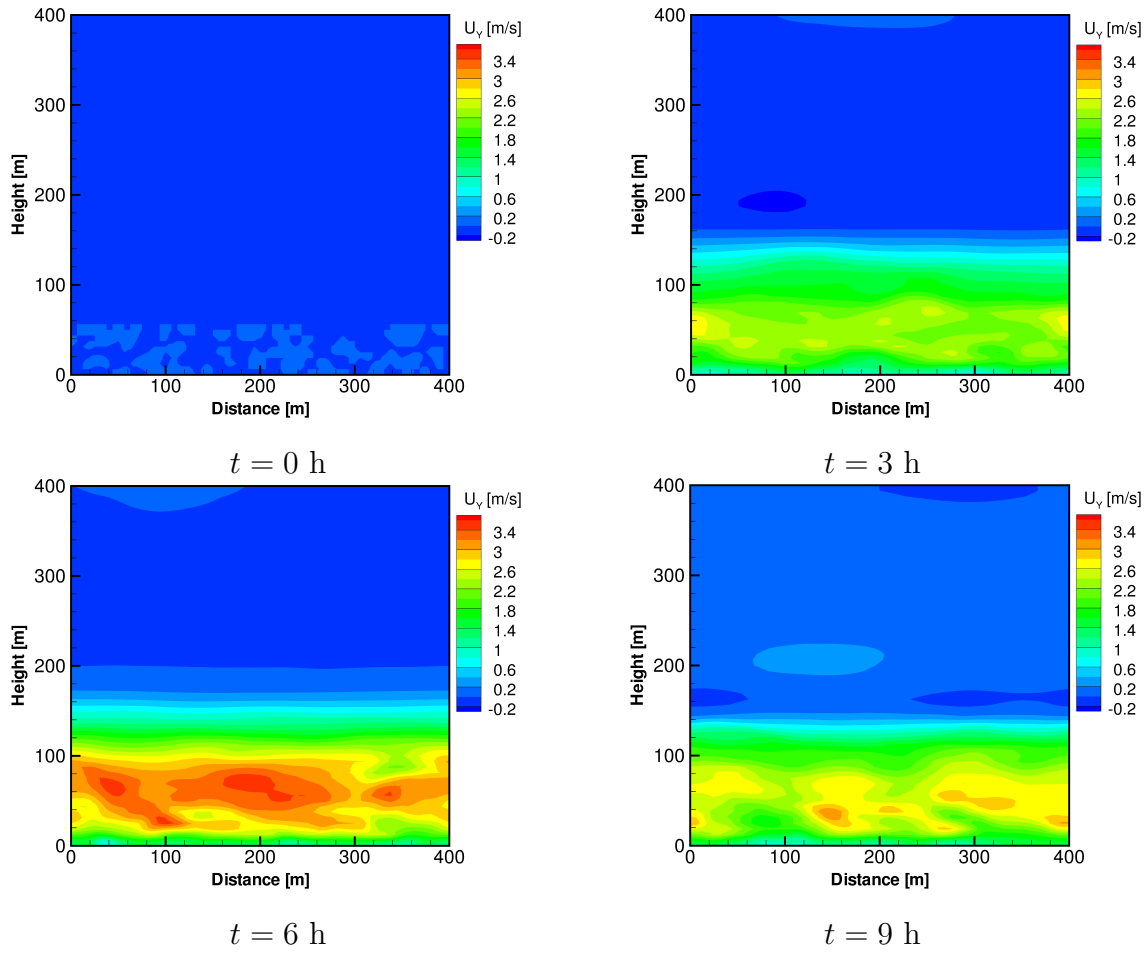


Figure 5.24: Instantaneous velocity in y direction at cut plane $x = 200 \text{ m}$ [155].

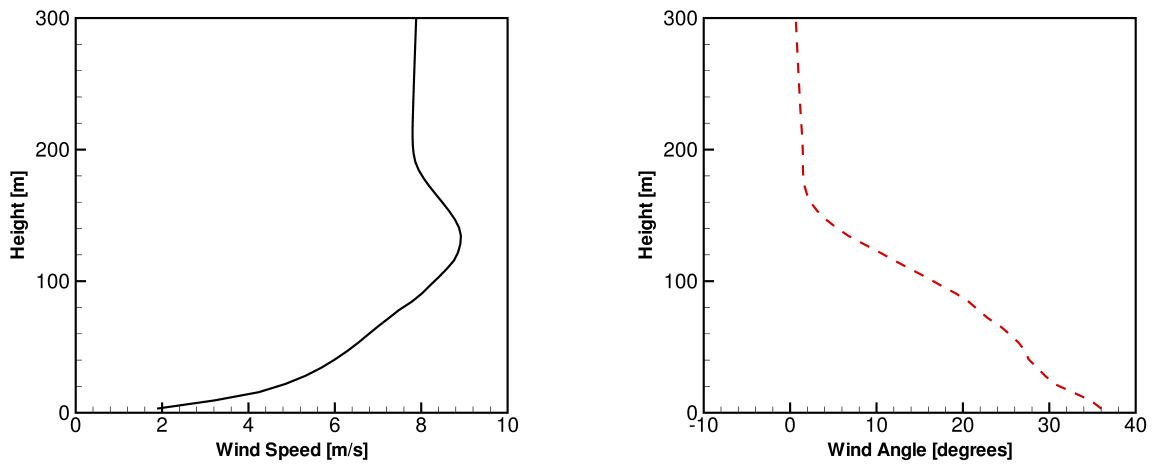


Figure 5.25: Vertical distribution of averaged wind profiles over the 9th hour [155]. Left: wind speed; Right: wind angle.

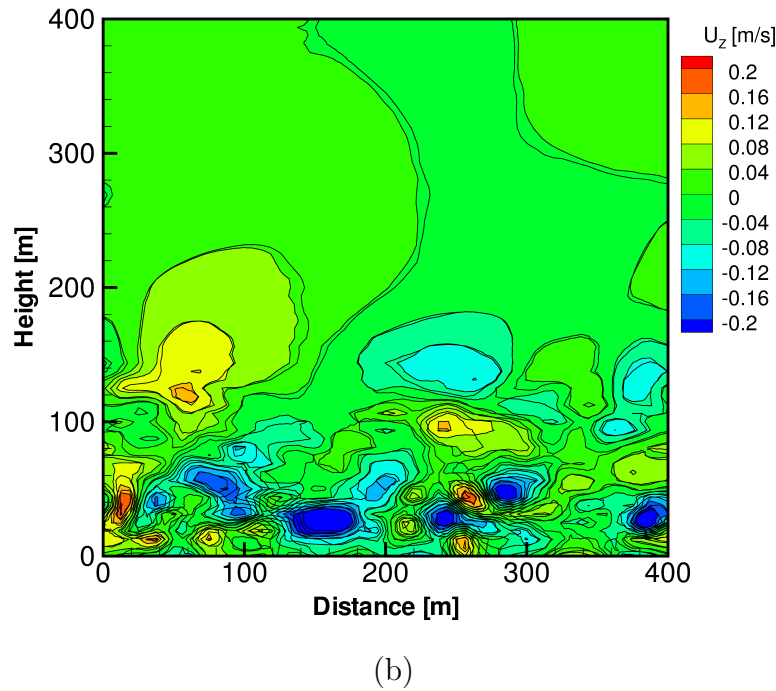
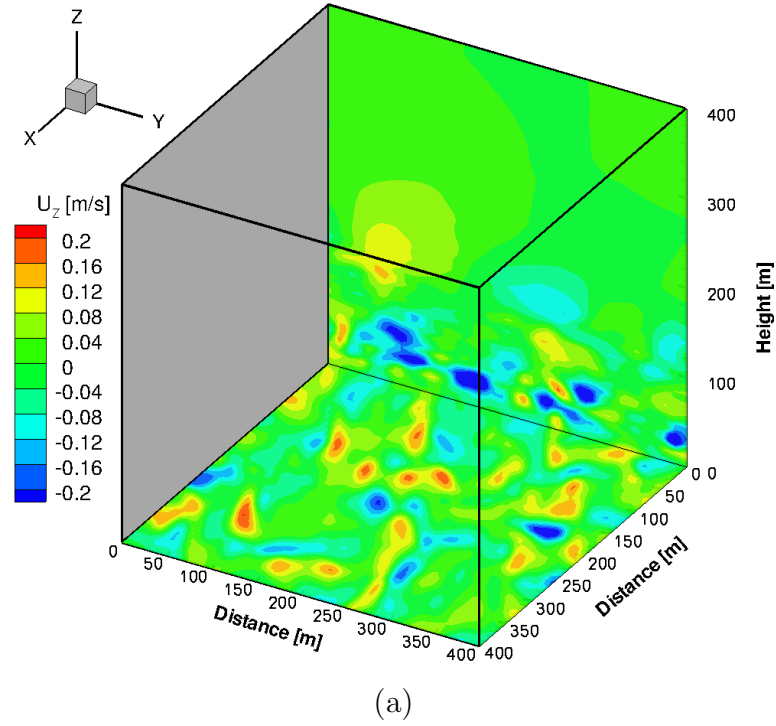


Figure 5.26: Distribution of the instantaneous vertical velocity at hour 9 in (a) 3D view and (b) 2D view cut plane at $x = 0$ m [155].

that the resolved scale eddies reside mostly below the height of about 200 m and, more frequently, at the height of about 30-40 meters.

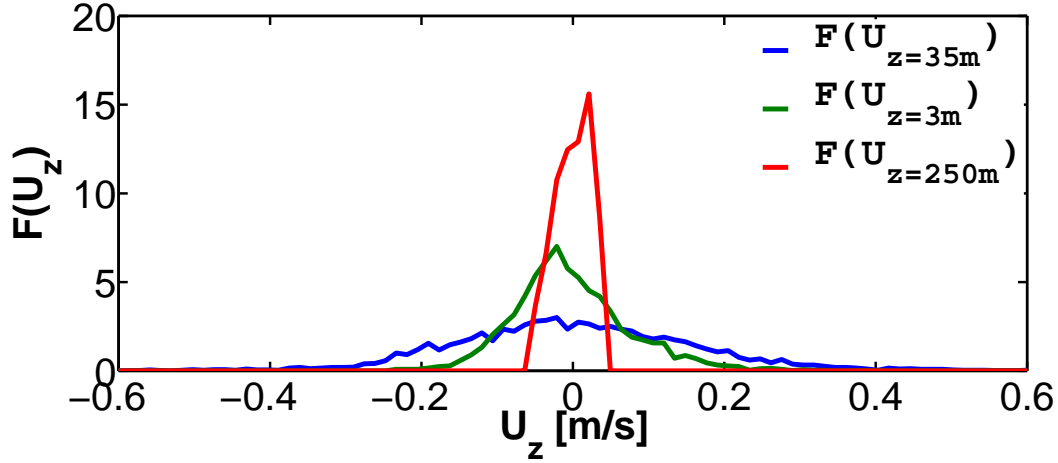


Figure 5.27: Probability density function for the instantaneous vertical velocity at the 9th hour. $F(U_z)$ is the probability density function and U_z is the vertical velocity at different heights (3 m, 35 m and 250 m).

In order to describe the relative occurrence probability of the random vertical velocity, the probability density functions (pdf) of the vertical velocity at different time steps and heights are calculated. The definition of a pdf $F(x)$ with the variable x is defined as:

$$\int_{x_{\min}}^{x_{\max}} F(x) dx = 1. \quad (5.5)$$

Figure 5.27 shows $F(U_z)$ at the 9th hour at different heights. It is displayed in Fig. 5.27 that the profiles of the pdf are distributed equally on the lateral sides of the average value $\overline{U_z} = 0$. Besides, as the height increases from the bottom surface (3.125 m) to the height of about 35 m, the pdf profile becomes wider, representing stronger and more frequent fluctuations at the height of 35 m. This is consistent with the height where most of the resolved scale fluctuations are found, see Fig. 5.26 (b). As the altitude increases to the height of 250 m, the pdf profile becomes extremely narrow, denoting very weak resolved scale turbulent mixing at this height, which resides out of the boundary layer.

The effective turbulent diffusivity at different heights is estimated and shown in Fig. 5.28. The definition of the effective turbulent diffusivity is as follows [126]:

$$k_{\text{eff}} = \frac{(\tau_{xz}^2 + \tau_{yz}^2)^{\frac{1}{2}}}{\rho \left(\frac{\partial U^2}{\partial x} + \frac{\partial V^2}{\partial y} \right)^{\frac{1}{2}}}. \quad (5.6)$$

The total (resolved plus subgrid) mixing ability of the turbulent flow can be represented by the effective turbulent diffusivity. It is seen from Fig. 5.28 that the maximum value of k_{eff} occurs at the height of about 35 m, which again confirms the results of Fig. 5.26 (b).

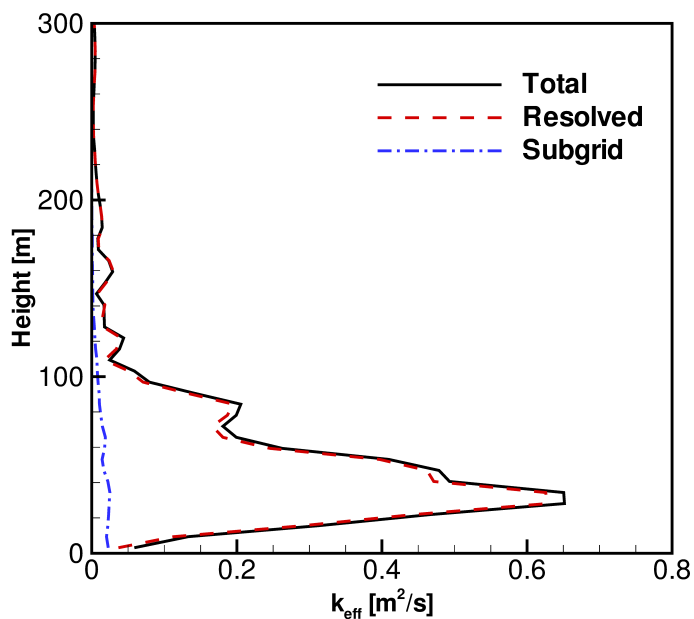


Figure 5.28: Averaged effective turbulent diffusivity over the 9th hour [155].

The 3D simulation is continued until the surface ozone is almost completely consumed. In Fig. 5.29, the vertical distributions of ozone and major bromine species at day 6 are shown. It is found that in the lowest part of the troposphere, ozone is totally depleted and about one day earlier than the ozone depletion found in the box model

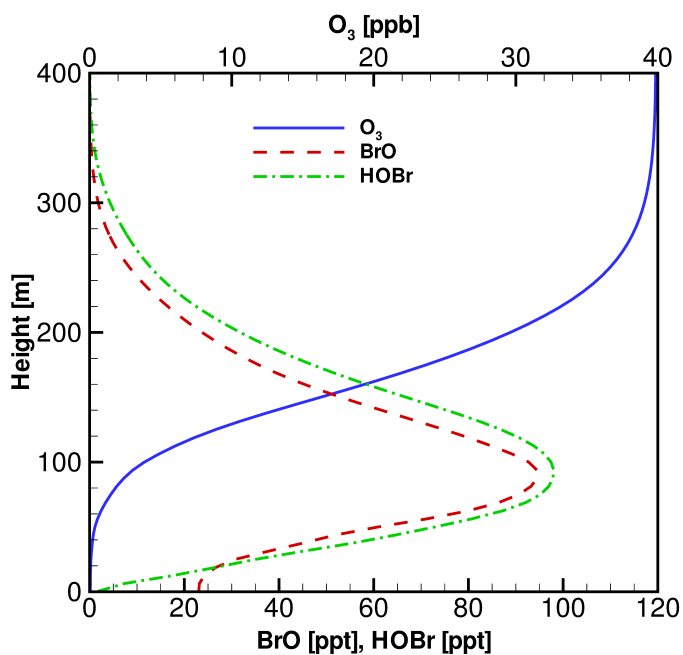


Figure 5.29: Vertical distribution of ozone, BrO and HOBr at day 6.

(see Fig. 5.1). In the 3D simulation, the peak values of the bromine species are found at the height of 90-100 m. The peak values of BrO and HOBr in the 3D simulation are 95 ppt and 100 ppt, respectively, which are larger than those found in the box model (60 ppt and 65 ppt for BrO and HOBr). The reason for the difference between the 3D simulation and the box model study can be explained as follows: the mixing intensity in 3D simulation is not as large as it is in the box model (where it is infinity), which affects the temporal and spatial change of chemical species concentrations. When the HOBr molecules in the lowest part of the troposphere are consumed by the heterogeneous liberation process at the bottom ice surface, Br₂ molecules are produced, leading to the enhancement of the bromine concentration in the air near the surface. Due to the limited turbulent mixing intensity in the 3D simulation, there occurs an accumulation of bromine in the regions near the bottom surface. This increase of surface bromine concentrations leads to a faster heterogeneous reaction rate and a speeding up of the ozone depletion. The reason for the relative higher peak values for the reactive bromine species may be also attributable to this accumulation effect of the chemical species near the surface. Moreover, the venting/mixing at the top of the boundary layer may also bring O₃ rich air from aloft into the boundary layer, resulting in a higher BrO concentration. Overall, the vertical distributions of the reactive bromine species depend on the balance between the turbulent mixing intensity, chemical production and consumption including the heterogeneous processes. Moreover, this balance is affected by

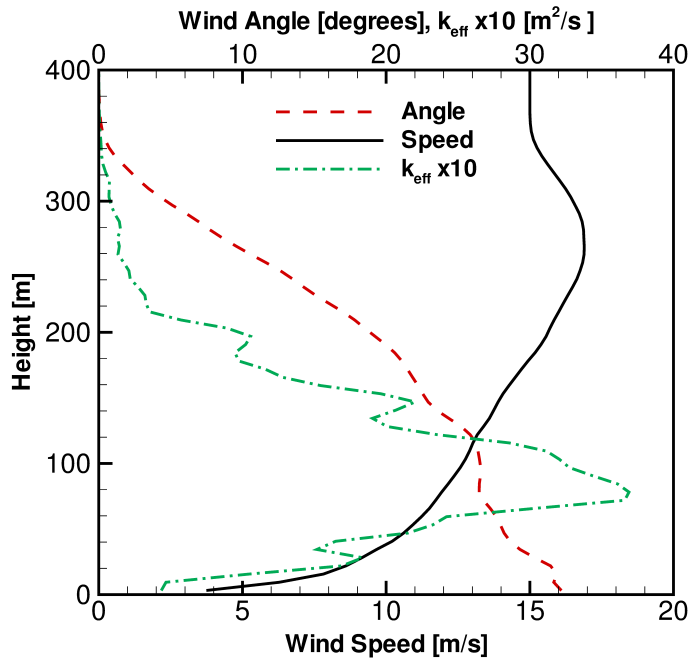


Figure 5.30: Vertical distributions of averaged wind profiles and effective turbulent diffusivity over the 9th hour when wind speed is 15 m/s [155].

many factors such as wind speed, temperature inversion intensity, surface topography. However, more parameter studies are needed to investigate this balance effect.

A preliminary parameter study is conducted for the influence of wind speed on the development of the boundary layer. In this parameter study, the wind speed is changed from 8 m/s to 15 m/s while other parameters in the simulation are fixed. The vertical distribution of wind speed, angle and effective turbulent diffusivity over the 9th hour is shown in Fig. 5.30. It can be seen that due to the increase of wind speed, the boundary layer elevates to a height of more than 300 m. The maximum value of wind speed is approximately 17 m/s occurring at about 280 m. It can be expected that the chemical mixing ratios are reduced because of the increase of the boundary layer height. Thus, the reaction rates for ozone depletion are retarded. However, from Fig. 5.30, it is also observed that the turbulent mixing intensity within the boundary layer is about five times of the value obtained in 8 m/s wind speed simulation. It represents an enhancement of the gas transfer between the ground surface and the boundary layer, which accelerates the ozone depletion. Thus, the change of the wind speed has both negative and positive impacts on the ozone depletion rate, which needs a more detailed evaluation in a future study.

5.2.2 Model with a Mountain

The bottom flat surface of the computational domain is then replaced with a complex shape representing the terrain of Melville Island in Canada. The data set for the mountain shape is provided by Dr. H. Sihler and Prof. U. Platt from the Institute of Environmental Physics of Heidelberg University. The 2-D view of the mountain is shown in Fig. 5.31. The horizontal size of the major part of mountain is longer than 150 km and top of the mountain is about 750 m, thus the computational domain should be re-sized compared with the flat surface simulation.

5.2.2.1 Initial Conditions

For this simulation, the major part of the Melville Island which ranges from -140 km to 60 km in x -direction and from -160 km to 40 km in y -direction is used. The data set for the mountain shape is first imported into the mesh generation software ICEM-CFD [176] as a cluster of scattered points. After combining all the points together, the shape of the bottom surface of the computational domain is obtained. By adding the top and lateral side boundaries, the complete computational domain can be formed. Then the grid nodes are distributed in the computational domain. Finally, the mesh file is generated and imported in the OpenFOAM solver.

Figure 5.32 shows the 3-D view of the computational domain used in the model.

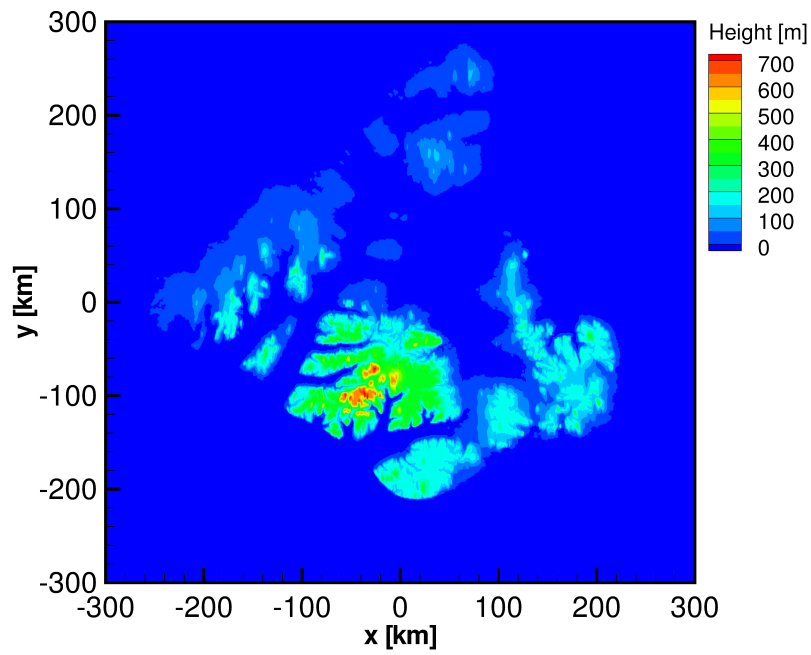


Figure 5.31: Melville Island in Canada [175].

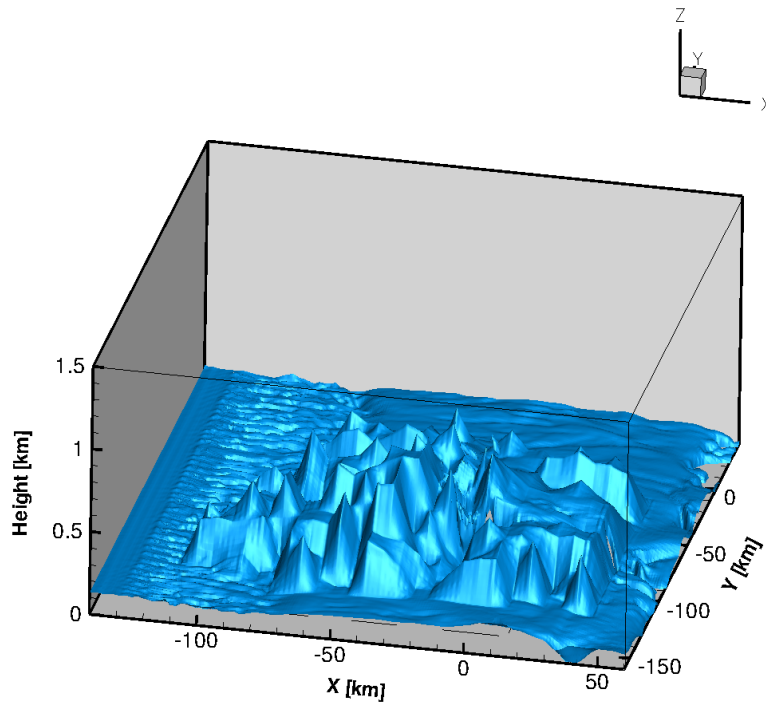


Figure 5.32: Three-dimensional view of the computational domain with the mountain topography surface [175].

The size of the domain is $200 \text{ km} \times 200 \text{ km} \times 1.5 \text{ km}$. For simplicity of the treatment of the boundary conditions, small islands near the lateral sides are replaced by the flat surface. 200 elements are distributed uniformly along each horizontal directions, which denotes 1 km horizontal grid resolution. Along the vertical direction, 15 elements are distributed. The thickness of each element depends on the height of the bottom surface. The initial wind speed is 0 m/s in the whole computational domain, the inlet wind speed at $x = -140 \text{ km}$ is 8 m/s along the x direction. The other initial settings are similar to the ones used in the simulation of the flat surface. It can be expected that as the wind flows across the mountain, because of the topography change of the surface, the movement of the air parcels in a large spatial scale affects the vertical mixing within the boundary layer, changing the local ozone depletion rate and the spatial distributions of the halogen species.

5.2.2.2 Boundary Conditions

The boundaries conditions for the simulation with a mountain shape boundary are similar to the ones of the flat surface simulation except the inlet and outlet boundary conditions are applied to the lateral sides boundaries. The following changes are described below.

At the inlet boundary, which is the plane at $x = -140 \text{ km}$, the flow has the velocity of (8 m/s, 0, 0). For the potential temperature, a 100 m well-mixed layer of 265 K from the bottom and an inverse temperature gradient of 0.01 K m^{-1} up to 1500 m height is assumed. The relation $p = p_0 - \rho g z$ is adopted for pressure. A two-step procedure is applied for the chemical species mixing ratios: first, a 3-D simulation with a flat bottom surface is performed using the initial species mixing ratios (see Tab. 5.2). After $t = 5.5$ days, the mixing ratios of the chemical species are averaged horizontally over each height level and used as the inlet condition for the chemical species mixing ratios at different heights. The inlet values of the principal chemical species are listed in Tab. 5.7.

At the outlet boundaries, i.e. the planes at $x = 60 \text{ km}$, $y = -160 \text{ km}$, and $y = 40 \text{ km}$,

Table 5.7: Inlet values of the principal chemical species, z denotes height [175].

Species	$z < 100 \text{ m}$	$100 \text{ m} < z < 200 \text{ m}$	$200 \text{ m} < z < 300 \text{ m}$	$z > 300 \text{ m}$
O ₃	31 ppb	35 ppb	39 ppb	40 ppb
BrO	65 ppt	30 ppt	5 ppt	0 ppt
HOBr	13 ppt	18 ppt	7 ppt	0 ppt
Br	2 ppt	1 ppt	0 ppt	0 ppt

Neumann (zero gradient) conditions are used for all the variables at these three lateral sides.

5.2.2.3 Results

The simulation is extended to include a bottom surface with a mountain shape as described above. The initial ozone-rich gas within the computational domain is not moving while the inlet wind flows along the x -direction. All the results are analyzed at the 9th hour. Figures 5.33 – 5.35 show the x -, y - and z -components of the wind speed after 9 hours at cross sections $y = -60$ km (Figs. 5.33 and 5.35) and $x = -40$ km (Fig. 5.34).

It can be observed that as the wind flows over the mountain, large scale turbulent mixing occurs above the mountain surface. In Fig. 5.33, an area with higher wind speed is found behind the main peak of the mountain. The reason may be attributed to the propagation of the initial pressure wave from the inlet boundary. Figure 5.34 shows that as the air flows across the mountain, it moves downhill in y -direction. Figure 5.35 reveals that some resolved scale turbulent fluctuations are found in front of or behind the peaks of the mountain. These turbulent fluctuations may help to mix the bromine flux released from the surface.

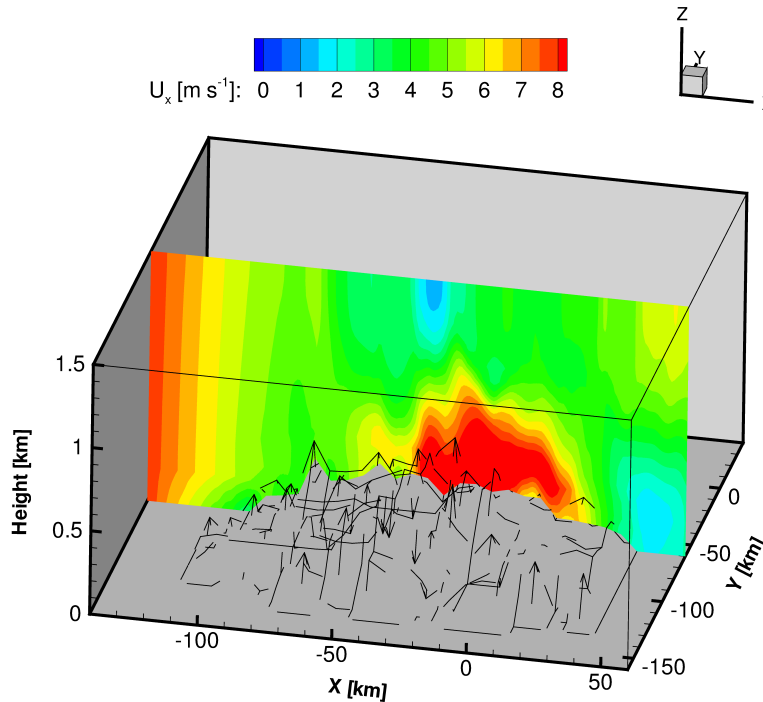


Figure 5.33: Instantaneous wind speed in x direction at the 9th hour at $y = -60$ km cut plane [175].

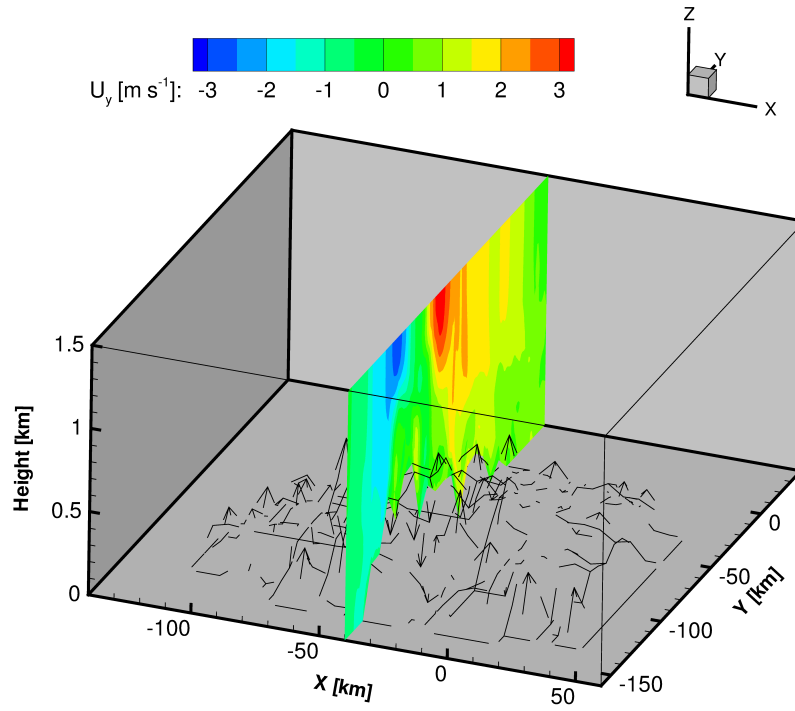


Figure 5.34: Instantaneous wind speed in y direction at the 9th hour at $x = -40$ km cut plane [175].

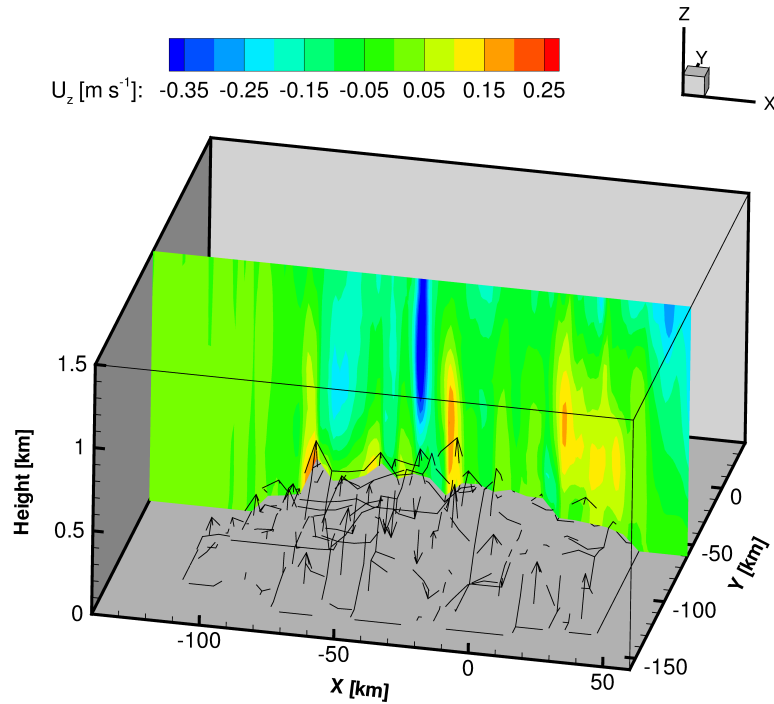


Figure 5.35: Instantaneous wind speed in z direction at the 9th hour at $y = -60$ km cut plane [175].

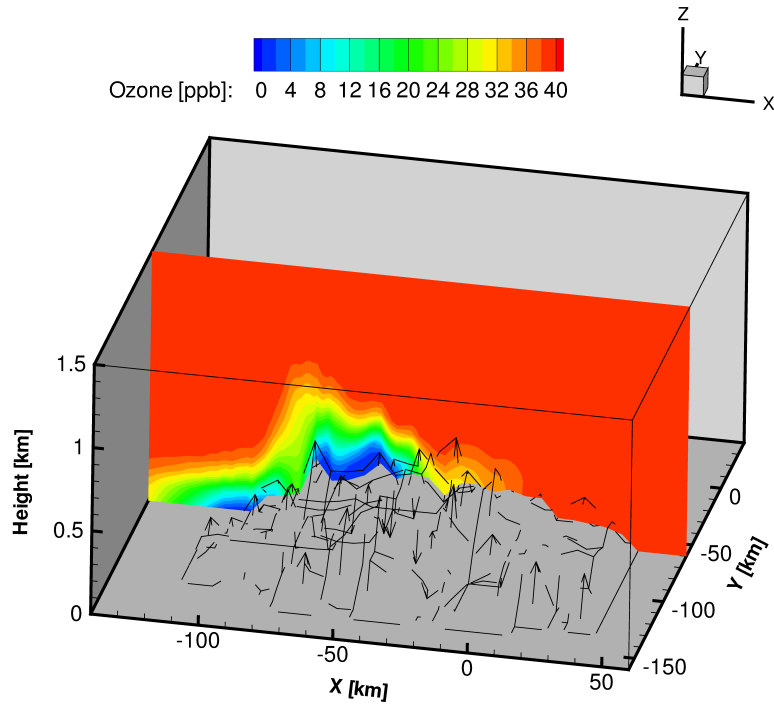


Figure 5.36: Distribution of the ozone concentration at the 9th hour at $y = -60$ km cut plane [175].

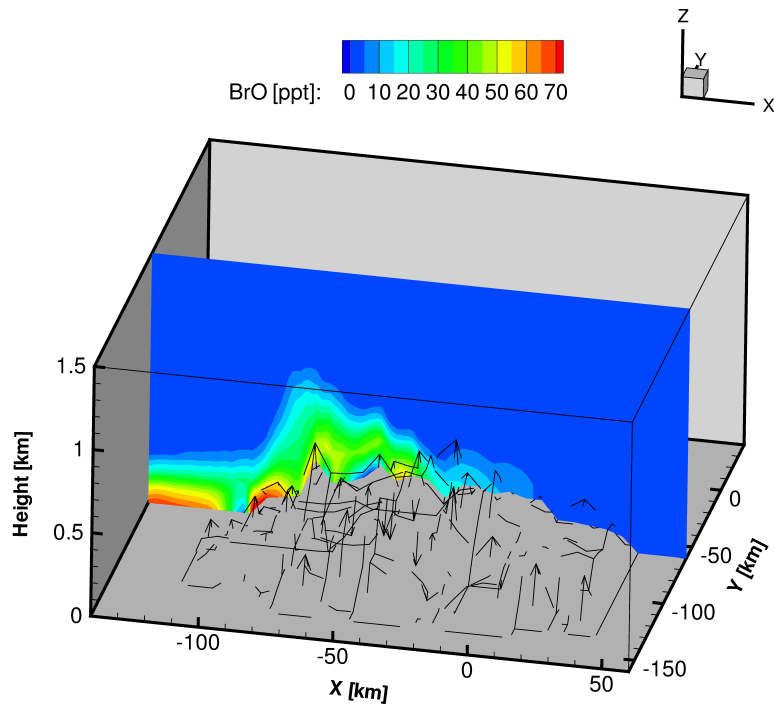


Figure 5.37: Distribution of the BrO concentration at the 9th hour at $y = -60$ km cut plane [175].

In Fig. 5.36, it is shown that as the inlet gas is transported to the mountain area, the ozone in the lowest part of the troposphere is almost totally consumed. An enhancement of the BrO is found in the same region, which can be seen in Fig. 5.37.

Figure 5.37 shows that the typical mixing ratio for BrO in the boundary layer is about 30–60 ppt, which is within a typical range found in the observations [42, 44, 45, 46, 47, 48, 51]. The present results indicate that the model is suitable to capture complex ground surfaces, and the skeletal chemical scheme allows for detailed studies of complex geometrical configurations that are found in polar regions. However, this simulation still needs validation, which is the major focus of future work.

6. Conclusions and Future Work

6.1 Conclusions

In this study, a numerical model is developed to simulate the spring time halogen release and ozone depletion in polar regions. The detailed chemical reaction mechanisms including heterogeneous reactions are investigated to study the role of the chemical species, and in particular, the reactive halogen species in the ozone depletion event.

In the box model study, when the nitrogen and chlorine containing species are not considered, i.e. in the bromine only mechanism, the temporal change of chemical species concentrations shows that ozone is completely destroyed after 5 days induction time and 40 hours depletion process assuming a boundary layer height of 200 m. When the boundary layer height increases, the whole depletion process is retarded, and the average principal bromine species mixing ratios are reduced. The importance of the bromine containing reactions on the ozone depletion rate is identified using a relative sensitivity analysis of the chemical reaction rates. It is shown that as the bromine loading in the air is heavily enhanced by the "bromine explosion" mechanism, the heterogeneous reactions related to HOBr play an important role. The physical properties such as the reactive surface area offered for the heterogeneous reactions, determine the heterogeneous reaction rate, thus, greatly affecting the ozone depletion rates. It is found that the shortest ozone depletion period caused by local chemistry ends after two days.

In the box model simulations including NO_x chemistry, the computational results show that the NO_x concentrations are controlled by different chemical cycles at different time periods. During the depletion process, the most dominant NO_x reaction cycle is related to BrONO₂ because of the enhanced bromine concentration in the air. The importance of this chemical cycle is identified by both the study of the reaction rate evolutions and relative sensitivities. A critical value of 0.0004 of the uptake coefficient of the BrONO₂ hydrolysis reaction at the aerosol and saline surfaces is identified, beyond which the existence of NO_x species accelerates the ozone depletion event, whereas for lower values, retardation occurs. In the simulation including the chlorine related mechanism, according to the calculated time integration of Br and Cl radicals, the number of Cl atoms during depletion is less than 0.1% of the atomic Br radicals. Therefore,

the chlorine containing species has minor direct effect on the ozone loss. A parameter study of the reaction rate ratio, $K_{\text{Br}_2/\text{BrCl}}$, for Br_2 and BrCl formation through reactions (R14) and (R129) reveals that the chemical composition of the surface has a strong impact on the ozone depletion rate.

A sensitivity analysis is performed for the detailed chemical reaction mechanism. Based on the results of the sensitivity analysis, 27 reactions and 4 species are removed from the detailed chemical reaction mechanism and a skeletal mechanism is derived with 26 species and 28 chemical reactions. This skeletal mechanism is adopted in the three-dimensional large eddy simulations with different shapes of the bottom boundary to account for the effect of the turbulent mixing and the topography change. In the 3D simulation with a flat ground surface, it is shown that the reactive bromine flux generated at the ice surface is mixed within the boundary layer. The strongest turbulent mixing is found at the height of about 35 m. Due to the limited turbulent mixing in the 3D simulation compared to the box model study, an accumulation of bromine concentration is found in the regions near the bottom surface, which causes the acceleration of the ozone depletion event and higher mixing ratios of the halogen species such as BrO and HOBr . When a boundary with a shape representing a mountain is applied, large scale fluctuations are observed near the mountain, which may enhance the turbulent mixing. The non-uniform vertical distribution of chemical species concentrations is captured, where the ozone is totally consumed and a strong elevation of the reactive bromine species occurs near the bottom surface.

Finally, the issues raised in Chapter 1 can be answered:

- **What are the sources of the halogens causing the ozone depletion?**

It is found that the sea ice covered by snow is the major source of the halogens, leading to the ozone depletion. Besides, the existence of the sea salt aerosols can enhance the re-activation processes of the inert halogen species through the heterogeneous reactions. The result indicates that when the boundary layer height is higher than 200 m, both the ice/snow surface and the aerosols are needed for the occurrence of the ozone depletion event (see the results shown in Fig. 5.4 and the related discussions).

- **What is the effect caused by the change of the weather conditions?**

In the simulations, it is observed that the increase of the boundary layer can cause the retardation of the ozone depletion and the lower mixing ratios of the halogen species. If the surface area provided by the ice/snow pack (the reactive surface ratio β) increases, the time needed for the ozone depletion is shortened, which is mainly attributable to the time decrease of the induction stage. Moreover, the increase of the wind speed leads to the elevation of the boundary layer height

and the enhancement of the turbulent mixing intensity, which may affect the time behavior of the ozone and the halogen species both positively and negatively.

- **What is the role for each reaction in the ozone depletion and halogen release mechanism?**

The relative importance of each reaction is identified by using a sensitivity analysis. It is found that the heterogeneous reactions related to HOBr are important during the ozone depletion event as they determine the total halogen loading in the atmosphere. When the bromine concentration increases, the chemical reaction cycle including the hydrolysis of BrONO₂ becomes more prominent. The reaction rates of the heterogeneous hydrolysis of BrONO₂ considerably influence the depletion of ozone, which is seen in Fig. 5.16.

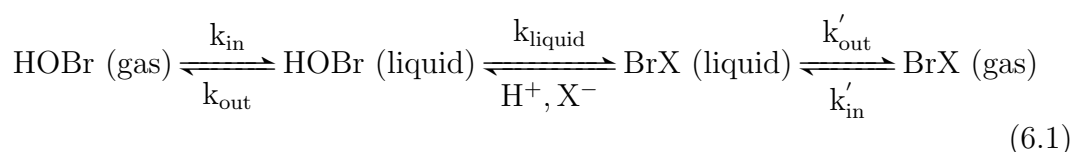
- **How to include the effect of the vertical turbulent mixing for the ozone depletion more accurately?**

The vertical turbulent mixing is included in the 3D large eddy simulation with the simplified Smagorinsky subgrid model. It is revealed that the limited intensity of the turbulent mixing in the 3D simulation reduces the time needed for the near-surface ozone to be totally consumed. Moreover, the turbulent mixing is affected by the topography change of the ground surface, leading to a non-uniform spatial distribution of the ozone and the halogen species.

6.2 Future Work

Both the box model and 3D model can be improved in many aspects.

- **Liquid reactions:** In the present model, it is assumed that the rates of liquid reactions are much faster than the adsorption process occurring at the aerosol or ice/snow pack surfaces. The heterogeneous reaction rates are calculated by using the rate of adsorption and neglecting the liquid reaction rates. However, it is possible to include the liquid reactions explicitly in the model. In that situation, the heterogeneous reaction $\text{HOBr} + \text{H}^+ + \text{X}^- \xrightarrow{\text{mp}} \text{BrX} + \text{H}_2\text{O}$ can be divided to three steps: adsorption of gas phase molecules at the surface, following liquid reactions and re-emission processes. These processes can be denoted by Eq. (6.1):



The adsorption rates of gas phase HOBr, k_{in} , by the aerosols and ice/snow have the same forms as the ones shown in Eqs. (3.3) and (3.7) in the current model.

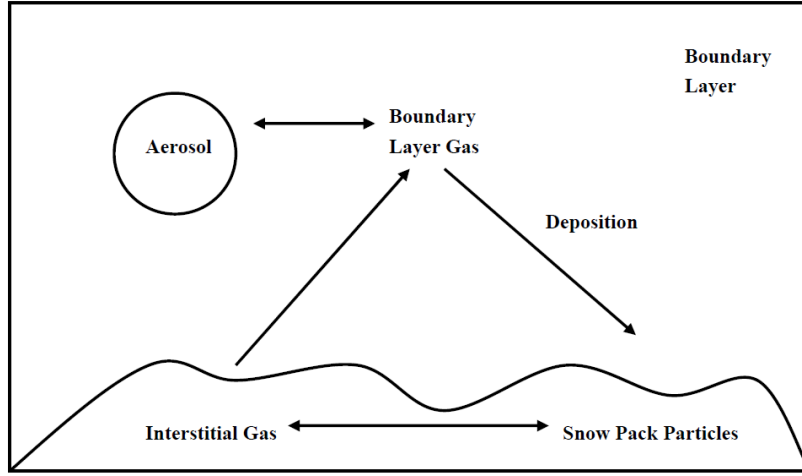


Figure 6.1: Gas transfer processes in the boundary layer.

The rate constants k_{liquid} for the liquid reactions can be looked up in Liu and Margerum [177]. For the gas transfer from the liquid phase to the gas phase, an chemical equilibrium between the gas phase and aerosol phase is assumed:

$$k_{\text{in}}[\text{HOBr (gas)}] = k_{\text{out}}[\text{HOBr (liquid)}]. \quad (6.2)$$

Thus, the re-emission rate constant k_{out} can be expressed as

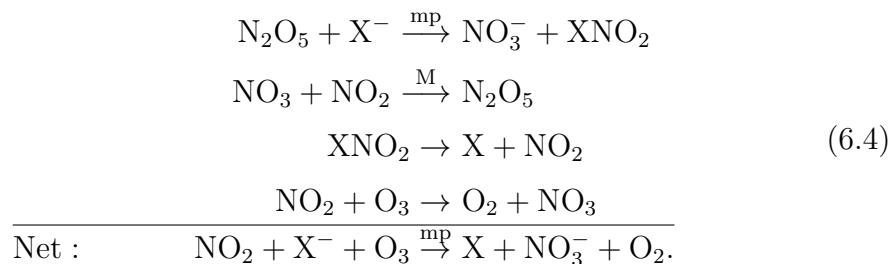
$$k_{\text{out}} = k_{\text{in}}/(HRT), \quad (6.3)$$

in which H is the Henry coefficient, R is the universal gas constant, and T is the absolute temperature.

In addition, the porous properties of the snow covering the ice surface can be taken into account. Figure 6.1 shows a sketch of the gas transfer processes in the boundary layer, especially within the snowpack at the bottom. It can be seen that the gas phase molecules first deposit at the surface of the snowpack, then undergo the liquid reactions in the snow particles. The products are then emitted to the interstitial gas within the snowpack. The estimation of the transfer rate between the interstitial gas and the boundary layer gas needs the consideration of the liquid content ratio in the snowpack.

- Effects of N_2O_5 : At present, the chemical species N_2O_5 and its related reactions are not considered in the chemical reaction mechanisms used in the model. This treatment is the same as the one used in Lehrer et al. [105]. However, the species

N_2O_5 can participate in an ozone depletion cycle which is listed below:



However, the rates of the heterogeneous reaction still need to be estimated.

- Different subgrid models: According to Beare et al. [126], change of the subgrid models can affect the estimation of the turbulent diffusion and the following model results. Therefore, in the future, the present Smagorinsky model could be replaced with other subgrid models. An example of the typical turbulent kinetic energy based subgrid model is the k -equation model, in which the evolution of the subgrid turbulent kinetic energy including transport and diffusion is expressed by Eq. (3.20). Moreover, the back-scatter effects [139] which denote the turbulent energy transfered from the filtered scale back to the resolved scale can be also considered.
- Different weather conditions: Changing parameters such as the effect of wind speed, ice surface coverage, and temperature inversion is beneficial to study the ozone depletion under different weather conditions. For instance, when the wind speed increases, reaching a stormy condition, it can be expected that massive snow particles may be pumped from the snow pack on the ice by the strong wind and then lifted and distributed into the boundary layer. As a result, in the lowest part of the troposphere, the effective snow surface area A_{eff} is enlarged, thus accelerating the heterogeneous reaction rate and ozone depletion rate. Besides, the aerodynamic resistance which represents the resistance of gas transport in the surface layer is smaller in a strong wind condition. This reduction of the aerodynamic resistance may enhance the gas transfer between the ground surface and the boundary layer, speeding up the ozone depletion. However, the increase of wind speed also leads to the increase of the boundary layer height, which leads the decrease of the chemical mixing ratios and the reaction rates. In addition, strong wind is also the major cause for the breakup of the boundary layer, leading to the entrainment of the ozone rich air into the boundary layer and termination of the ozone depletion. Thus, simulations with different values of the wind speed are desirable for clarify the impact of wind speed on the ozone depletion rate.

By modifying the air composition and the chemical reactions included in the mechanism, it is also possible to extend the model to consider other types of air,

for instance the air in the Arctic polluted by the anthropogenic activities and long-range transport from the places at low latitudes. The surface properties of the polar regions are rather complicated due to the existence of the mountains and open leads. The implementation of these different surface properties can be done by changing the surface roughness, halogen emission and deposition fluxes.

Appendix

A. Nomenclature

Symbol	Unit	Description
A_{aerosol}	m^2	Aerosol surface area
a	m	Typical aerosol radius
a_1, a_2, \dots, a_7		Polynomial constants for thermodynamic properties
C_p	$\text{kg m}^2 \text{s}^{-2} \text{mol}^{-1} \text{K}^{-1}$	Specific heat capacity
c	mol m^{-3}	Species concentrations
c_e		Constant in the sub-grid model
c_k		Constant in the sub-grid model
c_s		Constant in the sub-grid model
D_{eff}	$\text{m}^2 \text{s}^{-1}$	Effective species diffusion coefficient
D_g	$\text{m}^2 \text{s}^{-1}$	Gas phase molecular diffusivity
$D_{i,\text{eff}}$	$\text{m}^2 \text{s}^{-1}$	Effective diffusivity of the i^{th} species
D_{liq}	$\text{m}^2 \text{s}^{-1}$	Liquid phase molecular diffusivity
d_{eff}	m^{-1}	Surface-volume ratio coefficient
E	s^{-1}	Characteristic filtered rate of strain
$\bar{\bar{e}}$	s^{-1}	Rate of strain tensor
$\bar{\bar{e}}^D$	s^{-1}	Deviatoric part of the rate of strain tensor
$F(U_z)$	$\text{m}^{-1} \text{s}$	probability density function of the vertical velocity
\vec{g}	m s^{-2}	Gravitational acceleration
H	$\text{mol L}^{-1} \text{atm}^{-1}$	Henry constant
H	$\text{kg m}^2 \text{s}^{-2} \text{mol}^{-1}$	Enthalpy
H^*	$\text{mol L}^{-1} \text{atm}^{-1}$	Effective Henry constant
h_s	$\text{m}^2 \text{s}^{-2}$	Specific sensible enthalpy
$\bar{\bar{I}}$		Unit dyadic
J	s^{-1}	Photolysis reaction rates
$K_{\text{Br}_2/\text{BrCl}}$		Production ratio of Br_2 and BrCl from the snow/ice surface
k	$(\text{molec. cm}^{-3})^{1-n} \text{s}^{-1}$	Reaction rate constant, n is the reaction order
k_{eff}	$\text{m}^2 \text{s}^{-1}$	Effective turbulent diffusivity
k_t	$\text{m}^2 \text{s}^{-1}$	Sub-grid turbulent kinetic energy
Le		Lewis number

L_{mix}	m	Boundary layer height
M_{HOBr}	kg mol ⁻¹	Molar mass of HOBr
P_i	kg m ⁻¹ s ⁻²	Partial pressure of the i^{th} species
p	kg m ⁻¹ s ⁻²	Pressure
\bar{p}	kg m ⁻¹ s ⁻²	Modified pressure
p_{rgh}	kg m ⁻¹ s ⁻²	Pressure excluding the term $\rho g z$
Pr_l		Laminar Prandtl number
Pr_t		Turbulent Prandtl number
r_a	m ⁻¹ s	Aerodynamic resistance
r_b	m ⁻¹ s	Quasi-laminar layer resistance
r_c	m ⁻¹ s	Surface resistance
S	kg m ² s ⁻² mol ⁻¹ K ⁻¹	Entropy
S_{ij}		Relative sensitivity of the i^{th} concentration caused by the j^{th} reaction rate change
T	K	Temperature
t	s	Time
\vec{U}	m s ⁻¹	Gas velocity vector
U_x	m s ⁻¹	Velocity component along x direction
U_y	m s ⁻¹	Velocity component along y direction
U_z	m s ⁻¹	Velocity component along z direction
$U(z_1)$	m s ⁻¹	Horizontal averaged velocity at the height z_1
u_*	m s ⁻¹	Friction velocity
V_m	m ³	Total volume of the model
v_d	m s ⁻¹	Deposition velocity
v_{therm}	m s ⁻¹	Molecular mean speed
W	m s ⁻¹	Wind speed
Y_i		Mass fraction of the i^{th} species
z	m	Height
z_0	m	Surface roughness
z_1	m	Half of the height at the first vertical grid
z_s	m	Surface layer height, 10% of the boundary layer
α		Accommodation coefficient
α_{eff}	m ² s ⁻¹	Effective thermal diffusivity
β		Reactive surface ratio
β_h		Constant in Monin-Obukhov similarity
β_m		Constant in Monin-Obukhov similarity

γ		Uptake coefficient
Δ	m	Filter width
$\Delta h_{f,i}^\circ$	$\text{m}^2 \text{s}^{-2}$	Specific enthalpy of formation
δ_z	m	Height at the first vertical grid
$\Theta(z_1)$	K	Horizontal averaged potential at the height z_1
θ	K	Potential temperature
θ_w	K	Surface potential temperature
κ		Von Karman's constant
μ_{eff}	$\text{kg m}^{-1} \text{s}^{-1}$	Effective dynamic viscosity
μ_l	$\text{kg m}^{-1} \text{s}^{-1}$	Molecular dynamic viscosity
μ_t	$\text{kg m}^{-1} \text{s}^{-1}$	Sub-grid turbulent dynamic viscosity
$\vec{\Omega}$	s^{-1}	Angular velocity vector of the earth's rotation
ω	s^{-1}	Magnitude of the angular velocity
$\dot{\omega}_i$	$\text{kg m}^{-3} \text{s}^{-1}$	Reaction rate of the i^{th} species
ϕ	$^\circ$	Latitude
ρ	kg m^{-3}	Air density
$\bar{\tau}$	$\text{kg m}^{-1} \text{s}^{-2}$	Molecular viscous stress tensor
$\overline{\overline{\tau}}_t$	$\text{kg m}^{-1} \text{s}^{-2}$	Sub-grid stress tensor
$\overline{\overline{\tau}}_t^D$	$\text{kg m}^{-1} \text{s}^{-2}$	Deviatoric part of the sub-grid stress tensor

Physical Constants

Symbol	Quantity
$R = 8.31451 \text{ kg m}^2 / (\text{s}^2 \text{ mol K})$	Universal gas constant
$g = 9.81 \text{ m/s}^2$	Gravitational acceleration

B. Chemical Reaction Mechanism for Ozone Depletion and Halogen Release

Mechanism for bromine containing species:

Reac. No.	Reaction	k [(molec. cm ⁻³) ¹⁻ⁿ s ⁻¹]	Reac. order	Reference
R1	$O_3 + h\nu \rightarrow O(^1D) + O_2$	$4.70 \cdot 10^{-7}$	1	Lehrer et al. [105]
R2	$O(^1D) + O_2 \rightarrow O_3$	$4.20 \cdot 10^{-11}$	2	Atkinson et al. [168]
R3	$O(^1D) + H_2O \rightarrow 2OH$	$2.30 \cdot 10^{-10}$	2	Atkinson et al. [168]
R4	$Br + O_3 \rightarrow BrO + O_2$	$7.65 \cdot 10^{-13}$	2	Atkinson et al. [168]
R5	$Br_2 + h\nu \rightarrow 2Br$	0.021	1	Lehrer et al. [105]
R6	$BrO + h\nu \xrightarrow{O_2} Br + O_3$	0.014	1	Lehrer et al. [105]
R7	$BrO + BrO \rightarrow 2Br + O_2$	$1.92 \cdot 10^{-12}$	2	Atkinson et al. [168]
R8	$BrO + BrO \rightarrow Br_2 + O_2$	$5.42 \cdot 10^{-13}$	2	Atkinson et al. [168]
R9	$BrO + HO_2 \rightarrow HOBr + O_2$	$4.31 \cdot 10^{-11}$	2	Atkinson et al. [168]
R10	$HOBr + h\nu \rightarrow Br + OH$	$3.00 \cdot 10^{-4}$	1	Lehrer et al. [105]
R11	$CO + OH(+M) \xrightarrow{O_2} HO_2 + CO_2(+M)$	$2.40 \cdot 10^{-13}$	2	Atkinson et al. [168]
R12	$Br + HO_2 \rightarrow HBr + O_2$	$1.42 \cdot 10^{-12}$	2	Atkinson et al. [168]
R13	$HOBr + HBr \xrightarrow{aerosol} Br_2 + H_2O$	See text		
R14	$HOBr + H^+ + Br^- \xrightarrow{snow/ice} Br_2 + H_2O$	See text		
R15	$Br + HCHO \xrightarrow{O_2} HBr + CO + HO_2$	$7.65 \cdot 10^{-13}$	2	Atkinson et al. [168]
R16	$Br + CH_3CHO \xrightarrow{O_2} HBr + CH_3CO_3$	$3.22 \cdot 10^{-12}$	2	Atkinson et al. [168]
R17	$Br_2 + OH \rightarrow HOBr + Br$	$5.66 \cdot 10^{-11}$	2	Atkinson et al. [168]
R18	$HBr + OH \rightarrow H_2O + Br$	$1.23 \cdot 10^{-11}$	2	Atkinson et al. [168]
R19	$Br + C_2H_2 \xrightarrow{3O_2} 2CO + 2HO_2 + Br$	$4.20 \cdot 10^{-14}$	2	Borken [169]
R20	$Br + C_2H_2 \xrightarrow{2O_2} 2CO + HO_2 + HBr$	$8.92 \cdot 10^{-14}$	2	Borken [169]
R21	$Br + C_2H_4 \xrightarrow{3.5O_2} 2CO + 2HO_2 + Br + H_2O$	$2.53 \cdot 10^{-13}$	2	Barnes et al. [170]
R22	$Br + C_2H_4 \xrightarrow{2.5O_2} 2CO + HO_2 + HBr + H_2O$	$5.34 \cdot 10^{-13}$	2	Barnes et al. [170]
R23	$CH_4 + OH \xrightarrow{O_2} CH_3O_2 + H_2O$	$2.46 \cdot 10^{-15}$	2	Atkinson et al. [168]
R24	$BrO + CH_3O_2 \rightarrow Br + HCHO + HO_2$	$1.60 \cdot 10^{-12}$	2	Aranda et al. [171]
R25	$BrO + CH_3O_2 \rightarrow HOBr + HCHO + 0.5O_2$	$4.10 \cdot 10^{-12}$	2	Aranda et al. [171]
R26	$OH + O_3 \rightarrow HO_2 + O_2$	$3.94 \cdot 10^{-14}$	2	Atkinson et al. [168]
R27	$OH + HO_2 \rightarrow H_2O + O_2$	$1.26 \cdot 10^{-10}$	2	Atkinson et al. [168]
R28	$OH + H_2O_2 \rightarrow HO_2 + H_2O$	$1.56 \cdot 10^{-12}$	2	Atkinson et al. [168]
R29	$OH + OH \xrightarrow{O_2} H_2O + O_3$	$2.12 \cdot 10^{-12}$	2	Atkinson et al. [168]
R30	$HO_2 + O_3 \rightarrow OH + 2O_2$	$1.37 \cdot 10^{-15}$	2	Atkinson et al. [168]

B-2 B. Chemical Reaction Mechanism for Ozone Depletion and Halogen Release

Mechanism for bromine containing species (continued):

Reac. No.	Reaction	k [(molec. cm ⁻³) ¹⁻ⁿ s ⁻¹]	Reac. order	Reference
R31	$\text{HO}_2 + \text{HO}_2 \rightarrow \text{O}_2 + \text{H}_2\text{O}_2$	$4.65 \cdot 10^{-12}$	2	Atkinson et al. [168]
R32	$\text{C}_2\text{H}_6 + \text{OH} \rightarrow \text{C}_2\text{H}_5 + \text{H}_2\text{O}$	$1.46 \cdot 10^{-13}$	2	Atkinson et al. [168]
R33	$\text{C}_2\text{H}_5 + \text{O}_2 \rightarrow \text{C}_2\text{H}_4 + \text{HO}_2$	$3.80 \cdot 10^{-15}$	2	Atkinson et al. [168]
R34	$\text{C}_2\text{H}_5 + \text{O}_2(+\text{M}) \rightarrow \text{C}_2\text{H}_5\text{O}_2(+\text{M})$	$7.12 \cdot 10^{-12}$	2	Atkinson et al. [168]
R35	$\text{C}_2\text{H}_4 + \text{OH}(+\text{M}) \xrightarrow{1.5\text{O}_2} \text{CH}_3\text{O}_2 + \text{CO} + \text{H}_2\text{O}(+\text{M})$	$8.20 \cdot 10^{-12}$	2	Atkinson et al. [168]
R36	$\text{C}_2\text{H}_4 + \text{O}_3 \rightarrow \text{HCHO} + \text{CO} + \text{H}_2\text{O}$	$4.33 \cdot 10^{-19}$	2	Sander et al. [98]
R37	$\text{C}_2\text{H}_2 + \text{OH}(+\text{M}) \xrightarrow{1.5\text{O}_2} \text{HCHO} + \text{CO} + \text{HO}_2(+\text{M})$	$7.50 \cdot 10^{-13}$	2	Atkinson et al. [168]
R38	$\text{C}_3\text{H}_8 + \text{OH} \xrightarrow{2\text{O}_3} \text{C}_2\text{H}_5\text{O}_2 + \text{CO} + 2\text{H}_2\text{O}$	$8.13 \cdot 10^{-13}$	2	Atkinson et al. [168]
R39	$\text{HCHO} + \text{OH} \xrightarrow{\text{O}_2} \text{CO} + \text{H}_2\text{O} + \text{HO}_2$	$9.29 \cdot 10^{-12}$	2	Atkinson et al. [168]
R40	$\text{CH}_3\text{CHO} + \text{OH} \xrightarrow{\text{O}_2} \text{CH}_3\text{CO}_3 + \text{H}_2\text{O}$	$1.86 \cdot 10^{-11}$	2	Atkinson et al. [168]
R41	$\text{CH}_3\text{O}_2 + \text{HO}_2 \rightarrow \text{CH}_3\text{O}_2\text{H} + \text{O}_2$	$7.81 \cdot 10^{-12}$	2	Atkinson et al. [168]
R42	$\text{CH}_3\text{OOH} + \text{OH} \rightarrow \text{CH}_3\text{O}_2 + \text{H}_2\text{O}$	$3.97 \cdot 10^{-12}$	2	Atkinson et al. [168]
R43	$\text{CH}_3\text{OOH} + \text{OH} \rightarrow \text{HCHO} + \text{OH} + \text{H}_2\text{O}$	$2.09 \cdot 10^{-12}$	2	Atkinson et al. [168]
R44	$\text{CH}_3\text{OOH} + \text{Br} \rightarrow \text{CH}_3\text{O}_2 + \text{HBr}$	$5.19 \cdot 10^{-15}$	2	Atkinson et al. [168]
R45	$\text{CH}_3\text{O}_2 + \text{CH}_3\text{O}_2 \rightarrow \text{CH}_3\text{OH} + \text{HCHO} + \text{O}_2$	$3.06 \cdot 10^{-13}$	2	Atkinson et al. [168]
R46	$\text{CH}_3\text{O}_2 + \text{CH}_3\text{O}_2 \xrightarrow{\text{O}_2} 2\text{HCHO} + 2\text{HO}_2$	$1.50 \cdot 10^{-13}$	2	Atkinson et al. [168]
R47	$\text{CH}_3\text{OH} + \text{OH} \xrightarrow{\text{O}_2} \text{HCHO} + \text{HO}_2 + \text{H}_2\text{O}$	$7.68 \cdot 10^{-13}$	2	Atkinson et al. [168]
R48	$\text{C}_2\text{H}_5\text{O}_2 + \text{C}_2\text{H}_5\text{O}_2 \rightarrow \text{C}_2\text{H}_5\text{O} + \text{C}_2\text{H}_5\text{O} + \text{O}_2$	$6.80 \cdot 10^{-14}$	2	Atkinson et al. [168]
R49	$\text{C}_2\text{H}_5\text{O} + \text{O}_2 \rightarrow \text{CH}_3\text{CHO} + \text{HO}_2$	$7.44 \cdot 10^{-15}$	2	Sander et al. [98]
R50	$\text{C}_2\text{H}_5\text{O} + \text{O}_2 \rightarrow \text{CH}_3\text{O}_2 + \text{HCHO}$	$7.51 \cdot 10^{-17}$	2	Sander et al. [98]
R51	$\text{C}_2\text{H}_5\text{O}_2 + \text{HO}_2 \rightarrow \text{C}_2\text{H}_5\text{OOH} + \text{O}_2$	$1.31 \cdot 10^{-11}$	2	Atkinson et al. [168]
R52	$\text{C}_2\text{H}_5\text{OOH} + \text{OH} \rightarrow \text{C}_2\text{H}_5\text{O}_2 + \text{H}_2\text{O}$	$8.21 \cdot 10^{-12}$	2	Sander et al. [98]
R53	$\text{C}_2\text{H}_5\text{OOH} + \text{Br} \rightarrow \text{C}_2\text{H}_5\text{O}_2 + \text{HBr}$	$5.19 \cdot 10^{-15}$	2	Sander et al. [98]
R54	$\text{OH} + \text{OH}(+\text{M}) \rightarrow \text{H}_2\text{O}_2(+\text{M})$	$5.21 \cdot 10^{-12}$	2	Atkinson et al. [168]
R55	$\text{H}_2\text{O}_2 + h\nu \rightarrow 2\text{OH}$	$2.00 \cdot 10^{-6}$	1	Lehrer et al. [105]

Mechanism for nitrogen containing species:

Reac. No.	Reaction	k [(molec. cm ⁻³) ¹⁻ⁿ s ⁻¹]	Reac. order	Reference
R56	$\text{NO} + \text{O}_3 \rightarrow \text{NO}_2 + \text{O}_2$	$8.89 \cdot 10^{-15}$	2	Atkinson et al. [168]
R57	$\text{NO} + \text{HO}_2 \rightarrow \text{NO}_2 + \text{OH}$	$9.38 \cdot 10^{-12}$	2	Atkinson et al. [168]
R58	$\text{NO}_2 + \text{O}_3 \rightarrow \text{NO}_3 + \text{O}_2$	$9.02 \cdot 10^{-18}$	2	Atkinson et al. [168]
R59	$\text{NO}_2 + \text{OH}(+\text{M}) \rightarrow \text{HNO}_3(+\text{M})$	$1.62 \cdot 10^{-11}$	2	Atkinson et al. [168]
R60	$\text{NO} + \text{NO}_3 \rightarrow 2\text{NO}_2$	$2.76 \cdot 10^{-11}$	2	Atkinson et al. [168]
R61	$\text{HONO} + \text{OH} \rightarrow \text{NO}_2 + \text{H}_2\text{O}$	$7.40 \cdot 10^{-12}$	2	Atkinson et al. [168]
R62	$\text{HO}_2 + \text{NO}_2(+\text{M}) \rightarrow \text{HNO}_4(+\text{M})$	$1.61 \cdot 10^{-12}$	2	Atkinson et al. [168]
R63	$\text{HNO}_4(+\text{M}) \rightarrow \text{NO}_2 + \text{HO}_2(+\text{M})$	$4.02 \cdot 10^{-4}$	1	Atkinson et al. [168]
R64	$\text{HNO}_4 + \text{OH} \rightarrow \text{NO}_2 + \text{H}_2\text{O} + \text{O}_2$	$6.05 \cdot 10^{-12}$	2	Atkinson et al. [168]
R65	$\text{NO} + \text{OH}(+\text{M}) \rightarrow \text{HONO}(+\text{M})$	$1.36 \cdot 10^{-11}$	2	Atkinson et al. [168]
R66	$\text{OH} + \text{NO}_3 \rightarrow \text{NO}_2 + \text{HO}_2$	$2.00 \cdot 10^{-11}$	2	Atkinson et al. [168]
R67	$\text{HNO}_3 + h\nu \xrightarrow{\text{O}_2} \text{NO}_2 + \text{OH}$	$4.40 \cdot 10^{-8}$	1	Lehrer et al. [105]
R68	$\text{NO}_2 + h\nu \xrightarrow{\text{O}_2} \text{NO} + \text{O}_3$	$3.50 \cdot 10^{-3}$	1	Lehrer et al. [105]
R69	$\text{NO}_3 + h\nu \xrightarrow{\text{O}_2} \text{NO}_2 + \text{O}_3$	$1.40 \cdot 10^{-1}$	1	Lehrer et al. [105]
R70	$\text{NO}_3 + h\nu \rightarrow \text{NO} + \text{O}_2$	$1.70 \cdot 10^{-2}$	1	Lehrer et al. [105]
R71	$\text{NO} + \text{CH}_3\text{O}_2 \xrightarrow{\text{O}_2} \text{HCHO} + \text{HO}_2 + \text{NO}_2$	$8.44 \cdot 10^{-12}$	2	Atkinson et al. [168]
R72	$\text{NO}_3 + \text{CH}_3\text{OH} \xrightarrow{\text{O}_2} \text{HCHO} + \text{HO}_2 + \text{HNO}_3$	$6.38 \cdot 10^{-17}$	2	Atkinson et al. [168]
R73	$\text{NO}_3 + \text{HCHO} \xrightarrow{\text{O}_2} \text{CO} + \text{HO}_2 + \text{HNO}_3$	$5.80 \cdot 10^{-16}$	2	Atkinson et al. [168]
R74	$\text{NO} + \text{C}_2\text{H}_5\text{O}_2 \xrightarrow{\text{O}_2} \text{CH}_3\text{CHO} + \text{NO}_2 + \text{HO}_2$	$8.70 \cdot 10^{-12}$	2	Atkinson et al. [168]
R75	$\text{NO} + \text{CH}_3\text{CO}_3 \xrightarrow{\text{O}_2} \text{CH}_3\text{O}_2 + \text{NO}_2 + \text{CO}_2$	$2.00 \cdot 10^{-11}$	2	Atkinson et al. [168]
R76	$\text{NO}_2 + \text{CH}_3\text{CO}_3(+\text{M}) \rightarrow \text{PAN}(+\text{M})$	$1.33 \cdot 10^{-12}$	2	Atkinson et al. [168]
R77	$\text{Br} + \text{NO}_2(+\text{M}) \rightarrow \text{BrNO}_2(+\text{M})$	$5.03 \cdot 10^{-12}$	2	Atkinson et al. [168]
R78	$\text{Br} + \text{NO}_3(+\text{M}) \rightarrow \text{BrO} + \text{NO}_2(+\text{M})$	$1.60 \cdot 10^{-11}$	2	Atkinson et al. [168]
R79	$\text{BrO} + \text{NO}_2(+\text{M}) \rightarrow \text{BrONO}_2(+\text{M})$	$3.89 \cdot 10^{-12}$	2	Atkinson et al. [168]
R80	$\text{BrO} + \text{NO} \rightarrow \text{Br} + \text{NO}_2$	$2.38 \cdot 10^{-11}$	2	Atkinson et al. [168]
R81	$\text{BrONO}_2 + h\nu \rightarrow \text{NO}_2 + \text{BrO}$	$3.40 \cdot 10^{-4}$	1	Lehrer et al. [105]
R82	$\text{BrNO}_2 + h\nu \rightarrow \text{NO}_2 + \text{Br}$	$9.30 \cdot 10^{-5}$	1	Lehrer et al. [105]
R83	$\text{BrONO}_2 + \text{H}_2\text{O} \xrightarrow{\text{aerosol}} \text{HOBr} + \text{HNO}_3$	See text		
R84	$\text{PAN} + h\nu \rightarrow \text{NO}_2 + \text{CH}_3\text{CO}_3$	$3.03 \cdot 10^{-7}$	1	DeMore et al. [178]
R85	$\text{HNO}_3 + h\nu \xrightarrow{\text{aerosol}} \text{OH} + \text{NO}_2$	See text		
R86	$\text{BrONO}_2 + \text{H}_2\text{O} \xrightarrow{\text{ice/snow}} \text{HOBr} + \text{HNO}_3$	See text		

B-4 B. Chemical Reaction Mechanism for Ozone Depletion and Halogen Release

Mechanism for chlorine containing species:

Reac. No.	Reaction	k [(molec. cm ⁻³) ¹⁻ⁿ s ⁻¹]	Reac. order	Reference
R87	CH ₃ OOH + Cl → CH ₃ O ₂ + HCl	5.70 10 ⁻¹¹	2	Atkinson et al. [168]
R88	C ₂ H ₅ O ₂ H + Cl → C ₂ H ₅ O ₂ + HCl	5.70 10 ⁻¹¹	2	Sander et al. [98]
R89	HO ₂ + Cl → O ₂ + HCl	3.48 10 ⁻¹¹	2	Atkinson et al. [168]
R90	HO ₂ + Cl → OH + ClO	7.17 10 ⁻¹²	2	Atkinson et al. [168]
R91	H ₂ O ₂ + Cl → HO ₂ + HCl	2.46 10 ⁻¹³	2	Atkinson et al. [168]
R92	O ₃ + Cl → O ₂ + ClO	1.06 10 ⁻¹¹	2	Atkinson et al. [168]
R93	CH ₄ + Cl $\xrightarrow{O_2}$ CH ₃ O ₂ + HCl	5.13 10 ⁻¹⁴	2	Atkinson et al. [168]
R94	C ₂ H ₂ + Cl $\xrightarrow{3O_3}$ 2CO + 2HO ₂ + Cl	2.00 10 ⁻¹¹	2	Borken [169]
R95	C ₂ H ₂ + Cl $\xrightarrow{2O_3}$ 2CO + HO ₂ + HCl	4.24 10 ⁻¹¹	2	Borken [169]
R96	C ₂ H ₄ + Cl $\xrightarrow{3.5O_2}$ 2CO + 2HO ₂ + Cl + H ₂ O	3.92 10 ⁻¹¹	2	Atkinson et al. [168]
R97	C ₂ H ₄ + Cl $\xrightarrow{2.5O_2}$ 2CO + HO ₂ + HCl + H ₂ O	8.32 10 ⁻¹¹	2	Atkinson et al. [168]
R98	C ₂ H ₆ + Cl → C ₂ H ₅ + HCl	5.60 10 ⁻¹¹	2	Atkinson et al. [168]
R99	C ₃ H ₈ + Cl $\xrightarrow{2.5O_2}$ C ₂ H ₅ O ₂ + CO ₂ + HCl + H ₂ O	1.40 10 ⁻¹⁰	2	Atkinson et al. [168]
R100	HCHO + Cl $\xrightarrow{O_2}$ CO + HCl + HO ₂	7.19 10 ⁻¹¹	2	Atkinson et al. [168]
R101	CH ₃ CHO + Cl $\xrightarrow{O_2}$ HCl + CH ₃ CO ₃	7.20 10 ⁻¹¹	2	Atkinson et al. [168]
R102	OH + Cl ₂ → Cl + HOCl	4.28 10 ⁻¹⁴	2	Atkinson et al. [168]
R103	OH + HCl → Cl + H ₂ O	6.68 10 ⁻¹³	2	Atkinson et al. [168]
R104	OH + HOCl → ClO + H ₂ O	4.32 10 ⁻¹³	2	Atkinson et al. [168]
R105	OH + ClO → Cl + HO ₂	1.72 10 ⁻¹¹	2	Atkinson et al. [168]
R106	OH + ClO → HCl + O ₂	3.50 10 ⁻¹³	2	Atkinson et al. [168]
R107	ClO + ClO → Cl ₂ + O ₂	2.11 10 ⁻¹⁵	2	Atkinson et al. [168]
R108	ClO + ClO → 2Cl + O ₂	2.25 10 ⁻¹⁵	2	Atkinson et al. [168]
R109	ClO + ClO → Cl + OClO	1.73 10 ⁻¹⁵	2	Atkinson et al. [168]
R110	ClO + ClO(+M) → Cl ₂ O ₂ (+M)	4.42 10 ⁻¹³	2	Atkinson et al. [168]
R111	Cl ₂ O ₂ (+M) → ClO + ClO(+M)	4.81 10 ⁻¹	1	Atkinson et al. [168]
R112	ClO + HO ₂ → HOCl + O ₂	7.21 10 ⁻¹²	2	Atkinson et al. [168]
R113	ClO + CH ₃ O ₂ → Cl + HCHO + HO ₂	1.36 10 ⁻¹²	2	Atkinson et al. [168]
R114	ClO + NO → Cl + NO ₂	1.94 10 ⁻¹¹	2	Atkinson et al. [168]
R115	ClO + NO ₂ (+M) → ClONO ₂ (+M)	2.77 10 ⁻¹²	2	Atkinson et al. [168]
R116	Cl + ClONO ₂ → Cl ₂ + NO ₃	1.26 10 ⁻¹¹	2	Atkinson et al. [168]
R117	OCIO + NO → ClO + NO ₂	2.44 10 ⁻¹³	2	DeMore et al. [178]
R118	ClONO ₂ + OH → HOCl + NO ₃	3.34 10 ⁻¹³	2	Atkinson et al. [168]
R119	ClO + BrO → Br + OClO	8.47 10 ⁻¹²	2	Atkinson et al. [168]
R120	ClO + BrO → Br + Cl + O ₂	6.80 10 ⁻¹²	2	Atkinson et al. [168]
R121	ClO + BrO → BrCl + O ₂	1.12 10 ⁻¹²	2	Atkinson et al. [168]
R122	Br + OClO → BrO + ClO	1.69 10 ⁻¹³	2	Atkinson et al. [168]
R123	Br + Cl ₂ O ₂ → BrCl + ClOO	3.00 10 ⁻¹²	2	Atkinson et al. [168]
R124	Br ₂ + Cl → BrCl + Br	1.20 10 ⁻¹⁰	2	Sander et al. [98]
R125	BrCl + Br → Br ₂ + Cl	3.30 10 ⁻¹⁵	2	Sander et al. [98]
R126	Br + Cl ₂ → BrCl + Cl	1.10 10 ⁻¹⁵	2	Sander et al. [98]
R127	BrCl + Cl → Br + Cl ₂	1.50 10 ⁻¹¹	2	Sander et al. [98]
R128	HOBr + HCl $\xrightarrow{\text{aerosol}}$ BrCl + H ₂ O	See text		
R129	HOBr + H ⁺ + Cl ⁻ $\xrightarrow{\text{snow/ice}}$ BrCl + H ₂ O	See text		
R130	BrCl + hν → Br + Cl	5.70 10 ⁻³	1	Lehrer et al. [105]
R131	Cl ₂ + hν → 2Cl	8.50 10 ⁻⁴	1	Lehrer et al. [105]
R132	ClO + hν $\xrightarrow{O_2}$ Cl + O ₃	5.00 10 ⁻⁷	1	Lehrer et al. [105]
R133	HOCl + hν → Cl + OH	8.60 10 ⁻⁵	1	Lehrer et al. [105]
R134	ClONO ₂ + hν → Cl + NO ₃	1.30 10 ⁻²	1	Lehrer et al. [105]
R135	OCIO + hν $\xrightarrow{O_2}$ ClO + O ₃	3.60 10 ⁻²	1	Lehrer et al. [105]

C. Acknowledgements

First, I would like to thank my supervisor, Prof. Dr. Eva Gutheil for her advice, encouragement and patience. Without her support, I would never have been able to finish my doctoral research. She provided me the great opportunity to better understand the research field of the atmospheric chemistry and physics. Her guidance established the overall direction of the research and helped me to move on to explore the mysteries in depth. She encouraged me attending many wonderful conferences in which I have learned a lot. She has also helped me through all the processes of writing this thesis. All of these made the past years an extremely excellent experience in my life.

Special thanks are given to my co-supervisor, Prof. Dr. Ulrich Platt, whose profound knowledge of the atmospheric science triggers my interests for this research area. It is very kind of him for providing many instructive suggestions. I am also grateful to Dr. Holger Sihler for sharing the information of the experimental results, which enables me to improve my knowledge of the physical and chemical processes occurring in the ozone depletion event.

I still remember the time when I left my hometown Hefei and then arrived in Germany, I was so nervous and afraid about everything in Heidelberg. However, these bad feelings had disappeared at the time when I met Prof. Gutheil and other colleagues in my research group as they warmly welcomed me. Therefore, I would like to thank all the members or former members of my research group: Dr. Holger Grosshans, Yong Hu, Srikanth Reddy Gopireddy, Dr. Rana Muhammad Humza, Alaor Augusto Fava Sanches, Hernan Andres Olguin Astudillo, Dr. Xinguang Cui, Dr. Daniela Urzica, Dr. Haiwen Ge. They have given me many valuable suggestions and provoking discussions. I want to specially thank Dr. Holger Grosshans and Yong Hu who have spent much of their free time on the proofreading of this thesis. I also would like to thank the secretary Ellen Vogel and the computer system administrator Manfred Trunk who helped me a lot in their respective roles. All of these people made my work and life in Heidelberg much easier and more comfortable.

I greatly appreciate the financial support from the German Science Foundation (DFG) and Interdisciplinary Center for Scientific Computing (IWR).

My parents and parents-in-law receive my warmest love for their many years of support. I also wish to thank my wife Xuanli Sun for her selfless love during these years and taking care of our daughter Lynn, who is the source of the joy.

Bibliography

- [1] Seinfeld, J. and Pandis, S. *Atmospheric Chemistry and Physics: From Air Pollution to Climate Change*. Wiley-Interscience, 1998.
- [2] Schoenbein, C. *Recherches sur la nature de l'odeur qui se manifeste dans certaines actions chimiques*. 1840.
- [3] Cornu, A. “Sur la limite ultra-violette du spectre solaire”. In: *C. R. Acad. Sci.* Vol. 8 (1879), pp. 1101–1108.
- [4] Hartley, W. N. “On the probable absorption of solar radiation by atmospheric ozone”. In: *Chem. News* vol. 42 (1880), pp. 268–270.
- [5] Dobson, G., N., H. D., and J., L. “Measurements of the amount of ozone in the earth’s atmosphere and its relation to other geophysical condition”. In: *Proc. R. Soc. London, Ser. A* . Vol. 1222 (1929), pp. 456–486.
- [6] Götz, F. W. P., Dobson, G. M. B., and Meetham, A. R. “Vertical distribution of ozone in the atmosphere”. In: *Nature* vol. 132 (1933), pp. 281–281. DOI: 10.1038/132281a0.
- [7] Johnson, F. S., Purcell, J. D., Tousey, R., and Watanabe, K. “Direct measurements of the vertical distribution of atmospheric ozone to 70 kilometers altitude”. In: *Journal of Geophysical Research* vol. 57, no. 2 (1952), pp. 157–176. DOI: 10.1029/JZ057i002p00157.
- [8] Singer, S. F. *Scientific uses of earth satellites*. University of Michigan Press, 1956.
- [9] Logan, J. A. “Tropospheric ozone: Seasonal behavior, trends, and anthropogenic influence”. In: *Journal of Geophysical Research: Atmospheres* vol. 90, no. D6 (1985), pp. 10463–10482. DOI: 10.1029/JD090iD06p10463.
- [10] Low, P. S., Davies, T. D., Kelly, P. M., and Farmer, G. “Trends in surface ozone at Hohenpeissenberg and Arkona”. In: *Journal of Geophysical Research: Atmospheres* vol. 95, no. D13 (1990), pp. 22441–22453. DOI: 10.1029/JD095iD13p22441.
- [11] Matsumi, Y. and Kawasaki, M. “Photolysis of atmospheric ozone in the ultraviolet region”. In: *Chemical Reviews* vol. 103, no. 12 (2003), pp. 4767–4782. DOI: 10.1021/cr0205255.

-
- [12] Parrish, J. A., Jaenicke, K. F., and Anderson, R. R. "Erythema and Melanogenesis action spectra of normal human skin". In: *Photochemistry and Photobiology* vol. 36, no. 2 (1982), pp. 187–191. DOI: 10.1111/j.1751-1097.1982.tb04362.x.
- [13] Rowland, S. F. "Stratospheric Ozone Depletion". In: *Annual Review of Physical Chemistry* vol. 42, no. 1 (1991), pp. 731–768. DOI: 10.1146/annurev.pc.42.100191.003503.
- [14] UNEP, U. N. E. P. *Environmental effects of ozone depletion: 1998 assessment*. Tech. rep. Nairobi, Kenya, 1998.
- [15] McMichael, A. J., Lucas, R., Ponsonby, A.-L., and J., E. S. "Stratospheric ozone depletion, ultraviolet radiation and health". In: *Climate change and human health: risks and responses*. Ed. by A. J. McMichael, D. H. Campbell-Lendrum, C. F. Corvalan, K. L. Ebi, A. K. Githeko, and J. D. Scheraga. Geneva: World Health Organization (WHO Press), 2003, pp. 159–180.
- [16] *National Aeronautics and Space Administration (NASA) Home Page*. <http://www.nasa.gov/>.
- [17] Harrison, H. "Stratospheric ozone with added water vapor: influence of high-altitude aircraft". In: *Science* vol. 170, no. 3959 (1970), pp. 734–736. DOI: 10.1126/science.170.3959.734.
- [18] Voigt, Ch., Schumann, U., Graf, K., and Gottschaldt, K.-D. "Impact of rocket exhaust plumes on atmospheric composition and climate – an overview". In: *EUCASS Proceedings Series – Advances in AeroSpace Sciences*. Vol. 4. 2013, pp. 657–670. DOI: 10.1051/eucass/201304657.
- [19] Molina, M. J. and Rowland, F. S. "Stratospheric sink for chlorofluoromethanes: chlorine atom-catalysed destruction of ozone". In: *Nature* vol. 249, no. 5460 (1974), pp. 810–812. DOI: 10.1038/249810a0.
- [20] Rowland, F. S. and Molina, M. J. "Chlorofluoromethanes in the environment". In: *Reviews of Geophysics* vol. 13, no. 1 (1975), pp. 1–35. DOI: 10.1029/RG013i001p00001.
- [21] UNEP, U. N. E. P. *The 1987 Montreal protocol on substances that deplete the ozone layer*. Tech. rep. Montreal, Canada, 1987.
- [22] Farman, J. C., Gardiner, B. G., and Shanklin, J. D. "Large losses of total ozone in Antarctica reveal seasonal ClO_x/NO_x interaction". In: *Nature* vol. 315, no. 6016 (1985), pp. 207–210. DOI: 10.1038/315207a0.
- [23] *Total Ozone Mapping Spectrometer (TOMS) Website*. <http://ozoneaq.gsfc.nasa.gov/>.

- [24] *Ozone Monitoring Instrument (OMI) Website*. <http://www.knmi.nl/omi/>.
- [25] Solomon, S., Garcia, R. R., Rowland, F. S., and Wuebbles, D. J. “On the depletion of Antarctic ozone”. In: *Nature* vol. 321, no. 6072 (1986), pp. 755–758. DOI: 10.1038/321755a0.
- [26] Lippmann, M. “Health effects of tropospheric ozone”. In: *Environmental Science Technology* vol. 25, no. 12 (1991), pp. 1954–1962. DOI: 10.1021/es00024a001.
- [27] *Tropospheric Ozone, the Polluter*. http://www.ucar.edu/learn/1_7_1.htm/.
- [28] Allen, J. *The Ozone We Breathe*. http://earthobservatory.nasa.gov/Features/OzoneWeBreathe/ozone_we_breathe.php. 2002.
- [29] Krupa, S., McGrath, M. T., Andersen, C. P., Booker, F. L., Burkey, K. O., Chappelka, A. H., Chevone, B. I., Pell, E. J., and Zilinskas, B. A. “Ambient ozone and plant health”. In: *Plant Disease* vol. 85, no. 1 (2001), pp. 4–12. DOI: 10.1094/PDIS.2001.85.1.4.
- [30] Vingarzan, R. “A review of surface ozone background levels and trends”. In: *Atmospheric Environment* vol. 38, no. 21 (2004), pp. 3431–3442. DOI: <http://dx.doi.org/10.1016/j.atmosenv.2004.03.030>.
- [31] Reid, N. *A review of background ozone in the troposphere*. Tech. rep. Toronto, Canada: Ontario ministry of environment, 2007.
- [32] Barrie, L. A., Bottenheim, J. W., Schnell, R. C., Crutzen, P. J., and Rasmussen, R. A. “Ozone destruction and photochemical reactions at polar sunrise in the lower Arctic atmosphere”. In: *Nature* vol. 334, no. 6178 (1988), pp. 138–141. DOI: 10.1038/334138a0.
- [33] Oltmans, S. J. “Surface ozone measurements in clean air”. In: *Journal of Geophysical Research: Oceans* vol. 86, no. C2 (1981), pp. 1174–1180. DOI: 10.1029/JC086iC02p01174.
- [34] Bottenheim, J., Gallant, A., and Brice, K. “Measurements of NO_y species and O₃ at 82° N latitude”. In: *Geophysical Research Letters* vol. 13, no. 2 (1986), pp. 113–116. DOI: 10.1029/GL013i002p00113.
- [35] Barrie, L. and Platt, U. “Arctic tropospheric chemistry: an overview”. In: *Tellus B* vol. 49, no. 5 (1997), pp. 450–454. DOI: 10.1034/j.1600-0889.49.issue5.2.x.
- [36] Oltmans, S. J., Johnson, B. J., and Harris, J. M. “Springtime boundary layer ozone depletion at Barrow, Alaska: Meteorological influence, year-to-year variation, and long-term change”. In: *Journal of Geophysical Research: Atmospheres* vol. 117, no. D14 (2012). DOI: 10.1029/2011JD016889.

- [37] Barrie, L., Hartog, G., Bottenheim, J., and Landsberger, S. “Anthropogenic aerosols and gases in the lower troposphere at Alert Canada in April 1986”. In: *Journal of Atmospheric Chemistry* vol. 9, no. 1-3 (1989), pp. 101–127. DOI: 10.1007/BF00052827.
- [38] Oltmans, S., Schnell, R., Sheridan, P., Peterson, R., Li, S.-M., Winchester, J., Tans, P., Sturges, W., Kahl, J., and Barrie, L. “Seasonal surface ozone and filterable bromine relationship in the high Arctic”. In: *Atmospheric Environment (1967)* vol. 23, no. 11 (1989), pp. 2431–2441. DOI: [http://dx.doi.org/10.1016/0004-6981\(89\)90254-0](http://dx.doi.org/10.1016/0004-6981(89)90254-0).
- [39] Helmig, D., Oltmans, S. J., Carlson, D., Lamarque, J.-F., Jones, A., Labuschagne, C., Anlauf, K., and Hayden, K. “A review of surface ozone in the polar regions”. In: *Atmospheric Environment* vol. 41, no. 24 (2007), pp. 5138–5161. DOI: <http://dx.doi.org/10.1016/j.atmosenv.2006.09.053>.
- [40] Helmig, D., Boylan, P., Johnson, B., Oltmans, S., Fairall, C., Staebler, R., Weinheimer, A., Orlando, J., Knapp, D. J., Montzka, D. D., Flocke, F., Frieß, U., Sihler, H., and Shepson, P. B. “Ozone dynamics and snow-atmosphere exchanges during ozone depletion events at Barrow, Alaska”. In: *Journal of Geophysical Research: Atmospheres* vol. 117, no. D20 (2012). DOI: 10.1029/2012JD017531.
- [41] Simpson, W. R., King, M. D., Beine, H. J., Honrath, R. E., and Peterson, M. C. “Atmospheric photolysis rate coefficients during the Polar Sunrise Experiment {ALERT2000}”. In: *Atmospheric Environment* vol. 36, no. 15–16 (2002), pp. 2471–2480. DOI: [http://dx.doi.org/10.1016/S1352-2310\(02\)00123-1](http://dx.doi.org/10.1016/S1352-2310(02)00123-1).
- [42] Hausmann, M. and Platt, U. “Spectroscopic measurement of bromine oxide and ozone in the high Arctic during Polar Sunrise Experiment 1992”. In: *Journal of Geophysical Research: Atmospheres* vol. 99, no. D12 (1994), pp. 25399–25413. DOI: 10.1029/94JD01314.
- [43] Barrie, L. A., Bottenheim, J. W., and Hart, W. R. “Polar Sunrise Experiment 1992 (PSE 1992): Preface”. In: *Journal of Geophysical Research: Atmospheres* vol. 99, no. D12 (1994), pp. 25313–25314. DOI: 10.1029/94JD01929.
- [44] Kreher, K., Johnston, P. V., Wood, S. W., Nardi, B., and Platt, U. “Ground-based measurements of tropospheric and stratospheric BrO at Arrival Heights, Antarctica”. In: *Geophysical Research Letters* vol. 24, no. 23 (1997), pp. 3021–3024. DOI: 10.1029/97GL02997.

- [45] Tuckermann, M., Ackermann, R., Gölz, C., Lorenzen-Schmidt, H., Senne, T., Stutz, J., Trost, B., Unold, W., and Platt, U. “DOAS-observation of halogen radical-catalysed arctic boundary layer ozone destruction during the ARCTOC-campaigns 1995 and 1996 in Ny-Ålesund, Spitsbergen”. In: *Tellus B* vol. 49, no. 5 (1997), pp. 533–555. DOI: 10.1034/j.1600-0889.49.issue5.9.x.
- [46] Hönninger, G. and Platt, U. “Observations of BrO and its vertical distribution during surface ozone depletion at Alert”. In: *Atmospheric Environment* vol. 36, no. 15–16 (2002), pp. 2481–2489. DOI: [http://dx.doi.org/10.1016/S1352-2310\(02\)00104-8](http://dx.doi.org/10.1016/S1352-2310(02)00104-8).
- [47] Frieß, U., Hollwedel, J., König-Langlo, G., Wagner, T., and Platt, U. “Dynamics and chemistry of tropospheric bromine explosion events in the Antarctic coastal region”. In: *Journal of Geophysical Research: Atmospheres* vol. 109, no. D6 (2004). DOI: 10.1029/2003JD004133.
- [48] Wagner, T., Ibrahim, O., Sinreich, R., Frieß, U., Glasow, R. von, and Platt, U. “Enhanced tropospheric BrO over Antarctic sea ice in mid winter observed by MAX-DOAS on board the research vessel Polarstern”. In: *Atmospheric Chemistry and Physics* vol. 7, no. 12 (2007), pp. 3129–3142. DOI: 10.5194/acp-7-3129-2007.
- [49] Liao, J., Sihler, H., Huey, L. G., Neuman, J. A., Tanner, D. J., Friess, U., Platt, U., Flocke, F. M., Orlando, J. J., Shepson, P. B., Beine, H. J., Weinheimer, A. J., Sjostedt, S. J., Nowak, J. B., Knapp, D. J., Staebler, R. M., Zheng, W., Sander, R., Hall, S. R., and Ullmann, K. “A comparison of Arctic BrO measurements by chemical ionization mass spectrometry and long path-differential optical absorption spectroscopy”. In: *Journal of Geophysical Research: Atmospheres* vol. 116, no. D14 (2011). DOI: 10.1029/2010JD014788.
- [50] Sihler, H., Platt, U., Beirle, S., Marbach, T., Köhl, S., Dörner, S., Verschaeve, J., Frieß, U., Pöhler, D., Vogel, L., Sander, R., and Wagner, T. “Tropospheric BrO column densities in the Arctic derived from satellite: retrieval and comparison to ground-based measurements”. In: *Atmospheric Measurement Techniques* vol. 5, no. 11 (2012), pp. 2779–2807. DOI: 10.5194/amt-5-2779-2012.
- [51] Liao, J., Huey, L. G., Tanner, D. J., Flocke, F. M., Orlando, J. J., Neuman, J. A., Nowak, J. B., Weinheimer, A. J., Hall, S. R., Smith, J. N., Fried, A., Staebler, R. M., Wang, Y., Koo, J.-H., Cantrell, C. A., Weibring, P., Walega, J., Knapp, D. J., Shepson, P. B., and Stephens, C. R. “Observations of inorganic bromine (HOBr, BrO, and Br₂) speciation at Barrow, Alaska, in spring 2009”. In: *Journal of Geophysical Research: Atmospheres* vol. 117, no. D14 (2012). DOI: 10.1029/2011JD016641.

- [52] Stephens, C. R., Shepson, P. B., Steffen, A., Bottenheim, J. W., Liao, J., Huey, L. G., Apel, E., Weinheimer, A., Hall, S. R., Cantrell, C., Sive, B. C., Knapp, D. J., Montzka, D. D., and Hornbrook, R. S. “The relative importance of chlorine and bromine radicals in the oxidation of atmospheric mercury at Barrow, Alaska”. In: *Journal of Geophysical Research: Atmospheres* vol. 117, no. D14 (2012). DOI: 10.1029/2011JD016649.
- [53] Platt, U. and Janssen, C. “Observation and role of the free radicals NO₃, ClO, BrO and IO in the troposphere”. In: *Faraday Discuss.* Vol. 100 (1995), pp. 175–198. DOI: 10.1039/FD9950000175.
- [54] Platt, U. and Lehrer, E. *Arctic tropospheric ozone chemistry, ARCTOC. results from field, laboratory and modelling studies*. Air pollution research report 64. Luxembourg: European Commission Directorate-General, Science, Research and Development, 1997.
- [55] Wennberg, P. “Atmospheric chemistry: Bromine explosion”. In: *Nature* vol. 397, no. 6717 (1999), pp. 299–301. DOI: 10.1038/16805.
- [56] Glasow, R. von. “Atmospheric chemistry in volcanic plumes”. In: *Proceedings of the National Academy of Sciences* vol. 107, no. 15 (2010), pp. 6594–6599. DOI: 10.1073/pnas.0913164107.
- [57] Byun, D. and Ching, J. *Science algorithms of the EPA Models-3 Community Multiscale Air Quality (CMAQ) modeling system*. Tech. rep. Washington, DC, US, 1999.
- [58] Fiore, A., Jacob, D. J., Bey, I., Yantosca, R. M., Field, B. D., Fusco, A. C., and Wilkinson, J. G. “Background ozone over the United States in summer: Origin, trend, and contribution to pollution episodes”. In: *Journal of Geophysical Research: Atmospheres* vol. 107, no. D15 (2002), ACH 11–1–ACH 11–25. DOI: 10.1029/2001JD000982.
- [59] Fiore, A., Jacob, D. J., Liu, H., Yantosca, R. M., Fairlie, T. D., and Li, Q. “Variability in surface ozone background over the United States: Implications for air quality policy”. In: *Journal of Geophysical Research: Atmospheres* vol. 108, no. D24 (2003). DOI: 10.1029/2003JD003855.
- [60] Auvray, M. and Bey, I. “Long-range transport to Europe: Seasonal variations and implications for the European ozone budget”. In: *Journal of Geophysical Research: Atmospheres* vol. 110, no. D11 (2005). DOI: 10.1029/2004JD005503.

- [61] Kaminski, J. W., Plummer, D. A., Neary, L., McConnell, J. C., Struzewska, J., and Loboeki, L. “First application of MC2-AQ to multiscale air quality modelling over Europe”. In: *Physics and Chemistry of the Earth* vol. 27, no. 35 (2002), pp. 1517–1524. DOI: [http://dx.doi.org/10.1016/S1474-7065\(02\)00159-6](http://dx.doi.org/10.1016/S1474-7065(02)00159-6).
- [62] Tulet, P., Crassier, V., Solmon, F., Guedalia, D., and Rosset, R. “Description of the Mesoscale Nonhydrostatic Chemistry model and application to a trans-boundary pollution episode between northern France and southern England”. In: *Journal of Geophysical Research: Atmospheres* vol. 108, no. D1 (2003). DOI: 10.1029/2000JD000301.
- [63] Marécal, V., Rivière, E. D., Held, G., Cautenet, S., and Freitas, S. “Modelling study of the impact of deep convection on the utls air composition – Part I: Analysis of ozone precursors”. In: *Atmospheric Chemistry and Physics* vol. 6, no. 6 (2006), pp. 1567–1584. DOI: 10.5194/acp-6-1567-2006.
- [64] Rivière, E. D., Marécal, V., Larsen, N., and Cautenet, S. “Modelling study of the impact of deep convection on the UTLS air composition – Part 2: Ozone budget in the TTL”. In: *Atmospheric Chemistry and Physics* vol. 6, no. 6 (2006), pp. 1585–1598. DOI: 10.5194/acp-6-1585-2006.
- [65] *Weather Research and Forecasting (WRF) Model Description*. <http://www.mmm.ucar.edu/>.
- [66] Grell, G. A., Peckham, S. E., Schmitz, R., McKeen, S. A., Frost, G., Skamarock, W. C., and Eder, B. “Fully coupled ‘online’ chemistry within the {WRF} model”. In: *Atmospheric Environment* vol. 39, no. 37 (2005), pp. 6957–6975. DOI: <http://dx.doi.org/10.1016/j.atmosenv.2005.04.027>.
- [67] Kaminski, J. W., Neary, L., Struzewska, J., McConnell, J. C., Lupu, A., Jarosz, J., Toyota, K., Gong, S. L., Côté, J., Liu, X., Chance, K., and Richter, A. “GEM-AQ, an on-line global multiscale chemical weather modelling system: model description and evaluation of gas phase chemistry processes”. In: *Atmospheric Chemistry and Physics* vol. 8, no. 12 (2008), pp. 3255–3281. DOI: 10.5194/acp-8-3255-2008.
- [68] Chapman, S. *A Theory of Upper-atmospheric Ozone*. Memoirs of the Royal Meteorological Society. Edward Stanford, 1930.
- [69] Johnston, H. and Whitten, G. “Instantaneous photochemical rates in the global stratosphere”. In: *pure and applied geophysics* vol. 106-108, no. 1 (1973), pp. 1468–1489. DOI: 10.1007/BF00881099.

- [70] Bates, D. R. and Nicolet, M. "The photochemistry of atmospheric water vapor". In: *Journal of Geophysical Research* vol. 55, no. 3 (1950), pp. 301–327. DOI: 10.1029/JZ055i003p00301.
- [71] Crutzen, P. J. "The influence of nitrogen oxides on the atmospheric ozone content". In: *Quarterly Journal of the Royal Meteorological Society* vol. 96, no. 408 (1970), pp. 320–325. DOI: 10.1002/qj.49709640815.
- [72] Johnston, H. "Reduction of stratospheric ozone by nitrogen oxide catalysts from supersonic transport exhaust". In: *Science* vol. 173, no. 3996 (1971), pp. 517–522. DOI: 10.1126/science.173.3996.517.
- [73] Stolarski, R. S. and Cicerone, R. J. "Stratospheric chlorine: a possible sink for ozone". In: *Canadian Journal of Chemistry* vol. 52, no. 8 (1974), pp. 1610–1615. DOI: 10.1139/v74-233.
- [74] Molina, L. T. and Molina, M. J. "Production of chlorine oxide (Cl_2O_2) from the self-reaction of the chlorine oxide (ClO) radical". In: *The Journal of Physical Chemistry* vol. 91, no. 2 (1987), pp. 433–436. DOI: 10.1021/j100286a035.
- [75] McElroy, M. B., Salawitch, R. J., Wofsy, S. C., and Logan, J. A. "Reductions of Antarctic ozone due to synergistic interactions of chlorine and bromine". In: *Nature* vol. 321, no. 6072 (1986), pp. 759–762. DOI: 10.1038/321759a0.
- [76] Tung, K.-K., Ko, M. K. W., Rodriguez, J. M., and Dak Sze, N. "Are Antarctic ozone variations a manifestation of dynamics or chemistry?" In: *Nature* vol. 322, no. 6082 (1986), pp. 811–814. DOI: 10.1038/322811a0.
- [77] Wang, Y., Logan, J. A., and Jacob, D. J. "Global simulation of tropospheric O_3 - NO_x -hydrocarbon chemistry: 2. Model evaluation and global ozone budget". In: *Journal of Geophysical Research: Atmospheres* vol. 103, no. D9 (1998), pp. 10727–10755. DOI: 10.1029/98JD00157.
- [78] Platt, U. and Hönninger, G. "The role of halogen species in the troposphere". In: *Chemosphere* vol. 52, no. 2 (2003), pp. 325–338. DOI: [http://dx.doi.org/10.1016/S0045-6535\(03\)00216-9](http://dx.doi.org/10.1016/S0045-6535(03)00216-9).
- [79] Simpson, W. R., Glasow, R. von, Riedel, K., Anderson, P., Ariya, P., Bottenheim, J., Burrows, J., Carpenter, L. J., Frieß, U., Goodsite, M. E., Heard, D., Hutterli, M., Jacobi, H.-W., Kaleschke, L., Neff, B., Plane, J., Platt, U., Richter, A., Roscoe, H., Sander, R., Shepson, P., Sodeau, J., Steffen, A., Wagner, T., and Wolff, E. "Halogens and their role in polar boundary-layer ozone depletion". In: *Atmospheric Chemistry and Physics* vol. 7, no. 16 (2007), pp. 4375–4418. DOI: 10.5194/acp-7-4375-2007.

- [80] Abbatt, J. P. D., Thomas, J. L., Abrahamsson, K., Boxe, C., Granfors, A., Jones, A. E., King, M. D., Saiz-Lopez, A., Shepson, P. B., Sodeau, J., Toohey, D. W., Toubin, C., Glasow, R. von, Wren, S. N., and Yang, X. “Halogen activation via interactions with environmental ice and snow in the polar lower troposphere and other regions”. In: *Atmospheric Chemistry and Physics* vol. 12, no. 14 (2012), pp. 6237–6271. DOI: 10.5194/acp-12-6237-2012.
- [81] *FluxViewer Description*. <http://garfield.chem.elte.hu/>.
- [82] Wayne, R., Poulet, G., Biggs, P., Burrows, J., Cox, R., Crutzen, P., Hayman, G., Jenkin, M., Bras, G. L., Moortgat, G., Platt, U., and Schindler, R. “Halogen oxides: Radicals, sources and reservoirs in the laboratory and in the atmosphere”. In: *Atmospheric Environment* vol. 29, no. 20 (1995). Halogen oxides: Radicals, sources and reservoirs in the laboratory and in the atmosphere, pp. 2677–2881. DOI: [http://dx.doi.org/10.1016/1352-2310\(95\)98124-Q](http://dx.doi.org/10.1016/1352-2310(95)98124-Q).
- [83] Le Bras, G. and Platt, U. “A possible mechanism for combined chlorine and bromine catalyzed destruction of tropospheric ozone in the Arctic”. In: *Geophysical Research Letters* vol. 22, no. 5 (1995), pp. 599–602. DOI: 10.1029/94GL03334.
- [84] Fan, S.-M. and Jacob, D. J. “Surface ozone depletion in Arctic spring sustained by bromine reactions on aerosols”. In: *Nature* vol. 359, no. 6395 (1992), pp. 522–524. DOI: 10.1038/359522a0.
- [85] Tang, T. and McConnell, J. C. “Autocatalytic release of bromine from Arctic snow pack during polar sunrise”. In: *Geophysical Research Letters* vol. 23, no. 19 (1996), pp. 2633–2636. DOI: 10.1029/96GL02572.
- [86] Vogt, R., Crutzen, P. J., and Sander, R. “A mechanism for halogen release from sea-salt aerosol in the remote marine boundary layer”. In: *Nature* vol. 383, no. 6598 (1996), pp. 327–330. DOI: 10.1038/383327a0.
- [87] Sander, R. and Crutzen, P. J. “Model study indicating halogen activation and ozone destruction in polluted air masses transported to the sea”. In: *Journal of Geophysical Research: Atmospheres* vol. 101, no. D4 (1996), pp. 9121–9138. DOI: 10.1029/95JD03793.
- [88] Impey, G., Mihele, C., Anlauf, K., Barrie, L., Hastie, D., and Shepson, P. “Measurements of photolyzable halogen compounds and bromine radicals during the polar sunrise experiment 1997”. In: *Journal of Atmospheric Chemistry* vol. 34, no. 1 (1999), pp. 21–37. DOI: 10.1023/A:1006264912394.

- [89] Perovich, D. K. and Richter-Menge, J. A. "Surface characteristics of lead ice". In: *Journal of Geophysical Research: Oceans* vol. 99, no. C8 (1994), pp. 16341–16350. DOI: 10.1029/94JC01194.
- [90] Rankin, A. M., Wolff, E. W., and Martin, S. "Frost flowers: Implications for tropospheric chemistry and ice core interpretation". In: *Journal of Geophysical Research: Atmospheres* vol. 107, no. D23 (2002), AAC 4–1–AAC 4–15. DOI: 10.1029/2002JD002492.
- [91] Staebler, R., Toom-Sauntry, D., Barrie, L., Langendörfer, U., Lehrer, E., Li, S.-M., and Dryfhout-Clark, H. "Physical and chemical characteristics of aerosols at Spitsbergen in the spring of 1996". In: *Journal of Geophysical Research: Atmospheres* vol. 104, no. D5 (1999), pp. 5515–5529. DOI: 10.1029/1998JD100056.
- [92] Koop, T., Kapilashrami, A., Molina, L. T., and Molina, M. J. "Phase transitions of sea-salt/water mixtures at low temperatures: Implications for ozone chemistry in the polar marine boundary layer". In: *Journal of Geophysical Research: Atmospheres* vol. 105, no. D21 (2000), pp. 26393–26402. DOI: 10.1029/2000JD900413.
- [93] Michalowski, B. A., Francisco, J. S., Li, S.-M., Barrie, L. A., Bottenheim, J. W., and Shepson, P. B. "A computer model study of multiphase chemistry in the Arctic boundary layer during polar sunrise". In: *Journal of Geophysical Research: Atmospheres* vol. 105, no. D12 (2000), pp. 15131–15145. DOI: 10.1029/2000JD900004.
- [94] Foster, K. L., Plastridge, R. A., Bottenheim, J. W., Shepson, P. B., Finlayson-Pitts, B. J., and Spicer, C. W. "The role of Br₂ and BrCl in surface ozone destruction at polar sunrise". In: *Science* vol. 291, no. 5503 (2001), pp. 471–474.
- [95] Sander, R., Rudich, Y., Glasow, R. von, and Crutzen, P. J. "The role of BrNO₃ in marine tropospheric chemistry: A model study". In: *Geophysical Research Letters* vol. 26, no. 18 (1999), pp. 2857–2860. DOI: 10.1029/1999GL900478.
- [96] Finlayson-Pitts, B. J. "Reactions at surfaces in the atmosphere: integration of experiments and theory as necessary (but not necessarily sufficient) for predicting the physical chemistry of aerosols". In: *Phys. Chem. Chem. Phys.* Vol. 11 (2009), pp. 7760–7779. DOI: 10.1039/B906540G.
- [97] Stull, R. B. *An Introduction to Boundary Layer Meteorology*. The Netherlands: Kluwer Academic Publishers, 1988.

- [98] Sander, R., Vogt, R., Harris, G. W., and Crutzen, P. J. “Modelling the chemistry of ozone, halogen compounds, and hydrocarbons in the arctic troposphere during spring”. In: *Tellus B* vol. 49, no. 5 (1997), pp. 522–532. DOI: 10.1034/j.1600-0889.49.issue5.8.x.
- [99] Sander, R., Burrows, J., and Kaleschke, L. “Carbonate precipitation in brine – a potential trigger for tropospheric ozone depletion events”. In: *Atmospheric Chemistry and Physics* vol. 6, no. 12 (2006), pp. 4653–4658. DOI: 10.5194/acp-6-4653-2006.
- [100] Morin, S., Marion, G. M., Glasow, R. von, Voisin, D., Bouchez, J., and Savarino, J. “Precipitation of salts in freezing seawater and ozone depletion events: a status report”. In: *Atmospheric Chemistry and Physics* vol. 8, no. 23 (2008), pp. 7317–7324. DOI: 10.5194/acp-8-7317-2008.
- [101] Sander, R. and Morin, S. “Introducing the bromide/alkalinity ratio for a follow-up discussion on ”Precipitation of salts in freezing seawater and ozone depletion events: a status report”, by Morin et al., published in *Atmos. Chem. Phys.*, 8, 7317–7324, 2008”. In: *Atmospheric Chemistry and Physics* vol. 10, no. 16 (2010), pp. 7655–7658. DOI: 10.5194/acp-10-7655-2010.
- [102] Liao, J., Huey, L. G., Tanner, D. J., Brough, N., Brooks, S., Dibb, J. E., Stutz, J., Thomas, J. L., Lefer, B., Haman, C., and Gorham, K. “Observations of hydroxyl and peroxy radicals and the impact of BrO at Summit, Greenland in 2007 and 2008”. In: *Atmospheric Chemistry and Physics* vol. 11, no. 16 (2011), pp. 8577–8591. DOI: 10.5194/acp-11-8577-2011.
- [103] Bloss, W. J., Camredon, M., Lee, J. D., Heard, D. E., Plane, J. M. C., Saiz-Lopez, A., Bauguitte, S. J.-B., Salmon, R. A., and Jones, A. E. “Coupling of HO_x, NO_x and halogen chemistry in the antarctic boundary layer”. In: *Atmospheric Chemistry and Physics* vol. 10, no. 21 (2010), pp. 10187–10209. DOI: 10.5194/acp-10-10187-2010.
- [104] Bloss, W. J., Lee, J. D., Heard, D. E., Salmon, R. A., Bauguitte, S. J.-B., Roscoe, H. K., and Jones, A. E. “Observations of OH and HO₂ radicals in coastal Antarctica”. In: *Atmospheric Chemistry and Physics* vol. 7, no. 16 (2007), pp. 4171–4185. DOI: 10.5194/acp-7-4171-2007.
- [105] Lehrer, E., Hönninger, G., and Platt, U. “A one dimensional model study of the mechanism of halogen liberation and vertical transport in the polar troposphere”. In: *Atmospheric Chemistry and Physics* vol. 4, no. 11/12 (2004), pp. 2427–2440. DOI: 10.5194/acp-4-2427-2004.

-
- [106] Thomas, J. L., Stutz, J., Lefer, B., Huey, L. G., Toyota, K., Dibb, J. E., and Glasow, R. von. “Modeling chemistry in and above snow at Summit, Greenland – Part 1: Model description and results”. In: *Atmospheric Chemistry and Physics* vol. 11, no. 10 (2011), pp. 4899–4914. DOI: 10.5194/acp-11-4899-2011.
- [107] Thomas, J. L., Dibb, J. E., Huey, L. G., Liao, J., Tanner, D., Lefer, B., Glasow, R. von, and Stutz, J. “Modeling chemistry in and above snow at Summit, Greenland – Part 2: Impact of snowpack chemistry on the oxidation capacity of the boundary layer”. In: *Atmospheric Chemistry and Physics* vol. 12, no. 14 (2012), pp. 6537–6554. DOI: 10.5194/acp-12-6537-2012.
- [108] Glasow, R. von, Sander, R., Bott, A., and Crutzen, P. J. “Modeling halogen chemistry in the marine boundary layer 1. Cloud-free MBL”. In: *Journal of Geophysical Research: Atmospheres* vol. 107, no. D17 (2002). DOI: 10.1029/2001JD000942.
- [109] Glasow, R. von, Sander, R., Bott, A., and Crutzen, P. J. “Modeling halogen chemistry in the marine boundary layer 2. Interactions with sulfur and the cloud-covered MBL”. In: *Journal of Geophysical Research: Atmospheres* vol. 107, no. D17 (2002). DOI: 10.1029/2001JD000943.
- [110] Glasow, R. von and Crutzen, P. J. “Model study of multiphase DMS oxidation with a focus on halogens”. In: *Atmospheric Chemistry and Physics* vol. 4, no. 3 (2004), pp. 589–608. DOI: 10.5194/acp-4-589-2004.
- [111] Zeng, T., Wang, Y., Chance, K., Browell, E. V., Ridley, B. A., and Atlas, E. L. “Widespread persistent near-surface ozone depletion at northern high latitudes in spring”. In: *Geophysical Research Letters* vol. 30, no. 24 (2003). DOI: 10.1029/2003GL018587.
- [112] Zeng, T., Wang, Y., Chance, K., Blake, N., Blake, D., and Ridley, B. “Halogen-driven low-altitude O₃ and hydrocarbon losses in spring at northern high latitudes”. In: *Journal of Geophysical Research: Atmospheres* vol. 111, no. D17 (2006). DOI: 10.1029/2005JD006706.
- [113] Zhao, T. L., Gong, S. L., Bottenheim, J. W., McConnell, J. C., Sander, R., Kaleschke, L., Richter, A., Kerkweg, A., Toyota, K., and Barrie, L. A. “A three-dimensional model study on the production of BrO and Arctic boundary layer ozone depletion”. In: *Journal of Geophysical Research: Atmospheres* vol. 113, no. D24 (2008). DOI: 10.1029/2008JD010631.
- [114] Yang, X., Pyle, J. A., and Cox, R. A. “Sea salt aerosol production and bromine release: Role of snow on sea ice”. In: *Geophysical Research Letters* vol. 35, no. 16 (2008). DOI: 10.1029/2008GL034536.

- [115] Yang, X., Pyle, J. A., Cox, R. A., Theys, N., and Van Roozendael, M. “Snow-sourced bromine and its implications for polar tropospheric ozone”. In: *Atmospheric Chemistry and Physics* vol. 10, no. 16 (2010), pp. 7763–7773. DOI: 10.5194/acp-10-7763-2010.
- [116] Jones, A. E., Anderson, P. S., Begoin, M., Brough, N., Hutterli, M. A., Marshall, G. J., Richter, A., Roscoe, H. K., and Wolff, E. W. “BrO, blizzards, and drivers of polar tropospheric ozone depletion events”. In: *Atmospheric Chemistry and Physics* vol. 9, no. 14 (2009), pp. 4639–4652. DOI: 10.5194/acp-9-4639-2009.
- [117] Jones, A. E., Anderson, P. S., Wolff, E. W., Roscoe, H. K., Marshall, G. J., Richter, A., Brough, N., and Colwell, S. R. “Vertical structure of Antarctic tropospheric ozone depletion events: characteristics and broader implications”. In: *Atmospheric Chemistry and Physics* vol. 10, no. 16 (2010), pp. 7775–7794. DOI: 10.5194/acp-10-7775-2010.
- [118] Toyota, K., McConnell, J. C., Lupu, A., Neary, L., McLinden, C. A., Richter, A., Kwok, R., Semeniuk, K., Kaminski, J. W., Gong, S.-L., Jarosz, J., Chipperfield, M. P., and Sioris, C. E. “Analysis of reactive bromine production and ozone depletion in the Arctic boundary layer using 3-D simulations with GEM-AQ: inference from synoptic-scale patterns”. In: *Atmospheric Chemistry and Physics* vol. 11, no. 8 (2011), pp. 3949–3979. DOI: 10.5194/acp-11-3949-2011.
- [119] Toyota, K., Dastoor, A. P., and Ryzhkov, A. “Air-snowpack exchange of bromine, ozone and mercury in the springtime Arctic simulated by the 1-D model PHANTAS – Part 2: Mercury and its speciation”. In: *Atmospheric Chemistry and Physics Discussions* vol. 13, no. 8 (2013), pp. 22151–22220. DOI: 10.5194/acpd-13-22151-2013.
- [120] Turanyi, T. “KINAL - a program package for kinetic analysis of reaction mechanisms.” In: *Computers and Chemistry* vol. 14, no. 3 (1990), pp. 253–254.
- [121] Schwartz, S. “Mass-transport considerations pertinent to aqueous phase reactions of gases in liquid-water clouds”. In: *Chemistry of Multiphase Atmospheric Systems*. Ed. by W. Jaeschke. Vol. 6. NATO ASI Series. Springer Berlin Heidelberg, 1986, pp. 415–471. DOI: 10.1007/978-3-642-70627-1_16.
- [122] Cao, L., Sihler, H., Platt, U., and Gutheil, E. “Numerical analysis of the chemical kinetic mechanisms of ozone depletion and halogen release in the polar troposphere”. In: *Atmospheric Chemistry and Physics Discussions* vol. 13, no. 9 (2013), pp. 24171–24222. DOI: 10.5194/acpd-13-24171-2013.

- [123] Hanson, D. R., Ravishankara, A. R., and Solomon, S. "Heterogeneous reactions in sulfuric acid aerosols: A framework for model calculations". In: *Journal of Geophysical Research: Atmospheres* vol. 99, no. D2 (1994), pp. 3615–3629. DOI: 10.1029/93JD02932.
- [124] Huff, A. K. and Abbatt, J. P. D. "Gas-phase Br₂ production in heterogeneous reactions of Cl₂, HOCl, and BrCl with halide-ice surfaces". In: *The Journal of Physical Chemistry A* vol. 104, no. 31 (2000), pp. 7284–7293. DOI: 10.1021/jp001155w.
- [125] Huff, A. K. and Abbatt, J. P. D. "Kinetics and product yields in the heterogeneous reactions of HOBr with ice surfaces containing NaBr and NaCl". In: *The Journal of Physical Chemistry A* vol. 106, no. 21 (2002), pp. 5279–5287. DOI: 10.1021/jp014296m.
- [126] Beare, R., Macvean, M., Holtslag, A., Cuxart, J., Esau, I., Golaz, J.-C., Jimenez, M., Khairoutdinov, M., Kosovic, B., Lewellen, D., Lund, T., Lundquist, J., McCabe, A., Moene, A., Noh, Y., Raasch, S., and Sullivan, P. "An intercomparison of large-eddy simulations of the stable boundary layer". In: *Boundary-Layer Meteorology* vol. 118, no. 2 (2006), pp. 247–272. DOI: 10.1007/s10546-004-2820-6.
- [127] Evans, M. J., Jacob, D. J., Atlas, E., Cantrell, C. A., Eisele, F., Flocke, F., Fried, A., Mauldin, R. L., Ridley, B. A., Wert, B., Talbot, R., Blake, D., Heikes, B., Snow, J., Walega, J., Weinheimer, A. J., and Dibb, J. "Coupled evolution of BrO_x-ClO_x-HO_x-NO_x chemistry during bromine-catalyzed ozone depletion events in the arctic boundary layer". In: *Journal of Geophysical Research: Atmospheres* vol. 108, no. D4 (2003). DOI: 10.1029/2002JD002732.
- [128] Adams, J. W., Holmes, N. S., and Crowley, J. N. "Uptake and reaction of HOBr on frozen and dry NaCl/NaBr surfaces between 253 and 233 K". In: *Atmospheric Chemistry and Physics* vol. 2, no. 1 (2002), pp. 79–91. DOI: 10.5194/acp-2-79-2002.
- [129] Yang, X., Cox, R. A., Warwick, N. J., Pyle, J. A., Carver, G. D., O'Connor, F. M., and Savage, N. H. "Tropospheric bromine chemistry and its impacts on ozone: A model study". In: *Journal of Geophysical Research: Atmospheres* vol. 110, no. D23 (2005). DOI: 10.1029/2005JD006244.
- [130] Röth, E. P. "A fast algorithm to calculate the photonflux in optically dense media for use in photochemical models". In: *Berichte der Bunsengesellschaft für physikalische Chemie* vol. 96, no. 3 (1992), pp. 417–420. DOI: 10.1002/bbpc.19920960335.

- [131] Röth, E. P. *Description of the anisotropic radiation transfer model ART to determine photodissociation coefficients*. Vol. 3960. Berichte des Forschungszentrums Jülich JUEL-3960. Jülich: Forschungszentrum, Zentralbibliothek, 2002.
- [132] Valko, P. and Vajda, S. “An extended ode solver for sensitivity calculations”. In: *Computers and Chemistry* vol. 8, no. 4 (1984), pp. 255–271. DOI: [http://dx.doi.org/10.1016/0097-8485\(84\)85017-2](http://dx.doi.org/10.1016/0097-8485(84)85017-2).
- [133] *OpenFOAM Website*. <http://www.openfoam.com/>.
- [134] Poinso, T. and Veynante, D. *Theoretical and Numerical Combustion*. Edwards, 2005.
- [135] Sullivan, P., McWilliams, J., and Moeng, C.-H. “A subgrid-scale model for large-eddy simulation of planetary boundary-layer flows”. In: *Boundary-Layer Meteorology* vol. 71, no. 3 (1994), pp. 247–276. DOI: 10.1007/BF00713741.
- [136] Fureby, C. “On subgrid scale modeling in large eddy simulations of compressible fluid flow”. In: *Physics of Fluids* vol. 8, no. 5 (1996), pp. 1301–1311. DOI: <http://dx.doi.org/10.1063/1.868900>.
- [137] Yoshizawa, A. “Bridging between eddy-viscosity-type and second-order turbulence models through a two-scale turbulence theory”. In: *Phys Rev E Stat Phys Plasmas Fluids Relat Interdiscip Topics* vol. 48, no. 1 (1993), pp. 273–281.
- [138] Smagorinsky, J. “General circulation experiments with the primitive equations”. In: *Monthly Weather Review* vol. 91, no. 3 (1963), pp. 99–164. DOI: 10.1175/1520-0493(1963)091<0099:GCEWTP>2.3.CO;2.
- [139] Pope, S. *Turbulent Flows*. Cambridge University Press, 2000.
- [140] Chase, M. W. “NIST–JANAF thermochemical tables for the bromine oxides”. In: *Journal of Physical and Chemical Reference Data* vol. 25, no. 4 (1996), pp. 1069–1111. DOI: <http://dx.doi.org/10.1063/1.555993>.
- [141] McBride, B. J., Gordon, S., and Reno, M. A. *Coefficients for calculating thermodynamic and transport properties of individual species*. National Aeronautics and Space Administration, 1993, p. 94.
- [142] Lundström, A. *ReactingFoam tutorial (simple gas phase reaction)*. Tech. rep. Chalmers University of Technology, 2008, p. 8.
- [143] McBride, B. and Gordon, S. *Computer program for calculating and fitting thermodynamic functions*. NASA reference publication Nr. 1271. National Aeronautics, Space Administration, Office of Management, Scientific, and Technical Information Program, 1992.

- [144] McGrath, M. P. and Rowland, F. S. “Ideal gas thermodynamic properties of HOBr”. In: *The Journal of Physical Chemistry* vol. 98, no. 18 (1994), pp. 4773–4775. DOI: 10.1021/j100069a001.
- [145] Harten, A. “High resolution schemes for hyperbolic conservation laws”. In: *Journal of Computational Physics* vol. 49, no. 3 (1983), pp. 357–393. DOI: [http://dx.doi.org/10.1016/0021-9991\(83\)90136-5](http://dx.doi.org/10.1016/0021-9991(83)90136-5).
- [146] Issa, R., Gosman, A., and Watkins, A. “The computation of compressible and incompressible recirculating flows by a non-iterative implicit scheme”. In: *Journal of Computational Physics* vol. 62, no. 1 (1986), pp. 66–82. DOI: [http://dx.doi.org/10.1016/0021-9991\(86\)90100-2](http://dx.doi.org/10.1016/0021-9991(86)90100-2).
- [147] *bwGRiD Website*. <http://www.bw-grid.de/das-bwgrid/>.
- [148] Pascau, A., Pérez, C., and Serón, F. J. “A comparison of segregated and coupled methods for the solution of the incompressible Navier-Stokes equations”. In: *Communications in Numerical Methods in Engineering* vol. 12, no. 10 (1996), pp. 617–630. DOI: 10.1002/(SICI)1099-0887(199610)12:10<617::AID-CNM10>3.0.CO;2-J.
- [149] Ferziger, J. and Perić, M. *Computational methods for fluid dynamics*. Springer London, 2002.
- [150] Harlow, F. H. and Welch, J. E. “Numerical calculation of time – dependent viscous incompressible flow of fluid with free surface”. In: *Physics of Fluids* vol. 8, no. 12 (1965), pp. 2182–2189. DOI: <http://dx.doi.org/10.1063/1.1761178>.
- [151] Von Neumann, J. and Richtmyer, R. D. “A method for the numerical calculation of hydrodynamic shocks”. In: *Journal of Applied Physics* vol. 21, no. 3 (1950), pp. 232–237. DOI: <http://dx.doi.org/10.1063/1.1699639>.
- [152] Patankar, S. V. and Spalding, D. B. “A calculation procedure for heat, mass and momentum transfer in three-dimensional parabolic flows”. In: *Int. J. Heat Mass Transfer* vol. 15 (1972), pp. 1787–1972.
- [153] Patankar, S. V. *Numerical heat transfer and fluid flow*. Taylor & Francis, 1980.
- [154] Versteeg, H. and Malalasekera, W. *An introduction to computational fluid dynamics: the finite volume method*. Pearson Education Limited, 2007.
- [155] Cao, L. and Gutheil, E. “Numerical simulation of tropospheric ozone depletion in the polar spring”. In: *Air Quality, Atmosphere and Health* (2013), pp. 1–14. DOI: 10.1007/s11869-013-0208-9.

- [156] Jones, A. E., Weller, R., Wolff, E. W., and Jacobi, H. W. "Speciation and rate of photochemical NO and NO₂ production in Antarctic snow". In: *Geophysical Research Letters* vol. 27, no. 3 (2000), pp. 345–348. DOI: 10.1029/1999GL010885.
- [157] Jones, A. E., Weller, R., Anderson, P. S., Jacobi, H.-W., Wolff, E. W., Schrems, O., and Miller, H. "Measurements of NO_x emissions from the Antarctic snow-pack". In: *Geophysical Research Letters* vol. 28, no. 8 (2001), pp. 1499–1502. DOI: 10.1029/2000GL011956.
- [158] Jacobi, H.-W., Frey, M. M., Hutterli, M. A., Bales, R. C., Schrems, O., Cullen, N. J., Steffen, K., and Koehler, C. "Measurements of hydrogen peroxide and formaldehyde exchange between the atmosphere and surface snow at Summit, Greenland". In: *Atmospheric Environment* vol. 36, no. 15–16 (2002), pp. 2619–2628. DOI: [http://dx.doi.org/10.1016/S1352-2310\(02\)00106-1](http://dx.doi.org/10.1016/S1352-2310(02)00106-1).
- [159] Grannas, A. M., Jones, A. E., Dibb, J., Ammann, M., Anastasio, C., Beine, H. J., Bergin, M., Bottenheim, J., Boxe, C. S., Carver, G., Chen, G., Crawford, J. H., Dominé, F., Frey, M. M., Guzmán, M. I., Heard, D. E., Helmig, D., Hoffmann, M. R., Honrath, R. E., Huey, L. G., Hutterli, M., Jacobi, H. W., Klán, P., Lefer, B., McConnell, J., Plane, J., Sander, R., Savarino, J., Shepson, P. B., Simpson, W. R., Sodeau, J. R., Glasow, R. von, Weller, R., Wolff, E. W., and Zhu, T. "An overview of snow photochemistry: evidence, mechanisms and impacts". In: *Atmospheric Chemistry and Physics* vol. 7, no. 16 (2007), pp. 4329–4373. DOI: 10.5194/acp-7-4329-2007.
- [160] Langendörfer, U., Lehrer, E., Wagenbach, D., and Platt, U. "Observation of filterable bromine variabilities during arctic tropospheric ozone depletion events in high (1 hour) time resolution". In: *Journal of Atmospheric Chemistry* vol. 34, no. 1 (1999), pp. 39–54. DOI: 10.1023/A:1006217001008.
- [161] Jones, A. E., Anderson, P. S., Wolff, E. W., Turner, J., Rankin, A. M., and Colwell, S. R. "A role for newly forming sea ice in springtime polar tropospheric ozone loss? Observational evidence from Halley station, Antarctica". In: *Journal of Geophysical Research: Atmospheres* vol. 111, no. D8 (2006). DOI: 10.1029/2005JD006566.
- [162] Perner, D., Arnold, T., Crowley, J., Klüpfel, T., Martinez, M., and Seuwen, R. "The measurement of active chlorine in the atmosphere by chemical amplification". In: *Journal of Atmospheric Chemistry* vol. 34, no. 1 (1999), pp. 9–20. DOI: 10.1023/A:1006208828324.

- [163] Jobson, B. T., Niki, H., Yokouchi, Y., Bottenheim, J., Hopper, F., and Leaitch, R. "Measurements of C₂-C₆ hydrocarbons during the Polar Sunrise 1992 Experiment: Evidence for Cl atom and Br atom chemistry". In: *Journal of Geophysical Research: Atmospheres* vol. 99, no. D12 (1994), pp. 25355–25368. DOI: 10.1029/94JD01243.
- [164] Solberg, S., Schmidbauer, N., Semb, A., Stordal, F., and Hov, Ø. "Boundary-layer ozone depletion as seen in the Norwegian Arctic in spring". In: *Journal of Atmospheric Chemistry* vol. 23, no. 3 (1996), pp. 301–332. DOI: 10.1007/BF00055158.
- [165] Ramacher, B., Rudolph, J., and Koppmann, R. "Hydrocarbon measurements during tropospheric ozone depletion events: Evidence for halogen atom chemistry". In: *Journal of Geophysical Research: Atmospheres* vol. 104, no. D3 (1999), pp. 3633–3653. DOI: 10.1029/1998JD100061.
- [166] Boudries, H. and Bottenheim, J. "Cl and Br atom concentrations during a surface boundary layer ozone depletion event in the Canadian High Arctic". In: *Geophysical Research Letters* vol. 27, no. 4 (2000), pp. 517–520. DOI: 10.1029/1999GL011025.
- [167] Spicer, C. W., Plastringe, R. A., Foster, K. L., Finlayson-Pitts, B. J., Bottenheim, J. W., Grannas, A. M., and Shepson, P. B. "Molecular halogens before and during ozone depletion events in the Arctic at polar sunrise: concentrations and sources". In: *Atmospheric Environment* vol. 36, no. 15–16 (2002), pp. 2721–2731. DOI: [http://dx.doi.org/10.1016/S1352-2310\(02\)00125-5](http://dx.doi.org/10.1016/S1352-2310(02)00125-5).
- [168] Atkinson, R., Baulch, D. L., Cox, R. A., Crowley, J. N., Hampson, R. F., Hynes, R. G., Jenkin, M. E., Kerr, J. A., Rossi, M., and Troe, J. *Summary of Evaluated Kinetic and Photochemical Data for Atmospheric Chemistry*. Tech. rep. 2006, p. 60.
- [169] Borken, J. "Ozonabbau durch Halogene in der arktischen Grenzschicht. Reaktionskinetische Modellrechnungen zu einem Fröhjahrsphänomen". PhD thesis. Heidelberg University, 1996, p. 151.
- [170] Barnes, I., Becker, K., and Overath, R. "Oxidation of organic sulfur compounds". In: *The Tropospheric Chemistry of Ozone in the Polar Regions*. Ed. by H. Niki and K. Becker. Vol. 7. Springer Berlin Heidelberg, 1993, pp. 371–383. DOI: 10.1007/978-3-642-78211-4_27.
- [171] Aranda, A., Le Bras, G., La Verdet, G., and Poulet, G. "The BrO + CH₃O₂ reaction: Kinetics and role in the atmospheric ozone budget". In: *Geophysical Research Letters* vol. 24, no. 22 (1997), pp. 2745–2748. DOI: 10.1029/97GL02686.

- [172] Kosović, B. and Curry, J. A. “A large eddy simulation study of a quasi-steady, stably stratified atmospheric boundary layer”. In: *Journal of the Atmospheric Sciences* vol. 57, no. 8 (2000), pp. 1052–1068. DOI: 10.1175/1520-0469(2000)057<1052:ALESS0>2.0.CO;2.
- [173] Monin, A. S. and Obukhov, A. M. “Basic laws of turbulent mixing in the ground layer of the atmosphere”. In: *Tr. Akad. Nauk SSSR Geofiz. Inst* vol. 24 (1954), pp. 163–187.
- [174] Poulos, G. S., Blumen, W., Fritts, D. C., Lundquist, J. K., Sun, J., Burns, S. P., Nappo, C., Banta, R., Newsom, R., Cuxart, J., Terradellas, E., Balsley, B., and Jensen, M. “CASES-99: a comprehensive investigation of the stable nocturnal boundary layer”. In: *Bulletin of the American Meteorological Society* vol. 83, no. 4 (2002), pp. 555–581. DOI: 10.1175/1520-0477(2002)083<0555:CACIOT>2.3.CO;2.
- [175] Cao, L. and Gutheil, E. “Modeling and simulation of tropospheric ozone depletion in the polar spring”. In: *Proceedings of ASME 2014 4th Joint US-European Fluids Engineering Summer Meeting*. Chicago, IL, USA, 2014.
- [176] *ANSYS ICEM CFD Website*. <http://www.ansys.com/Products/Other+Products/ANSYS+ICEM+CFD/>.
- [177] Liu, Q. and Margerum, D. W. “Equilibrium and kinetics of bromine chloride hydrolysis”. In: *Environmental Science and Technology* vol. 35, no. 6 (2001), pp. 1127–1133. DOI: 10.1021/es001380r.
- [178] DeMore, W., Sander, S., Golden, D., Hampson, R., Kurylo, M., Howard, C., Ravishankara, A., Kolb, C., and Molina, M. *Chemical kinetics and photochemical data for use in stratospheric modeling No. 12*. 1997.

**Eidesstattliche Versicherung gemäß § 8 der Promotionsordnung
der Naturwissenschaftlich-Mathematischen Gesamtfakultät
der Universität Heidelberg**

1. Bei der eingereichten Dissertation zu dem Thema

handelt es sich um meine eigenständig erbrachte Leistung.

2. Ich habe nur die angegebenen Quellen und Hilfsmittel benutzt und mich keiner unzulässigen Hilfe Dritter bedient. Insbesondere habe ich wörtlich oder sinngemäß aus anderen Werken übernommene Inhalte als solche kenntlich gemacht.

3. Die Arbeit oder Teile davon habe ich wie folgt/bislang nicht¹⁾ an einer Hochschule des In- oder Auslands als Bestandteil einer Prüfungs- oder Qualifikationsleistung vorgelegt.

Titel der Arbeit: _____

Hochschule und Jahr: _____

Art der Prüfungs- oder Qualifikationsleistung: _____

4. Die Richtigkeit der vorstehenden Erklärungen bestätige ich.

5. Die Bedeutung der eidesstattlichen Versicherung und die strafrechtlichen Folgen einer unrichtigen oder unvollständigen eidesstattlichen Versicherung sind mir bekannt.

Ich versichere an Eides statt, dass ich nach bestem Wissen die reine Wahrheit erklärt und nichts verschwiegen habe.

Ort und Datum

Unterschrift

¹⁾ Nicht Zutreffendes streichen. Bei Bejahung sind anzugeben: der Titel der andernorts vorgelegten Arbeit, die Hochschule, das Jahr der Vorlage und die Art der Prüfungs- oder Qualifikationsleistung.